Technische Universität München
TUM School of Life Sciences

How substrate helix dynamics affect intramembrane proteolysis by γ-secretase.

Philipp Alexander Högel

Vollständiger Abdruck der von der TUM School of Life Sciences der Technischen Universität München zur Erlangung eines Doktors der Naturwissenschaften (Dr. rer. nat) genehmigten Dissertation.

Vorsitz: Prof. Dr.Bernhard Küster

Prüfende der Dissertation:

1. Prof. Dr. Dieter Langosch
2. Prof. Dr. Stefan Lichtenthaler

Die Dissertation wurde am 30.11.2023 bei der Technischen Universität München eingereicht und durch die TUM School of Life Sciences am 29.01.2024 angenommen.

Zusammenfassung

Intramembranproteolyse findet innerhalb einer Doppellipidschicht statt und ist als grundlegender Prozess einer Zelle in nahezu allen Reichen des Lebens vertreten. Zu ihren biologischen Folgen gehören die Sekretion von Wachstumsfaktoren, entscheidende Signalweiterleitungen oder der Membranproteinumsatz. Aufgrund ihrer essenziellen Funktionen kann ein Fehler in der Proteolyse der Transmembrandomäne (TMD) von Substraten zu schweren Krankheiten wie diversen Krebserkrankungen, Alzheimer oder Parkinson führen. Aufgrund ihrer Verbindung zur Alzheimer-Krankheit stellen die Aspartylprotease γ-Sekretase und ihr Substrat, das C99-Fragment von APP, sicherlich das prominenteste Enzym/Substrat-Paar dieser Gattung dar.

Trotz ihrer biologischen Relevanz ist nur wenig über den Mechanismus der Intramembranproteolyse bekannt. Derzeit ist unklar, was ein Substrat von einem Nicht-Substrat unterscheidet oder wie eine spezifische Schnittstelle ausgewählt wird. Da für Transmembranproteasen keine Konsensussequenzen bekannt sind, müssen die Kriterien dafür in der Struktur der Substrate verborgen sein.

Um dieses Thema aufzuklären, habe ich die Helixdynamik eines auf der TMD von C99 basierenden Peptids in Detergenzien, Lösung und in der Gasphase untersucht. Zu diesem Zweck wurde eine neuartige Methode entwickelt, um die bekannte Technik des Deuterium-Wasserstoff-Austauschs in Kombination mit der Elektronentransferdissoziation zu verbessern und somit die Stärke (ΔG) der H-Brücken des TMD-Rückgrats auf der Ebene einzelner Aminosäuren quantifizieren zu können.

In einer ersten Reihe von Experimenten wurde der Zusammenhang zwischen Primärstruktur und Helixflexibilität anhand verschiedener Punktmutanten bestimmt. In einer zweiten Reihe wurde ein Satz künstlicher Peptide untersucht, die auf Poly-Leu und Poly-Ala basieren und Sequenzmotive der C99 TMD enthalten.

Beide Experimentreihen belegten eine lokale Erhöhung der Helixflexibililtät durch ein doppel-Glycin Motiv, welches auch als Scharnier dienen könnte, sowie die große Bedeutung der Seitenketten von Threonin für die Stabilität einer TMD-Helix. Darüber hinaus wurde eine Wechselwirkung zwischen der zentralen Region der TMD und der C-terminalen Spaltregion nachgewiesen, bei der die Primärsequenz in der einen Region die Helixdynamik in der jeweils anderen beeinflusst. Abschließend wurden die Ergebnisse genutzt, um den Zusammenhang zwischen der Helixflexibilität in verschiedenen Regionen der TMD und dem Resultat der Proteolyse systematisch zu analysieren. Letzteres beruhte auf den Ergebnissen aus Spaltversuchen, die von Kooperationspartnern *in vitro* und *in cellulo* durchgeführt wurden.

Abstract

Intramembrane proteolysis occurs in the plane of a lipid bilayer, and as a fundamental process in the cell, it is found in almost all kingdoms of life. Its biological consequences include secretion of growth factors, critical signaling events or membrane protein turnover. Due to its crucial functions, malfunction in the proteolysis of substrate transmembrane domains (TMDs) can cause severe diseases like various types of cancer, Alzheimer's-, or Parkinson's disease.

Due to its liaison with Alzheimer's disease, the aspartyl protease γ-secretase with its substrate, the C99 fragment of APP, surely represent the most prominent enzyme/substrate pair in this field.

Despite their biological relevance, little is known about the mechanism behind intramembrane proteolysis. Currently it is unclear what distinguishes a substrate from a non-substrate or how a specific cleavage site is selected. As transmembrane proteases share no consensus-sequence, the secrets of intramembrane proteolysis must be hidden in the structure of the substrates.

To address this question, I studied the helix dynamics of the C99 TMD-based peptide in detergent, solvent, and gas-phase. To this end, a novel method was developed to enhance the existing technique of deuterium-hydrogen exchange in combination with electron-transfer dissociation to quantify the strength (ΔG) of TMD backbone H-bonds at a residue specific level.

In a first series of experiments, the connection between primary structure und helix flexibility was determined using various point mutants. In a second series, a novel set of artificial peptides was introduced, based on poly-Leu and poly-Ala, holding sequence motifs of the C99 TMD.

Both series highlighted a local increase in helix flexibility through a double glycine motif, which might serve as a hinge, as well as the high relevance of threonine side chains for the stability of a TMD helix. They also revealed an interaction between the central region of the TMD and the C-terminal cleavage region, in which the primary sequence in one region affects the helix dynamics in the other.

Finally, my results were used to systematically analyze the impact of helix flexibility in different regions of the TMD on the outcome of the proteolytic process, as studied by results from cleavage assays, obtained by collaborating partners *in vitro* and *in cellulo*.

Acknowledgements

Throughout my work on the present doctoral dissertation, I have received support from many persons whom I want to thank explicitly, here.

I am deeply grateful to my doctoral advisor Prof. Dr. Dieter Langosch for the great supervision during this work – and a long time afterwards. The thoughtful discussions with you were one-of-a-kind and will be missed. I wish you all the best and hopefully a lot of upcoming boating trips.

Then, I want to thank Walter Stelzer for teaching me everything about mass spectrometry and beyond. On top of that, I owe you so much for keeping the instrument running all the time.

The tremendous software solution of Prof. Dr. Martin Wozny allowed me to evaluate this huge amount of MS-spectra. Without your contribution, this project would not have been possible.

Many of my findings in this work would be short of context without the contributions of cooperating colleagues from other departments. Special thanks go out to Dr. Alexander Götz and Dr. Christina Scharnagl for their MD simulations, as well as to Dr. Nadine Werner and Gökhan Güner plus their supervisors Prof. Harald Steiner and Prof. Stefan Lichtenthaler, for providing cleavage data of our investigated peptides.

Further, I would like to appreciate the work of the students that I could supervise during my time as a PhD candidate, Felix Kuhne and Iro Chaitoglu.
Also, I am very thankful to my colleagues at the Chair of Biopolymer Chemistry, especially the "BioBears", for the pleasant work environment. It was truly a joy to work, discuss and party with you over the years.

Of course, all this would not have been able without the loving support of my family.
Finally, I want to thank Laura Enzmann from the deepest of my heart for supporting me in every imaginable and unimaginable way so that I could finalize this project. I look forward to all the challenges and adventures that we will master in the future.

Content

1 Introduction

1.1 Transmembrane proteins and intramembrane proteolysis

Integral membrane proteins play an essential role in all cells, as they mediate some of the most important cell functions via receptors, transporters, ion channels or soluble N-ethylmaleimide-sensitive factor attachment protein receptors (SNAREs). The most important subgroup of integral membrane proteins are transmembrane proteins that pass the lipid bilayer with at least one transmembrane domain (TMD) (single-span transmembrane proteins) or more (multi-span transmembrane proteins).

Depending on their orientation in the membrane, single-pass transmembrane proteins are classified into type I with the carboxyl-terminus (C-terminus) facing the cytosolic site and type II with an inverted topology, thus the amino-terminus (N-terminus) positioned towards the cytosol [1] (Figure 1A).

The thickness of the lipid bilayer, as well as its hydrophobic interior are the reason that TMDs normally consist of approximately 20 amino acids (AA), which are predominantly non-polar. Due to the absence of water inside the hydrophobic bilayer, the peptides form α-helices by establishing intramolecular main chain - main chain hydrogen bonds (H-bonds) between the amide-groups at position *i* and the carbonyl-oxygens at (usually) *i-4* [2] (see Figure 1B) or *i-3* (3_{10} helix, about 10% of all helices).

In the rare case of porins in gram-negative bacteria [3], transmembrane proteins can also form β-barrels, consisting of eight to twenty-two beta strands, mostly arranged in an antiparallel fashion [4] (Figure 1A).

Proteolysis of transmembrane proteins inside their TMD is a fundamental process in every cell and is found in all kingdoms of life [5–8]. This includes secretion of growth factors, critical signaling events or membrane protein turnover [9]. Malfunctions in the proteolysis of TMDs can cause severe diseases like various types of cancer [10–13], Alzheimer's or Parkinson's Disease [5,14]. The cleavage of TMDs is catalyzed by intramembrane proteases (IMPs) that harbor their active site in their own TMD regions as well [15].

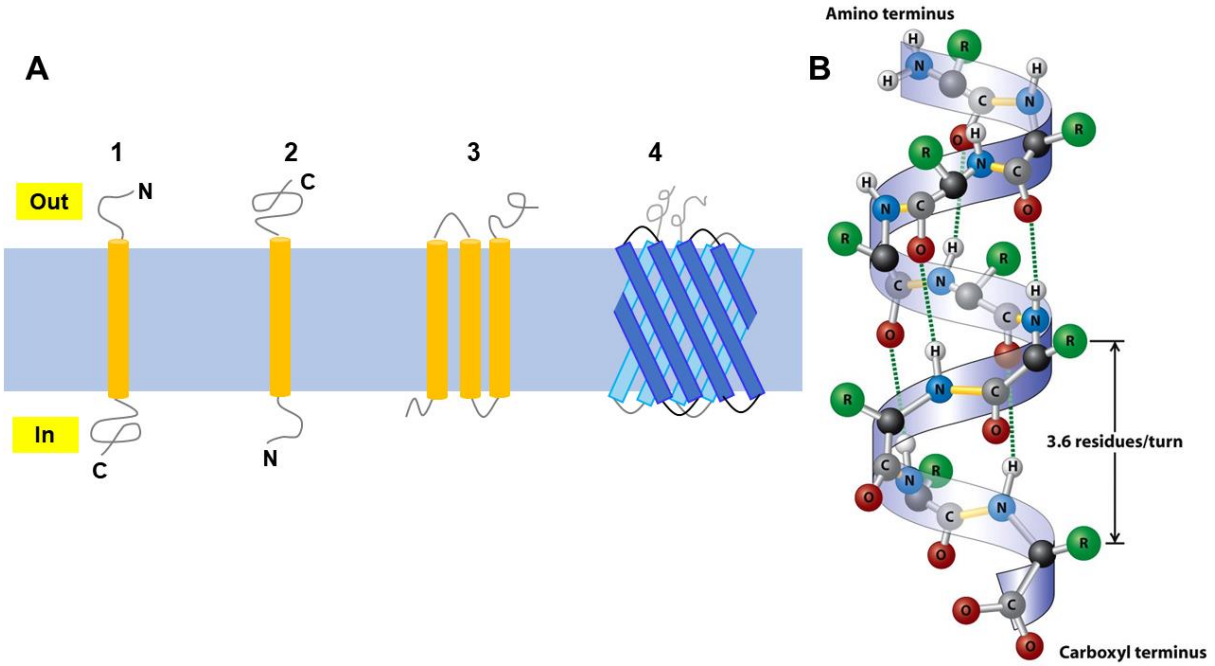

Figure 1: Schematic representation of transmembrane proteins.

A) 1) A single-span transmembrane α-helix of type I with N-out orientation. 2) A single-span transmembrane α-helix of type II with N-in orientation. 3) A multi-span transmembrane α-helical protein. 4) A polytopic transmembrane β-sheet protein. The membrane is represented in light blue.

B) Representation of an ideal α-helix. Green Rs denote amino acid side chains. A dotted line shows H-Bond between the hydrogen (white) from amide group at position *i* to the oxygen (red) of the carboxyl group at *i-4*. Figure B) adapted from Molecular biology of the cell (4th ed.) [16].

Today, four groups of IMPs are known that are distinguished by the residues in their active sites. Moreover, IMPs are also differentiated by their topology, i.e., their orientation in the membrane and consequently the orientation of their substrates (type I or type II transmembrane proteins, respectively).

The most prominent group are the aspartyl proteases with two aspartates in the active site. A well-known protease from this class is presenilin, the catalytic subunit of the Alzheimer's disease associated γ-secretase [5,17–19]. Representatives with an inverted topology relative to presenilin are the signal peptide peptidases (SPPs) and SPP-like proteases [5,20,21].

The second group that also occurs in different orientations are serine IMPs, also known as rhomboid proteases. They feature a characteristic Ser-His catalytic dyad in the active site [6,8,22].

Next, the metalloproteases are a group of IMPs, which rely on zinc-ions in their active site and comprise of site-2 protease (S2P) and S2P-like proteases [23,24].

The group that was most recently discovered, are the glutamyl proteases with only one known example, RCE1 (Ras converting CAAX endopeptidase 1) and a Glu-His catalytic dyad in its active site [25,26].

Apart from the fact that IMPs typically cleave their substrates in the TMD, little is still known about substrate discrimination and the cleavage process. Similar to soluble proteases, intramembrane proteolysis requires the sequential steps of substrate recognition, followed by the processing, cleavage and finally product release [27]. However, unlike most soluble proteases, IMPs do not recognize consensus sequences and the discrimination between substrates and non-substrates is still unclear. Also, kinetic studies have shown that intramembrane proteolysis is a slow process in the range of minutes and thus much slower than soluble proteases [28–32]. The reason for the slow kinetics is not yet understood. One explanation could be the slow access of the substrate's TMD into the active site of the enzyme, prior to the cleavage process.

1.2 Function and structure of γ-secretase

γ-Secretase is an aspartyl protease involved in the processing of type I single-span membrane proteins. Due to its involvement in the generation of Aβ-fragments from the Amyloid Precursor Protein (APP) and thus its connection to Alzheimer's disease [5], γ-secretase is arguably the most intensely studied intramembrane protease.

Next to APP, there are more than 149 substrates identified by now [33,34]. One noteworthy substrate is the cell surface receptor Notch1, where cleavage via γ-secretase plays a crucial role during the embryonic development and in adulthood, but also in the onset of various types of cancer [18,35,36]. Specifically, γ-secretase cleavage generates an intracellular domain (ICD) which is translocated to the nucleus and subsequently activates transcription of target genes [37]. This was first shown for Notch1, but similar signaling activities have been reported for other γ-secretase substrates [38,39].

ICDs from γ-secretase mediated cleavage were shown to activate or inactivate signaling pathways, depending on the substrate [38,40–42]. Consequently, regulation of signaling pathways by release of biologically active ICDs is a major function of γ-secretase. A second purpose could be the degradation of substrate C-Terminal Fragments (CTFs) that are left behind in the membrane after ectodomain shedding [43]. As observations with APP CTFs indicate, accumulation of these fragments can have toxic effects [44–48]. Thus, γ-secretase could serve a protective function by removing/cleaving these toxic CTFs.

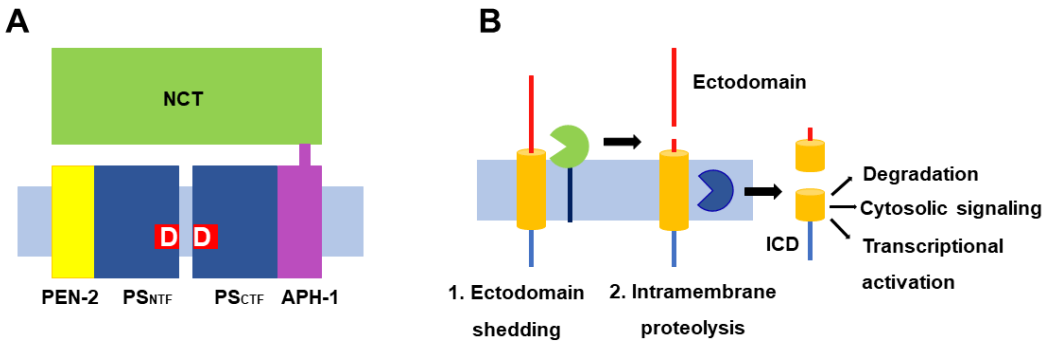

Figure 2: Structure and function of γ-secretase.

A) Arrangement of the four subunits of γ-secretase. Presenilin (blue) holds the two catalytic aspartates (Ds in red boxes) in its active center at TMD 6 (NTF) and TMD 7 (CTF). It is flanked by PEN-2 (yellow) and APH-1 (purple). Nicastrin (green) limits access to the complex via its bulky extracellular domain.

B) Schematic representation of intramembrane proteolysis via γ-secretase. First, ectodomains are shed by a membrane-bound protease (green). Subsequently, the remaining membrane-bound fragment is cleaved by γ-secretase (shown in blue). Afterwards, a small peptide gets released in the extracellular space and the intracellular domain (ICD) into the cytosol. The ICD may be further degraded, participate in cytosolic signaling or stimulate transcriptional activation of target genes. Figure B modified from Lichtenthaler *et al.*[5].

The γ-secretase protease is a complex composed of four subunits (Figure 2A):

Presenilin (PS), Nicastrin (NCT), anterior pharynx-defective 1 (APH-1) and presenilin enhancer 2 (PEN-2) [49–51]. PS is the catalytic subunit of the complex. It is a polytopic membrane protein with nine TMDs. The aspartate residues of the active site are located on TMD 6 and 7 [17,52,53]. Upon assembly and maturation of the γ-secretase complex [54], PS is cleaved stepwisely [55,56] by autoproteolysis [17,49,52,57] within the large cytoplasmic loop between TMD 6 and 7. This results in two fragments, the N-terminal fragment (NTF) comprising TMDs 1-6 and the C-terminal fragment (CTF) comprising TMDs 7-9 [58] . Presenilin occurs in two different homologs, presenilin-1 (PS1) and presenilin-2 (PS2), which can both contribute to the γ-secretase complex [59]. However, complexes with a certain variant of presenilin dominate in different subcellular regions. γ-Secretase complexes that contain PS1 are mostly located within the plasma membrane and in recycling endosomes, while γ-secretase complexes with PS2 are predominantly found in late endosomes and lysosomes [60,61].

NCT is the largest subunit of γ-secretase. It is a type I membrane protein [62] with a large and highly glycosylated extracellular domain, which covers the transmembrane part of the enzyme-complex [63]. Recent studies showed that this extracellular domain serves as a gatekeeper for type I membrane proteins prior to entering the protease complex, as only substrates with an appropriately short ectodomain fit underneath it [64].

APH-1 is a polytopic membrane protein with seven TMDs that stabilizes the structure of the complex. Similar to presenilin, APH-1 exists in two different variants that are part of separate complexes, namely APH-1a and APH-1b [65,66].

PEN-2 has a regulatory function and is the smallest subunit of the complex [67,68] with two hydrophobic domains. While the first one forms a straight TMD, the second domain features a hairpin-like structure with two half-helices embedded in the membrane [69,70].

The structure of the γ-secretase complex has recently been solved at atomic resolution by cryo-electron microscopy (Figure 3) [71]. Moreover, three different apo-states were identified in the atomic cryo-EM structures [72]. They show considerable conformational heterogeneity, particularly in the orientation of TMD 2 and 6 of presenilin, as well as a high flexibility of PEN-2 in the complex [72].

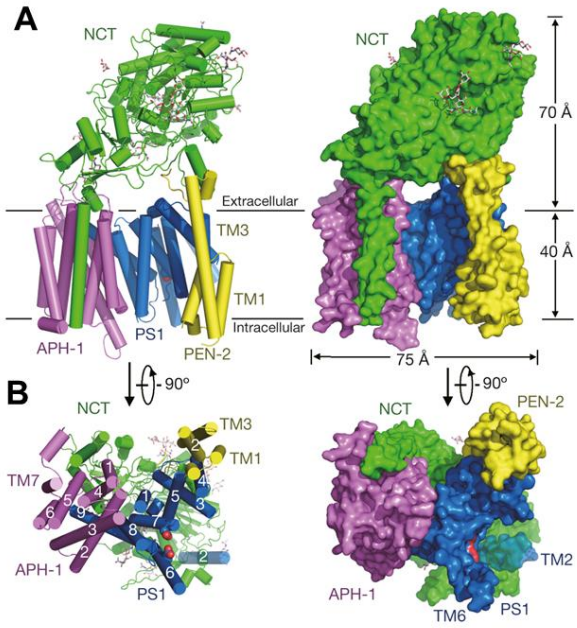

Figure 3: Atomic structure of human γ-secretase.

Atomic structure of human γ-secretase, acquired by Bai *et al* via cryo-electron microscopy (pdb code 5a63). γ-Secretase is shown from the side (A) or along the membrane, normal to the intracellular side (B) in cartoon representation (left) and surface view (right). Corresponding to Figure 2, PS1 is shown in blue with the active site in red, PEN-2 in yellow, APH-1 in purple and NCT in green. Figure adapted from Bai *et al.*[71].

All substrates of γ-secretase are type I membrane proteins, thus with an extracellular N-terminus and an intracellular C-terminus. Besides that, it is currently unknown what defines one of the over 1.500 type I membrane proteins as a substrate or a non-substrate. Substrates are

typically cleaved at specific positions in their sequence. However, they share no consensus sequence.

One crucial feature that all substrates share are short ectodomains, mostly of 15-30 amino acids. This length is typically achieved by ectodomain shedding via proteases like metalloproteases of the ADAM (a disintegrin and metalloprotease) family [73]. There are also substrates like BCMA (B-cell maturation antigen) with naturally short ectodomains, which do not require ectodomain shedding [74]. However, not all type I membrane proteins with short ectodomains are automatically cleaved by the γ-secretase [75].

Still, cleavability of substrates generally correlates inversely with the length of the ectodomains. The shorter the ectodomains are, the better the substrates are cleaved [64,76]. In contrast, substrates with ectodomains of more than 50 amino acids become increasingly less cleavable [77]. As mentioned earlier, the large globular extracellular domain of NCT is expected to block membrane proteins with longer ectodomains from getting in contact with the protease complex [64]. This is underlined by the observation that antibodies against the NCT ectodomain can block substrate binding and catalysis [78,79].

1.3 The amyloid precursor protein (APP)

The amyloid precursor protein is a single pass transmembrane protein with type I topology and a length of 695 amino acids [80]. As its name points out, APP is sequentially processed by transmembrane proteases to amyloid-β peptides (Aβ) which are prone to aggregate into amyloid plaques. These plaques in turn, are seen as a hallmark in the onset of Alzheimer's disease [81]. Although aging is considered to be the most important risk factor for this disease, Alzheimer's disease can also be genetically inherited, termed Familial Alzheimer's Disease (FAD). FAD is usually caused by one, or more, point mutations in the proteins of the γ-secretase complex or APP and is associated with a much earlier onset of the disease.

The first cleavage step of APP during the amyloidogenic pathway is carried out by the membrane-bound aspartyl protease BACE (β-site APP-cleaving enzyme), a component of the β-secretase complex [82]. This cleavage removes most of the APP ectodomain and leaves a 99 amino acid C-terminal fragment in the membrane, termed C99 (Figure 4).

In a second step, the C99 fragment is then cleaved at ε-sites in its TMD [19] by γ-secretase. This results in the release of the APP intracellular domain (AICD) from the membrane into the cytosol.

The remaining TMD is stepwisely trimmed by additional γ-secretase cleavages at the ζ- and γ-sites [83] before fragments are released in the extracellular space or lumen, respectively. This

generates a variety of Aβ forms, predominantly ranging between 38-42 amino acids in size. This is explained in detail in chapter 1.4.

Next to the initial cleavage by β-secretase, there is an alternative non-amyloidogenic pathway in which APP is cleaved by α-secretase [84]. This results in a cleavage within the Aβ region, generating a shorter APP C-terminal fragment, C83. This fragment is further processed by γ-secretase, resulting in the release of AICD and the extracellular fragment p3 [85–87].

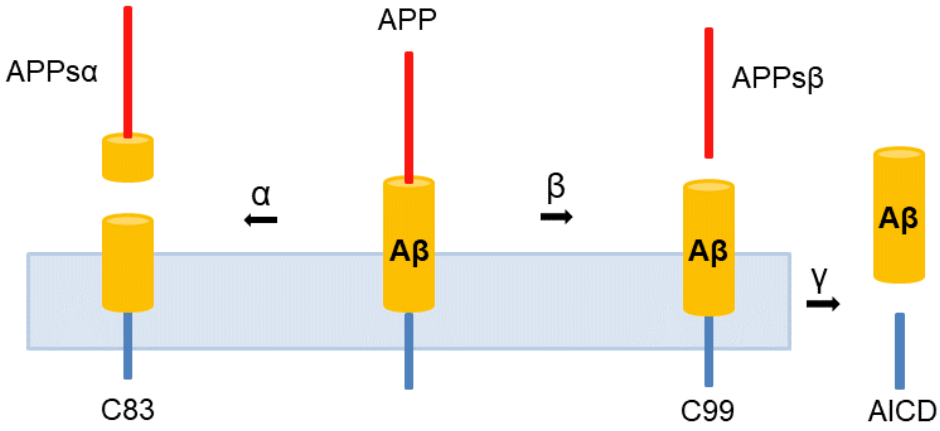

Figure 4: Processing of APP by α-, β- and γ-secretase.

APP is cleaved in two competing proteolytic pathways. Processing by α-secretase cleaves APP in its TMD and results in the soluble APP ectodomain APPsα and the non-amyloidogenic C-terminal fragment C83.

By analogy, cleavage by β-secretase generates the soluble APP ectodomain APPsβ and the membrane-bound C-terminal C99 fragment. C99 is subsequently cleaved by γ-secretase, generating the Aβ-peptides and the AICD.

1.4 Cleavage of C99 by γ-secretase

After shedding of the APPs ectodomain by β-secretase, the resulting C99 fragment is small enough in size to fit under the large globular extracellular domain of NCT that acts as a gatekeeper for γ-secretase [64]. In the following recognition process, the substrate gains access to the active site stepwisely via sequential interactions with exosites.

Photocrosslinking experiments showed that the first interaction of C99 and γ-secretase is mediated by exosites at NCT and PEN-2. Subsequently, the substrate binds to exosites of the PS1 NTF domain, which also harbors the majority of substrate binding sites. In a third step, C99 enters the catalytic cleft of PS for proteolysis [88].

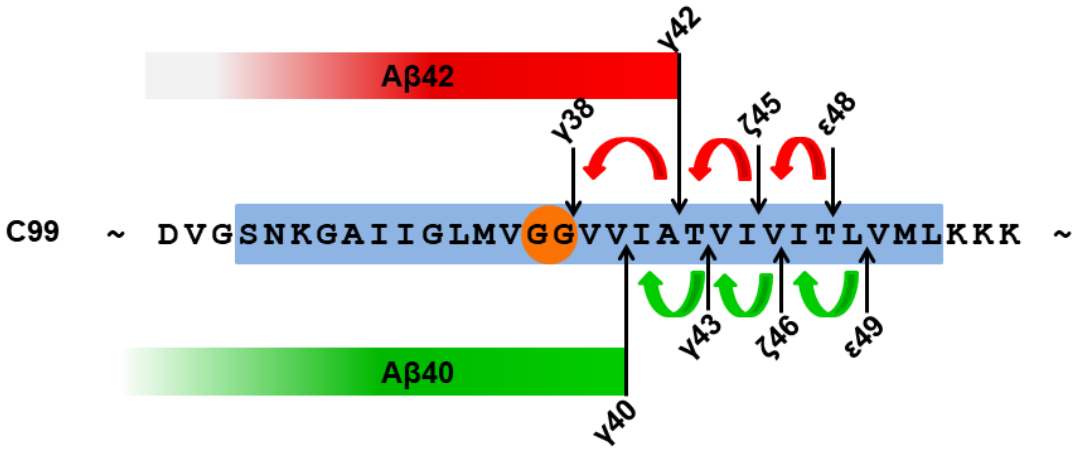

Figure 5: Stepwise cleavage of C99.

Part of the C99 sequence is shown with the TMD marked by the blue box. The hinge region is highlighted in orange. Both cleavage pathways are depicted with arrows pointing to the respective cleavage sites. The Aβ42 pathway is indicated in red and contains the cleavage sites ε48-ζ45-γ42(-γ38). The Aβ40 pathway is depicted in green with the cleavage sites ε49-ζ46-γ43-γ40.

Figure 5 shows the sequence of the C99 TMD, together with the respective cleavage sites of γ-secretase. The C99 TMD can be split into two parts. First, the N-terminal homodimerization region from S26 to V36, termed TM-N. Second, the C-terminal region (TM-C) from V39 to M51 that harbors the cleavage region. As proteolysis by aspartate proteases, such as the γ-secretase, requires unfolding of the substrate TMD [89,90], TM-C was initially expected to be quite flexible.

However, Deuterium-Hydrogen-Exchange (DHX) experiments revealed that the backbone flexibility of the TM-C helix is very low and comparable to that of non-substrates, while the TM-N helix shows a higher flexibility [91–93]. This is congruent with studies performed via NMR [94].

Both regions are linked by a highly flexible hinge motif, induced by the G37G38 sequence. This hinge was identified in NMR measurements as well as in molecular dynamics simulations with micelles, isotropic solution and lipid membrane as environments [93,95–101]. It was shown that the hinge plays a significant role in overall TMD helix dynamics between TM-N and TM-C and may provide the necessary flexibility to access the active site of γ-secretase [27,93,99,101,102]. For example, MD simulations suggested that the G37G38 hinge coordinates large-scale bending movements of the C99 TMD that may facilitate fitting of the TM-C domain into the active site of γ-secretase [103].

The relevance of the hinge is also underlined by studies with one exceptionally severe FAD mutation of C99, T43I, in the vicinity of the cleavage sites in TM-C. This mutation does not destabilize H-bonds at the ε-sites, but rather has a major impact on the stability of the upstream region around the G37G38 hinge [91].

The initial cleavage of C99 by γ-secretase occurs via endoproteolysis at ε-sites [104–107], leading to the release of the AICD, followed by stepwise carboxyterminal trimming [108–110] at the ζ- and γ-sites [83], releasing tri- and rarely tetrapeptides.

Depending on whether the initial cleavage occurs at position ε48 or ε49, there are two pathways for the proteolysis of the remaining Aβ fragment. The major pathway starts with the production of Aβ49, followed by the intermediates Aβ46 and Aβ43 and ends with the Aβ40 peptide. The minor pathway starts with Aβ48 and results in Aβ42, with only one intermediate, Aβ45. In both pathways, cleavage can continue further to generate the shorter peptides Aβ38 and Aβ37, respectively.

One highly cited model for the sequential release of the tripeptides proposes the existence of three amino-acid-binding pockets (S1´ to S3´) in the active site of γ-secretase, where the central S2´ pocket is smaller than the outer two (S1´ and S3´) [111]. Fitting of the substrate in these pockets is required to establish a stable enzyme-substrate scission complex and define cycles of the sequential cleavage. Thus, the "large-small-large" pattern of the pockets was proposed to represent a steric requirement for the sequence of respective substrates by prohibiting a large amino acid side chain at the central position. Bolduc *et al.* supported their theory by mutating phenylalanine (with a very large side chain that does not fit into the supposedly small S2´ pocket) into several positions of the cleavage region and thus successfully enforced cleavage pathways that avoided a misalignment of the large side chain with the small pocket. This means they could predict the preferred cleavage pathway based on the fit of the respective peptide into their pocket model.

However, there are FAD mutations, like I45T, that clearly contradict this model. ε-Site preference is not shifted for this FAD mutation [111] and the smaller side chain of T45 should fit even better in the small S2´pocket during the second step of the ε49-ζ46-γ43-γ40 pathway. Yet, this FAD mutant shows clear signs of a pathway switch after the initial cleavage [111–113].

The two alternative cleavage pathways of C99 in γ-secretase have drastically different consequences. As the Aβ42 is longer and more hydrophobic than Aβ40, its propensity to form neurotoxic aggregates is significantly larger. Accordingly, Aβ42 is the predominant Aβ form in the neurotoxic plaques that are related to Alzheimer's Disease [114,115], even though it is only generated at minor amounts. Aβ42's contribution to Alzheimer's Disease is supported by the fact that most genetic mutations that are related to FAD are located on APP and presenilin [116–118] and shift the Aβ42/Aβ40 ratio towards a higher Aβ42 level [119–121].

The vast majority of FAD mutations are located on PS1. They all increase the ratio of Aβ42/43 to Aβ40 [120,122] but there are multiple reasons for that. Changes in the processivity of the enzyme, as well as different ε-site selection with a shift towards the ε48 pathway are two causes that can also occur in combination [112,123–125]. Furthermore, alterations in substrate positioning have been reported [88], as well as a higher dissociation rate of Aβ42 and Aβ43 from the γ-secretase complex [126,127].

However, there are also several reported point mutations across the TMD of APP that are associated with FAD [128] and increase the Aβ42/Aβ40 ratio [112,129–132]. This is caused by a shift towards the pathologic ε48-ζ45-γ42 pathway [112,133], either at the initial cleavage [112,133] or in the downstream processing [108,109,111,134,135]. In addition, FAD mutations in the APP TMD also affect cleavage efficiency. While there are a few reported mutations like V46I that show increased cleavage efficiency, most FAD mutations decrease it [111–113].

To conclude, processing of C99 is sequence specific, which has also been reported for other substrates of γ-secretase [136], albeit they share no consensus sequence. Moreover, point mutations in the C99 TMD affect both cleavage efficiency and site specificity. Thus, there must be hidden molecular properties within the TMD helices that define substrates as such. Specifically, certain conformational characteristics in the structure and/or the dynamics of substrate TMD helices may affect recognition and cleavage by the γ-secretase.

1.5 How structural properties of substrate TMD can affect proteolysis

So how, and during which step, could conformational flexibility of a substrate TMD affect processivity in γ-secretase?

To answer this question, it is necessary to remember the successive steps in the mechanism of intramembrane proteolysis, their implication for the kinetics of the proteolysis, and to estimate how this can be linked to the diverse kinetics of different substrates or FAD mutants.

As described earlier, the first step of intramembrane proteolysis is substrate recognition and binding. To enter the proteolytic pathway, a substrate must bind long enough to its enzyme, otherwise it just dissociates without being cleaved. Consequently, the strength of substrate-enzyme interaction affects the overall reaction rate.

The strength of this interaction, i.e. the affinity of the substrate to the enzyme, is reflected by K_D in the Michaelis-Menten mechanism. Under the given circumstances of a turnover rate k_{cat} that is much smaller than K_D, the latter can be simplified to the Michaelis-Menten constant K_M, which, in turn, can be measured in experiments [28–30].

Subsequent to the substrate recognition step, the substrate is processed which includes the three consecutive steps of first, transport of the substrate to the active site; second, substrate unfolding at the cleavage site(s) plus the actual hydrolysis; and third, the release of the product(s).

The processing is characterized by k_{cat}, which is derived from the maximal reaction velocity V_{max} that can be measured in experiments. However, it is not possible to distinguish the impact of each single processing step on k_{cat} [27].

Chávez-Gutiérrez, De Strooper and their colleagues compared different substrates of γ-secretase and found that V_{max} as well as K_M values differ up to ~5-fold between the substrates [112]. This suggests that the substrate sequence influences its recognition and its processing to a similar extent.

Indeed, recognition of the substrate might be affected by the flexibility of its TMD. The exact mechanism of substrate recognition is not fully understood yet, but likely involves TMD-TMD interactions between the substrates and one or more exosites of the enzyme. It is possible that there is a selection, based on the conformation of the substrate TMD or a required induced fit. In both cases, a certain conformational flexibility of the helix, like bending or the fraying of termini, might be a requirement for substrate selection.

However, regarding the effect of TMD flexibility on cleavage efficiency, substrate processing is probably the more interesting target to investigate, especially with the effects of TMD-located FAD mutations in mind:

First, reported k_{cat} values for intramembrane proteolysis are several magnitudes slower than k_{cat} of soluble proteases. As described earlier, k_{cat} is directly linked to the processing of the substrate. Specifically, *in vitro* studies revealed k_{cat} values of $0.0012s^{-1}$ for the cleavage of C99 in γ-secretase [29] or 0.0083-0.0096 s^{-1} for Notch1 substrates [64]. In contrast, soluble proteases range around k_{cat} rates >1 s^{-1} [137] (https://www.brenda-enzymes.org).

Second, Chávez-Gutiérrez *et al.* showed that V_{max}, which can be taken as k_{cat} in their setting, is heavily affected by FAD mutations in the C99 TMD [112]. This indicates that already slight variations in the TMD's flexibility, caused by altered side chain interactions of the mutated residues, can lead to severe changes in the cleavage efficiency. Additionally, most FAD mutations in the C99 TMD also change site-specificity towards ε48. It seems plausible that the origin for this change in site-specificity occurs during the processing and not already at the recognition step.

But which step of the substrate processing might explain these observations?

Soluble proteases show that the chemistry of peptide bond hydrolysis itself is very fast and consequently is not the cause for the slow reaction kinetics [137].

Little is known about the mechanism and the kinetics of the product release. However, the reported k_{cat} values for the cleavage of C99 and its FAD mutants in γ-secretase are based on the release of the AICD-fragment, thus after the initial cleavage at ε48 or ε49. Yet, many severe FAD mutations, like T43I, which also hamper cleavage efficiency, are located one to two turns upstream of the initial cleavage site. Cleavage requires disruption of the helical secondary structure, at least around the cleavage site [90]. It is unclear, how altered side chain interactions or backbone flexibility in the remaining Aβ-fragment, induced by the FAD mutations, might then affect the release of the cleaved-off AICD-fragment. Consequently, product release is also not rate limiting, which leaves the refolding of substrate and enzyme to expose the substrate's scissile bond to the active site as the last option.

Which impact could TMD flexibility have on this step?

The obvious idea is that a high flexibility in the C-terminal region of the substrate TMD enables transient unfolding of the helix around the scissile bond, prior to cleavage. This is expected, as the aspartate proteases rely on a proton transfer to the carbonyl oxygen of the scissile bond [89]. This proton transfer, in turn, is only possible, when the respective carbonyl oxygen loses its intrahelical hydrogen-bond, at least temporarily [90].

First, NMR spectrometry experiments with artificial C99 mutants seemed to confirm this idea. Insertion of three helix-promoting leucine residues one helical turn downstream of the ε-site

prevented unraveling of the scissile bond and reduced cleavage efficiency (indicated by a lower production of both AICD and Aβ40) [123]. Moreover, this insertion also caused higher levels of Aβ42, which implies a shift of the initial cleavage site or in the cleavage pathway [138]. Insertion of an unstructured triple glycine motif at the same position had no major effect on TMD helix stability or substrate cleavage [123].

In a similar approach, Fernandez *et al.* [139] mutated I47 and T48 to helix promoting Leu or destabilizing Gly residues. These mutations resulted in reduced cleavage efficiency (Leu mutation) or enhanced cleavage efficiency (Gly mutation), respectively. Fernandez *et al.* ascribed this to the assumed alterations in helix flexibility around the ε-site.

Also, comparable conclusions were drawn from NMR studies with the two FAD mutations V44M and V44A. Both mutations increase the Aβ42/ Aβ40 ratio [112,129,132] by a shift of the preferential ε-site towards ε48 [112,140]. Chen *et al.* linked this to their observation of weakened H-bonds emanating from the T48 amide nitrogen, compared to the wildtype, caused by the mutations of V44 [94]. Yet, they did not provide an explanation, how weakened H-bonds emanating from the amide group of T48 could facilitate cleavage at this position, as the proteolytic process relies on the carbonyl oxygen, not the amide group. Rather, weakened H-bonds emanating one turn downstream, from L52 to T48 could explain a shift of the ε-site selection.

However, later studies with DHX experiments and MD simulations proved that TM-C, including the ε-site, is actually more rigid than the TM-N region [93,99,103] and even less flexible than several non-substrate TMDs [92]. Additional studies showed how the mutations T43V and T48V affect the cleavage and site specificity via their impact on helix bending [103]. In detail, both mutations change the direction and the extent of bending of TM-N, relative to TM-C, via altered side chain to main chain interactions. The hydroxylated side chain of T43 establishes stabilizing H-bonds with the backbone carbonyl oxygens of the TMD, which are lost in case of the mutants. Again, decreased H-bond occupancies around the ε -site were not found.

Similar effects were observed for the severe FAD mutation T43I, where the effect of the altered side chain to main chain interactions is even propagated towards the hinge region [91].

Helix bending might consequently play a crucial role for cleavage specificity and efficiency.

In which way could substrate TMD helix bending affect the cleavage process prior to the hydrolysis?

Fukumori *et al.* showed with the example of C99 how a substrate of γ-secretase does not directly enter the active site of the enzyme but is rather transported towards the active site in a stepwise

manner. The initial binding occurs at the NCT/PEN-2 exosite, followed by binding to the PS1 NTF before the substrate accesses the active site in PS1 NTF/CTF [88].

A certain repertoire of TMD conformations might be necessary to enable this transfer pathway towards the active site and could pose a selective criterion for the discrimination between substrate and non-substrate. Also, a slower or faster transport could increase/decrease the cleavage rate, respectively.

Once the substrate enters the active site, the cleavage rate depends on how likely the scissile bond, the catalytic residues of the enzyme, and the catalytic water are juxtaposed at the right geometry [102]. Similar to the movements in the transfer pathway, certain conformational features of the TMDs, like bending or twisting, might facilitate or hamper the establishment of the right geometry prior to a successful cleavage. Thus, conformational flexibility again affects the cleavage rate.

Finally, this concept also provides an explanation for the altered Aβ42/Aβ40 ratios of FAD mutants, which is mostly induced by a preferential use of ε48.

As already shown by Scharnagl *et al.* for V44A, V44M and T43I [91,103], FAD mutations alter the bending angles and the conformational repertoires of the C99 TMD. This might change their access to the catalytic aspartates and cause a mispositioning in the active center, leading to an increased use of the ε48 site.

This idea is supported by the photo-crosslinking experiments of Fukumori *et al.* They already showed that PS1 based FAD mutations alter the crosslinking sites with the C99 substrate. This in turn suggests a mispositioning of the substrate, favoring the ε48 pathway [88].

To sum up, there are good indications that conformational flexibility of the substrate TMD, with a special regard to helix bending, plays a major role in the discrimination of a substrate from a non-substrate, cleavage efficiency, and site specificity.

Yet, this does not imply that the stability of the H-bonds close to the cleavage site has no relevance at all. Recent cryo-electron microscopy studies revealed the structure of C83 bound to γ-secretase (Figure 6). The substrate, as well as the enzyme, undergo conformational changes and establish a hybrid β-sheet [141]. From the APP substrate, this hybrid β-sheet involves the residues from M_{51} to K_{54}. Thus, a high flexibility in the C-terminal region close to the initial cleavage site could be expected to facilitate helix unfolding, followed by β-sheet formation.

Though the results were obtained with C83, the structure of C99 can be expected to be identical, as they share the same sequence. Interestingly, very similar results were also obtained with Notch1 [142].

To further investigate the relationship between cleavage and conformational flexibility, I looked at the strength of the backbone H-bonds of the C99 TMD as well as several C99 TMD based peptides. These C99 TMD based peptides include FAD mutations as well as other artificial mutations, where cleavage ratios and/or cleavage efficiencies are already known from previous publications. In doing so, cleavage by γ-secretase can be linked to certain conformational properties of the substrate peptides.

Further artificial model substrates were introduced to identify the minimal requirements for a substrate of γ-secretase.

Based on the principle of DHX experiments, a sophisticated setup was developed to precisely distinguish the strength of the backbone H-bond of each single residue of the respective TMD-peptide. The idea and theory of this setup is described in the following chapters.

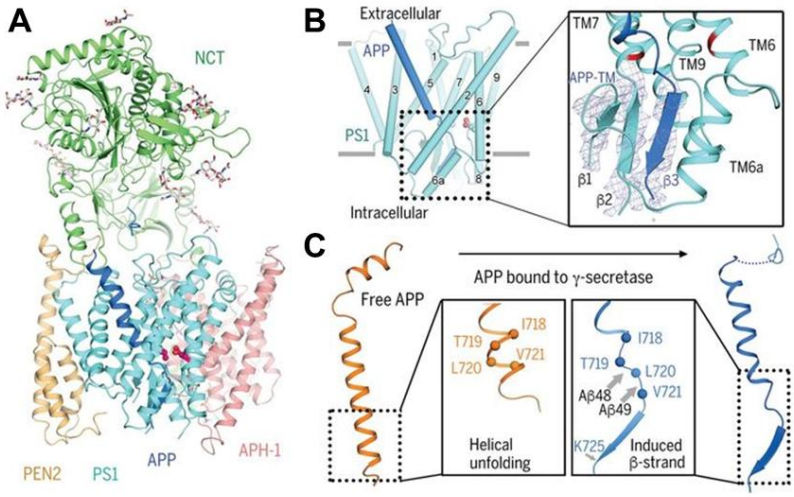

Figure 6: Atomic structure of human γ-secretase bound to C83.

A) Overall structure of the enzyme-substrate complex. B) Close-up view of the hybrid β-sheet established by β-strands of presenilin and one β-strand of C83. C) Structural comparison of free C99 (orange) and C83 bound to γ-secretase (blue) with the induced β-strand. Figure adapted from Zhou *et al* [141] and modified for this thesis.

1.6 Principles of DHX

DHX experiments are performed to investigate the stability of main chain hydrogen bonds in solution and by this getting insight into the conformational properties of proteins and peptides [143]. The principle is that labile deuterons/hydrogens on polar side chains or terminal groups exchange to hydrogen/deuterium practically immediately, while covalently carbon-bound deuterons/hydrogens do not exchange at all. Therefore, only the amide bound deuterons of interest remain measurable by this method.

In a stable helix, these amide bound protons at position *i* form intrahelical hydrogen bonds with carbonyl oxygens at position *i-4* (α-helix) or *i-3* (3_{10}-helix). However, deuterium exchange only occurs when the respective proton is currently not involved in a hydrogen bond. Hence, the stability of these hydrogen bonds determines the rate of exchange of amide bound protons. The less stable an H-bond is, the more time it spends in an "open" conformation, and the more likely it is that a proton exchanges. Consequently, a weak H-bond, which is associated with a higher conformational flexibility, is characterized by a faster exchange in DHX.

However, there are numerous aspects that affect the kinetics of DHX, both environmental and conformational that will be addressed in the next chapters. I will also explain how I managed to calculate exact H-bond strengths from the measured exchange data.

2 Theory

2.1 Sequence dependence of DHX at N-H groups

The exchange of deuterium to hydrogen first depends on the availability of a catalyst, as well as on the neighboring residues of the respective amide group.

The intrinsic exchange rate constant (k_{int}) of each amide deuterium is the sum of the acid-, water-, and base-catalyzed exchange constants (k_{acid}, k_{water} and k_{base}, respectively). k_{int} also depends on the local sequence context [144,145]. First, there are inductive effects of polar side chains that increase the acidity of the amide group and thus accelerate water- and base-catalyzed exchange while slowing down acid-catalyzed exchange. Second, steric effects of bulky side chains reduce the accessibility of the amide group towards the catalyst, which is especially pronounced for the β-branched amino acids Val and Ile. Due to the closer proximity, the steric effect of the side chain right of the amino group is larger than the one from the left residue.

Both the inductive and steric effects from the residues left and right of the respective amide group are independent from each other and can be multiplied to obtain the combined effect.

The effects of every side chain (inductive and steric combined) on both sides of an amide group were empirically determined for HDX [144] and later for DHX [145] reactions.

However, they were measured in context of unstructured Ala-based peptides. Steric effects of neighboring side chains might be different in context of a structured peptide or protein. Furthermore, solvents like TFE used in this work, might alter accessibility towards the catalyst in various ways for different side chains. Nevertheless, these values provide a reasonable basis for comparison of the peptides in this work.

So, k_{int} can be calculated as shown in equation (1) and equation (2):

$$k_{int} = k_{acid} + k_{base} + k_{water} \quad (1)$$

$$k_{int} = k_{acid,ref}(A_L \cdot A_R)[D^+] + k_{base,ref}(B_L \cdot B_R)[OD^-] + k_{water,ref}(B_L \cdot B_R) \quad (2)$$

$k_{acid,ref}$, $k_{base,ref}$, $k_{water,ref}$: Reference rate constants as determined for unstructured Ala-based peptides at 20°C [144,145]

A_L, A_R: Correction factors left and right of a side chain for acid catalyzed exchange

B_L, B_R: Correction factors left and right of a side chain for base and water catalyzed exchange

Calculations with sequences of the peptides used in this work reveal that at pH 4.0, the base-catalyzed exchange already contributes to 95% of the total k_{int}. At pH 5.0 and higher, this amount increases to > 99,5%. Simplified, in this work k_{int} mainly depends on k_{base} and [OD^-].

2.2 Temperature dependence of DHX

Exchange rate constants $k_{(x)}$ (for acid-, base-, and water-catalyzed exchange) also depend on the temperature. The change of the respective exchange rate constant at a certain temperature $k_{(x)T}$ can be estimated with the Arrhenius equation (equation (3)) [144,146,147] :

$$k_{(x)T} = k_{(x)293} \cdot \exp\left(-\frac{E_A(x)}{R} \cdot \left(\frac{1}{T} - \frac{1}{293}\right)\right) \quad (3)$$

$k_{(x)293}$: Exchange rate constant at 293 K (20°C)

T: Temperature in Kelvin

$E_A(x)$: Activation Energy

For base-catalyzed exchange, $E_A(x)$ (k_{OH^-}) = 17 kcal/mol = 71.2 x 10^3 J/mol

R: Gas constant; 8.314 J/ (mol · K)

Hence, changing the experimental settings by 1°C alters the exchange rate constants by 11%. Reducing the temperature from 20°C to 0°C (stop-conditions) results in an 8-fold decrease.

2.3 Thermodynamics and kinetics in DHX

The general deuterium exchange in native proteins dissolved in H_2O is described in the following scheme (equation (4), model originally proposed by Hvidt [148,149], modified here to fit DHX):

$$N_D \underset{k_{cl}}{\overset{k_{op}}{\rightleftharpoons}} U_D \overset{k_{ch}}{\rightleftharpoons} U_H \qquad N_D \xrightarrow{k_{exp}} U_H \qquad (4)$$

back exchange blocked in the absence of D

N_D, U_D: Deuterated amide group in native and unfolded state

U_H: Hydrogenated amide group in unfolded state

k_{op}, k_{cl}: Rate constants for conversions between folded and unfolded states

k_{ch}: Chemical exchange rate

k_{exp}: Observed exchange rate constant of an individual H-bond in an experiment

According to this model, a slowly exchanging deuterium is likely to reside in the closed (or folded) state, which hinders exchange. Occasionally, the protein experiences a motion that brings the amide deuterium to an open state where exchange is possible. This can be unfolding of the protein which facilitates access of the catalyzing OH^--ions or the opening of an H-bond. In the context of this work, where the peptides consist of only one helix, complexity is reduced to the opening and closing of H-bonds. The opening and closing motions proceed with the rate constants k_{op} and k_{cl}, respectively. These motions can be subdivided into two distinct types of motion. First, the low-energy local motions and second, high-energy global unfolding, which can both contribute to hydrogen exchange [150–154]. The actual exchange reaction occurs with the chemical exchange rate k_{ch}. As experiments are generally performed in a vast excess of H_2O, back exchange is essentially blocked.

So, the observed exchange rate constant (k_{exp}) of an individual H-bond depends first on the stability of this H-bond ($K_{op} = k_{op}/k_{cl}$) and second on the chemical exchange rate k_{ch}.

k_{ch} depends on the intrinsic exchange rate constant k_{int} (see chapter 2.1) and the concentration of the respective catalyst. As all measurements were performed at pH 4.0 or higher, exchange is essentially base-catalyzed and k_{ch} can be simplified to equation (5):

$$k_{ch} = k_{int} \cdot [OH^-] \quad (5)$$

Therefore, k_{ch} is directly proportional to $[OH^-]$, which allows tuning of the exchange reaction kinetics via pH (increasing the pH by 1 accelerates exchange by the factor of 10).

2.3.1 EX1 and EX2 kinetics

Basically, the exchange reactions occur between two kinetic limits, EX1 [150] and EX2 [148], depending on the stability of the protein and the pH of the solvent. The main conditions and consequences of these limits are compared in the following Table 1:

Table 1: Comparison of EX1 and EX2 regimes.

EX1 limit	EX2 limit
• **$k_{ch} >> k_{cl}$ → k_{op} is rate-limiting**	• **$k_{ch} << k_{cl}$ → k_{ch} is rate limiting**
• Requires that the protein is unstable and most of the time in the unfolded state (small k_{cl}) or very high pH (large k_{ch}).	• Requires the protein to be stable and predominantly in the folded state (large k_{cl}).
• Simultaneous exchange of several deuterons during the long-lived unfolded state. **→correlated exchange**	• Several rounds of unfolding and folding before exchange occurs. **→ uncorrelated exchange**
• The unfolding reaction via k_{op} is rate-limiting, so DHX is independent of pH.	• k_{ch} is rate-limiting and $k_{ch} = k_{int} \cdot [OH^-]$ so DHX = *f* (lg [pH]).
• Experimentally, EX1 kinetics are characterized by a decrease of the fully deuterated isotopic envelope, accompanied by the development of an isotopic envelope of the fully exchanged peptide [155].	• Experimentally, EX2 kinetics are characterized by a gradual shift of the isotopic [155] envelope with minimal peak broadening [156].

However, uncorrelated exchange is also possible under EX1 conditions, in case of local but long-lived fluctuations from the native state, where only single H-bonds can open and close. This can occur in addition to the correlated exchange. In the spectra, this might add a gradual shift of the isotopic envelope in addition to the development of the fully exchanged envelope [155,157].

As the relation between k_{ch} and k_{cl} is important for the differentiation between EX1 and EX2, not only the stability of the protein is important, but also the pH. For ubiquitin it was shown, how raising the pH from 5 to 9 increases k_{ch} by the factor of 10.000 and therefore shifts the exchange reaction from the EX2 limit to EX1 [158].

Additionally, there is an intermediate exchange regime between EX1 and EX2, called EXX [155]. In this state, the unfolded state is long-lived enough for multiple simultaneous exchanges, but too short for a complete correlated exchange. Therefore, the resulting envelope from the partially correlated exchange develops between the non-exchanged and the fully exchanged masses. The slower uncorrelated exchange then causes a gradual shift of this new isotopic envelope towards the fully exchanged state.

Exemplary isotope pattern shifts are shown in Figure 7.

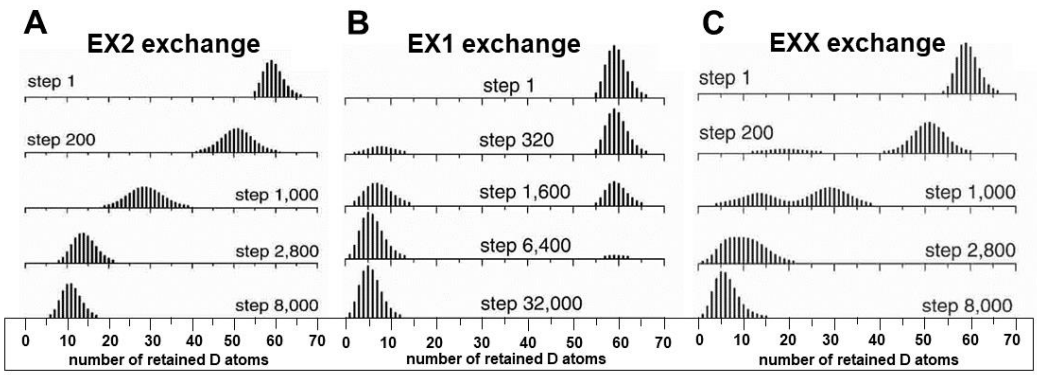

Figure 7: Simulated DHX patterns for two-state systems.

Simulations were carried out under A) EX2 conditions, B) EX1 conditions and C) EXX conditions with an overlap of EX1 and EX2 patterns. Model spectra adapted and modified from Xiao *et al.*[155]

In case of helices, global and local folding rates k_{cl} are ~10^6 sec^{-1} and ~10^{11} sec^{-1}, respectively, while k_{ch} is ~ 10 sec^{-1} at pH 7.0 [159]. Hence, closing rates of global and local folding vastly exceed k_{ch} and (native) helices are thought to always exchange in the EX2 limit.

2.3.2 Isotope effects

Previous experiments proposed an isotope effect where, depending on the D_2O/H_2O ratio in the solvent, strong H-bonds tend to accumulate protium, while weak H-bonds tend to accumulate deuterium [160–164]. This could also affect the kinetics of DHX and HDX experiments and as a result, compromise the calculation of H-bond strengths.

However, folding/unfolding experiments indicate that isotope effects mainly arise from enhanced hydrophobic interactions and increased strength of solvent-solvent H-bonds in D_2O [165]. In contrast, replacement of amide protons by deuterons does not affect the protein's stability during exchange experiments [165]. Also, studies on D/H amide isotope effects determined that deuterated helical H-bonds are only destabilized by 9 – 22 cal/mol, relative to protonated H-bonds [166,167]. As the stability of an intrahelical amide H-Bond is ~ 1 kcal/mol in water [168], these differences are negligible.

2.3.3 Calculation of H-bond strength with the Linderstrøm-Lang model

According to the model of Linderstrøm-Lang [169,170], the exchange rate constant can be calculated from the individual rate constants as shown in equation (6) [171]:

$$k_{exp} = \frac{k_{op} \cdot k_{ch}}{k_{ch} + k_{op} + k_{cl}} \tag{6}$$

For exchange in the EX2 limit with $k_{ch} << k_{cl}$, equation (6) can be simplified to equation (7):

$$k_{exp} = \frac{k_{op} \cdot k_{ch}}{k_{op} + k_{cl}} \tag{7}$$

By solving for k_{op}, equation (7) can be rewritten as equation (8):

$$k_{op} = \frac{k_{exp} \cdot k_{cl}}{k_{ch} - k_{exp}} \tag{8}$$

By inserting equation (8) into equation (9),

$$K_{op} = \frac{k_{op}}{k_{cl}} \tag{9}$$

K_{op} can be described as equation (10):

$$K_{op} = \frac{k_{exp}}{k_{ch} - k_{exp}} \tag{10}$$

So, with k_{exp} derived from EX2 measurements and calculated k_{ch} values, it is possible to determine K_{op}. This can be used to assess the Gibbs free energy (ΔG^0) of an H-bond, or, in other words, its strength, which is defined as in equation (11):

$$\Delta G^0 = -R \cdot T \cdot \ln(K_{op}) = -R \cdot T \cdot \ln\left(\frac{k_{exp}}{k_{ch} - k_{exp}}\right) \tag{11}$$

ΔG^0: Gibbs free energy

T: Temperature in Kelvin

R: Gas constant: 8.314 J/ (mol · K)

K_{op}: Stability constant, $K_{op} = k_{op}/k_{cl}$

Thus, deuterium exchange in the EX2 limit provides thermodynamic data and ΔG^0 of each H-bond can be determined.

2.3.4 Kinetic model of DHX

When calculating k_{exp} from experimental data, it is necessary to look at a kinetic model, similar to the model from 2.3 but also with the equilibrium between protonated peptide in the unfolded and the folded state (equation (12)):

$$F_D \underset{k_{cl}}{\overset{k_{op}}{\rightleftharpoons}} U_D \underset{k_{H\to D}}{\overset{k_{D\to H}}{\rightleftharpoons}} U_H \underset{k_{op}}{\overset{k_{cl}}{\rightleftharpoons}} F_H \tag{12}$$

F_D, U_D: Deuterated amide group in folded and unfolded state

F_H, U_H: Hydrogenated amide group in folded and unfolded state

k_{op}, k_{cl}: Rate constants for conversions between folded and unfolded states

$k_{D\to H}$: Rate constant for hydrogenation of U_D

$k_{H\to D}$: Rate constant for deuteration of U_H

As a value of 100% D_2O or H_2O, respectively, is not practicable in experiments due to the dilution of the sample into an exchange solvent of the opposite isotope type, this must be considered while calculating the chemical exchange rate. So, the rate constants $k_{D\to H}$ and $k_{H\to D}$ are proportional to the ratio of deuterated and hydrogenated exchange solvent, shown in equation (13 a) and (13 b):

$$k_{H\to D} = k_{ch} \cdot D_{asymptotic} \tag{13 a}$$

$$k_{D\to H} = k_{ch} \cdot \left(1 - D_{asymptotic}\right) \tag{13 b}$$

$D_{asymptotic}$: Expected degree of deuteration that is asymptotically approached for exceedingly long exchange periods. This value equals the ratio of deuterated to hydrogenated solvents in the exchange reaction volume. So, for experiments where 5% of a deuterated peptide solution is mixed with 95% hydrogenated exchange solvent, the value is 0.95.

For a better understanding of the dynamic system, some additional quantities have to be defined:

f_D, u_D: Concentration of the peptide with the deuterated amide group in its folded and unfolded state, respectively

f_H, u_H: Concentration of the peptide with the hydrogenated amide group in its folded and unfolded state, respectively

$c_D := f_D + u_D$: Concentration of the peptide with the deuterated amide group, regardless of the folding state

$c_H := f_H + u_H$: Concentration of the peptide with the hydrogenated amide group, regardless of the folding state

$c_P := c_D + c_H$: Total concentration of the peptide, regardless of the folding state and the amide group

As the exchange reactions are performed in the EX2 limit, $k_{D\rightarrow H}$ and $k_{H\rightarrow D}$ are much smaller than k_{op} and k_{cl}. Hence, the influence of $k_{D\rightarrow H}$ and $k_{H\rightarrow D}$ on the ratio of f_D and u_D is negligible and the ratio only depends on the quotient of k_{cl} and k_{op}. This is shown in equation (14):

$$\frac{f_D}{u_D} = \frac{k_{cl}}{k_{op}} \tag{14}$$

In an analog way, this applies to f_H and u_H.

To solve the differential equation resulting from the reaction scheme (12), the quantities of u_D and u_H are necessary. These quantities can be defined by the constant overall protein concentration c_P and the time dependent concentration of peptides with the deuterated amide hydrogen, c_D (equation (15 a) and (15 b)):

$$c_D = u_D + f_D = u_D \cdot \left(1 + \frac{k_{cl}}{k_{op}}\right) \tag{15 a}$$

$$\rightarrow u_D = c_D \cdot \left(1 + \frac{k_{cl}}{k_{op}}\right)^{-1} \tag{15 b}$$

Analog for c_H (equation (15 c) and (15 d)):

$$c_H = c_P - c_D = u_H + f_H = u_H \cdot \left(1 + \frac{k_{cl}}{k_{op}}\right) \tag{15 c}$$

$$\rightarrow u_H = (c_P - c_D) \cdot \left(1 + \frac{k_{cl}}{k_{op}}\right)^{-1} \tag{15 d}$$

With equation (13 a) and (13 b), as well as (15 b) and (15 d), the reaction scheme (12) can be expressed as a first order differential equation (16), based on the change of c_D over time:

$$\begin{gathered} \frac{d}{dt} c_D(t) = \frac{d}{dt} u_D(t) = \\ (-k_{D\rightarrow H} \cdot u_D + k_{H\rightarrow D} \cdot u_H) = \\ k_{ch} \cdot \left(-\left(1 - D_{asymptotic}\right) \cdot c_D \cdot \left(1 + \frac{k_{cl}}{k_{op}}\right)^{-1} + D_{asymptotic} \cdot (c_P - c_D) \cdot \left(1 + \frac{k_{cl}}{k_{op}}\right)^{-1}\right) \\ = \left(\frac{k_{op}}{k_{op} + k_{cl}}\right) \cdot k_{ch} \cdot (D_{asymptotic} \cdot c_P - c_D) \end{gathered} \tag{16}$$

Together with equation (7), equation (16) can be expressed as equation (17):

$$\frac{d}{dt} c_D(t) = k_{exp} \cdot (D_{asymptotic} \cdot c_P - c_D) \tag{17}$$

The general solution of equation (17) is the function of $c_D(t)$ (equation (18)) that contains a constant C, needed for adjusting the initial conditions:

$$c_D(t) = D_{asymptotic} \cdot c_P + C \cdot e^{-k_{exp} \cdot t} \tag{18}$$

During DHX, at t = 0, the overall concentration of peptides with deuterated amide hydrogens c_D equals the total concentration of peptides c_P (equation (19)):

$$c_D(0) = c_P \rightarrow C = \left(1 - D_{asymptotic}\right) \cdot c_P \tag{19}$$

Consequently, with equation (18) and (19) the amount of peptides with a deuterated amide group, relative to the total peptide concentration at a certain time, is described as in equation (20):

$$\frac{c_D(t)}{c_P} = D_{asymptotic} + \left(1 - D_{asymptotic}\right) \cdot e^{-k_{exp} \cdot t} \tag{20}$$

In case of the experiments in this work, this equation finalizes to equation (21):

$$D(t) = 0.05 + 0.95 \cdot e^{-k_{exp} \cdot t} \tag{21}$$

With D(t) as the measured respective number of deuterons for a fragment at a certain time point.

For HDX, the initial concentration of peptides with a deuterated amide group = 0, so equation (18) is solved via equation (22) and (23):

$$c_D(0) = 0 \rightarrow C = -D_{asymptotic} \cdot c_P \tag{22}$$

$$\frac{c_D(t)}{c_P} = D_{asymptotic} - D_{asymptotic} \cdot e^{-k_{exp} \cdot t} \tag{23}$$

2.4 Fragmentation of peptides in mass spectrometric analysis

To obtain residue specific exchange kinetics, it is necessary to fragment the peptides after the DHX reaction. In modern mass spectrometry, fragmentation of peptides plays a key role, as it allows bottom-up proteomics, sequencing, and conformational investigations. There are several fragmentation methods, which lead to different dissociation products (see Figure 8). During this study, collision-induced dissociation (CID) and electron-transfer dissociation (ETD) were used. The mechanisms of both methods are explained in 2.4.1 and 2.4.2, respectively, as the understanding is crucial for interpretation of the fragmentation results.

In CID, fragmentation is caused by mobile protons, facilitated by vibrational excitation. This leads to cleavage of the peptide bond and results in b- and y-ions (see Figure 8). In case of ETD, an electron is transferred from a radical anion reagent to the peptide upon collision, which finally causes dissociation of the peptide. Cleavage occurs between the amide nitrogen and the subsequent C_α, producing c- and z-ions.

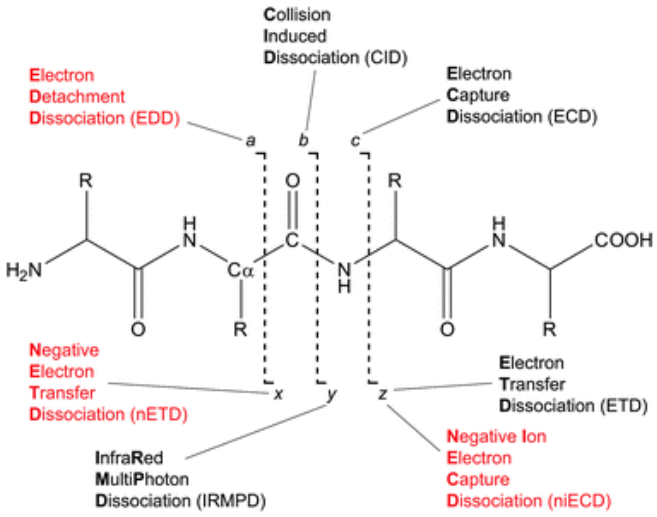

Figure 8: Cleavage products as results from different fragmentation methods.

In this work, ETD was applied to obtain c- and z-fragment ions, as well as CID for b- and y-fragment ions. Figure adapted from Zhurov *et al.* [172].

Regarding DHX analysis, one problem with fragmentation is the so-called scrambling [173,174]. Scrambling describes intramolecular hydrogen (H^1/H^2) migration, due to vibrational/collisional excitation. This renders the obtained results useless, as the original H^1/H^2 labeling pattern is lost (see Figure 9). Hence, a suitable fragmentation method, like ETD, must be chosen [175–177].

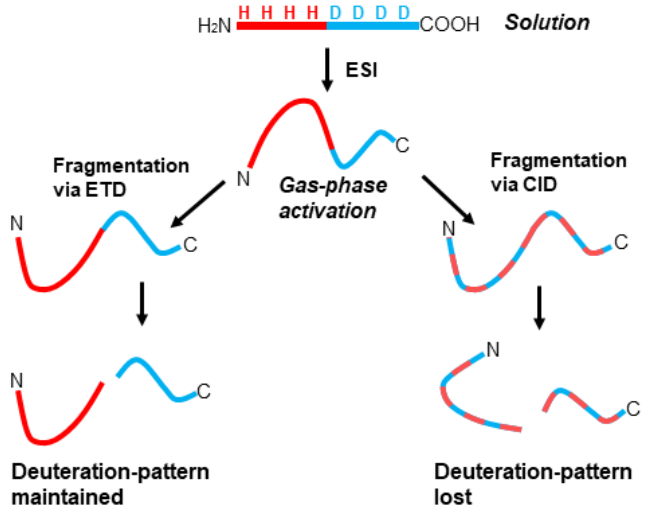

Figure 9: Illustration of scrambling in partly deuterated peptides.

Collisional activation in gas phase leads to migration of hydrogen (red) and deuterium (blue), which causes a loss of the original solution deuteration pattern. Figure modified from Rand *et al* [175].

2.4.1 The mechanism of collision-induced dissociation (CID)

In the generally accepted peptide-fragmentation mechanism of CID (Figure 10), cleavage between AA_n and AA_{n+1} is based on proton transfer onto the backbone carbonyl oxygen of AA_n. Subsequently, the carbonyl oxygen of AA_{n-1} attacks the partially electropositive carbon atom of the protonated carbonyl group (AA_n) [178,179]. The following proton transfer to the nitrogen atom leads to dissociation of the C-N bond [180,181].

The rate of intramolecular proton transfer is considered to be faster than the dissociation. Therefore, protons are statistically distributed over the backbone carbonyl groups, according to their basicities. The model predicts that the cleavage probability is related to the frequency of protonation. Hence, the gas phase basicity of the carbonyl oxygen of AA_n, determines cleavage efficiency [182]. First calculated by Zhang [183], gas phase basicity depends on the respective residue and its surrounding.

In addition, it is assumed that occupancy by a long-living hydrogen bond reduces the carbonyl group's ability to accommodate additional protons [184]. Therefore, CID efficiency is reduced in stable helices.

As this procedure is much faster than the time-consuming DHX experiments, I evaluated, whether the CID fragmentation propensity can be a measure for H-bond stability. This way, a small set of experiments could be used to determine the stability of an helix in the gas phase.

The proton transfer required for this type of fragmentation is facilitated by vibrational excitation [181]. In this work, vibrational excitation was predominantly caused by collision of the peptides to helium atoms in the trap cell of the mass spectrometer and mostly determined by the *trap collision energy*. Vibrational excitation and electrostatic repulsion cause a high mobility of the protons, which leads to fragmentation within 5-15 amino acids of basic residues and a maximum of fragmentation at a distance of 10 amino acids [185].
However, a major disadvantage of this method is the high amount of scrambling (see chapter 2.4) which is caused by the mobile protons [175] and which is unfavorable for DHX experiments.

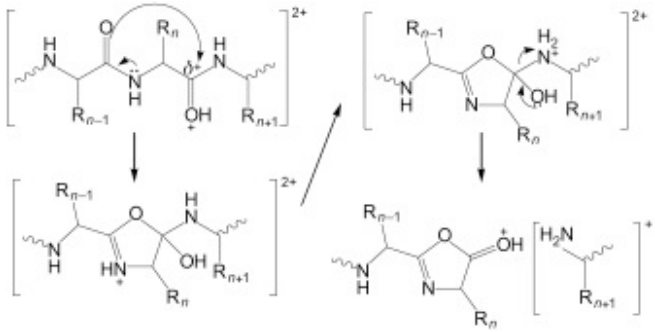

Figure 10: Mechanism of peptide fragmentation in CID.
Proton transfer to the carbonyl oxygen of AA_n leads to an attack of the carbonyl oxygen of AA_{n-1} which finally leads to dissociation between the N-C peptide bond between AA_n and AA_{n+1}. Figure adapted from Savitski *et al*. [184].

2.4.2 The mechanism of electron-transfer dissociation (ETD)

ETD is induced by the uptake of an electron by the peptide upon collision with a negatively charged radical anion reagent, which leads to loss of one charge (see equation (24)). Hence, the peptide must be at least 2+ charged to obtain data from ETD experiments.

$$[M + nH]^{n+} + A^{-} \rightarrow \left[[M + nH]^{(n-1)+}\right]^{*} + A \rightarrow fragments \qquad (24)$$

M: Molecule of interest
H: Proton
n: Charge state
A^-: Radical anion reagent
A: Uncharged anion reagent

There are different hypotheses concerning the detailed dissociation mechanism. The popular "Cornell" mechanism [186] is depicted in Figure 11. In this mechanism, the electron is received

by a positively charged side chain of a basic amino acid (lysine, arginine or histidine) that transfers its proton to a carbonyl oxygen. This results in dissociation between the amide C-terminal of that carbonyl and the subsequent C_α carbon. The position of the proton transferring side chain determines the charge of the fragments (see Figure 11).

Other hypotheses, like the "Utah-Washington" hypothesis, propose a direct electron uptake of the amide group, followed by anion neutralization by proton transfer, leading to cleavage of the N-C_α bond [187,188].

Fragmentation occurs in 1-100 ps [185,189], therefore intermolecular proton transfer, prior to cleavage, is not possible and scrambling is avoided. Consequently, ETD is a suitable method to investigate the deuterium content of fragments after DHX-experiments. However, to prevent scrambling before ETD fragmentation due to vibrational/collisional excitation, mild ionization parameters must be chosen [177].

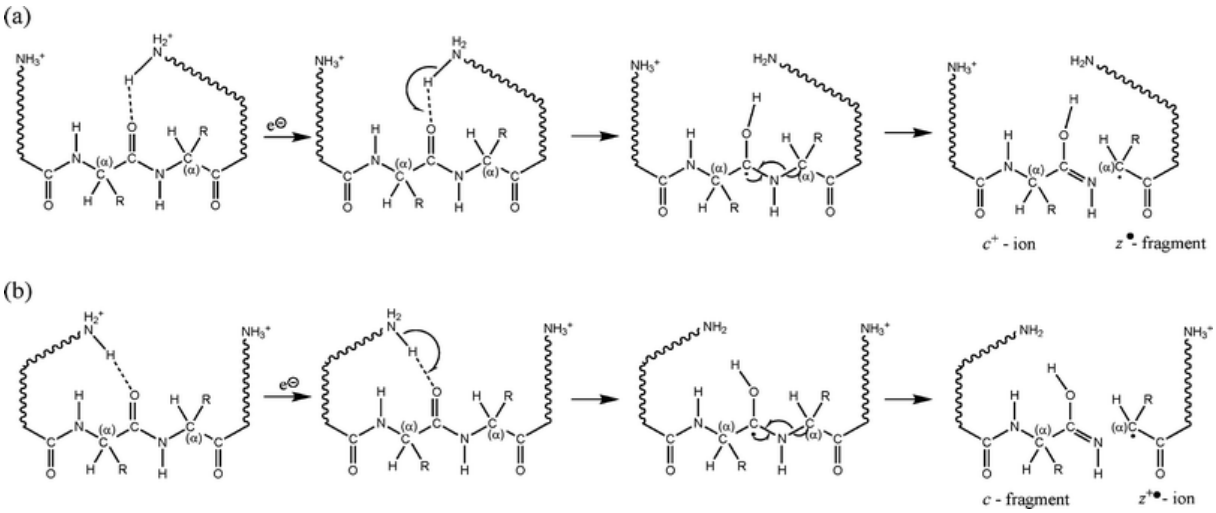

Figure 11: Cornell mechanism for N-Cα bond cleavage in ETD of peptides with charge.

Solvation from **A:** a C-terminal donor amine group; **B:** an N-terminal donor amine group. Figure adapted from Zhurov *et al.* [172]

ETD probably requires a direct interaction of the basic side chain with the carbonyl oxygen for proton transfer. Therefore, the range of fragmentation is limited to approximately 5 amino acids from the basic residue and shows the highest cleavage efficiency within 1-2 amino acids [185].

According to Zhang [190], the gas phase basicity of the proton accepting carbonyl oxygen is related to its frequency of protonation and therefore ETD efficiency. Similar to CID, it is plausible to assume that also in this case, long-living hydrogen bonds prevent the carbonyl oxygen from protonation and by this reduce fragmentation efficiency in stable helices. This model works only with the Cornell-mechanism, though.

3 Material and Methods

3.1 Chemicals

Table 2: Chemicals and peptides used in this work.

Chemical	Formula	Purity Grade and Manufacturer
Water (H^1)	H_2O	LC-MS Grade, Sigma Aldrich, St. Louis
Heavy Water (H^2)	D_2O	99,9 atom % D, Sigma Aldrich, St. Louis
2,2,2-Trifluoroethanol (TFE)	CF_3CH_2OH	LC-MS Grade, Sigma Aldrich, St. Louis
2,2,2-Trifluoroethan(ol-d) (d_1-TFE)	CF_3CH_2OD	99 atom % D, Sigma Aldrich, St. Louis
1,1,1,3,3,3-Hexafluoro-2-propan(ol-d)	$C_3H_1DF_6O$	98 atom % D, Sigma Aldrich, St. Louis
Ammonium acetate	$NH_4C_2H_3O_2$	For mass spectrometry, Sigma Aldrich, St. Louis
Ammonium acetate-d_7	$ND_4C_2D_3O_2$	98 atom % D, Sigma Aldrich, St. Louis
Formic acid	HCO_2H	For mass spectrometry, Sigma Aldrich, St. Louis
Formic acid-d_2	DCO_2D	98 atom % D, Sigma Aldrich, St. Louis
Acetic acid	CH_3CO_2H	LC-MS Grade, Sigma Aldrich, St. Louis
1,4-Dicyanobenzene	$C_6H_4(CN)_2$	98%, Sigma Aldrich, St. Louis
SUBSTANCE P (Acetate Salt Hydrate)		≥ 95%, Sigma Aldrich, St. Louis
Acetonitrile	C_2H_3N	LC-MS Grade, Carl Roth, Karlsruhe
Methanol	CH_3OH	LC-MS Grade, Panreac ApliChem, Darmstadt
Dodecylphosphocholine	$C_{17}H_{38}NO_4P$	LC-MS Grade, Sigma Aldrich, St. Louis
2,2′,2″,2‴-(Ethane-1,2-diyldinitrilo)tetraacetic acid	$C_{38}H_{44}N_6O_4$	LC-MS Grade, Sigma Aldrich, St. Louis

3.2 Instrumentation

- Synapt G2 HDMS Quadrupol-Time of Flight (Q- ToF) Electrospray Ionisation (ESI) Travelling Wave Ion mobility Separation (TWIMS) mass spectrometer [Waters, Wilmslow, United Kingdom]
- Harvard Apparatus 11plus Dual Syringe [Harvard Apparatus, Harvard, USA]
- Hamilton 100 µl Gastight Syringe [Hamilton, Bonaduz, Switzerland]
- WTW inoLab pH7110 [Xylem, White Plains, New York, USA]
- Amersham Biosciences Ultrospec 3100 *pro* [GE Healthcare, München, Germany]
- Hermle Z 233MK-2 [Hermle Labortechnik GmbH, Wehingen, Germany]
- Sonorex RK 52 H [Bandelin, Berlin, Germany]
- Univapo 100H [Vacuubrand GmbH, Germany]
- Eppendorf Mastercycler® PCR Cycler [Eppendorf AG, Hamburg, Germany]
- wtb Binder Incubator [Binder, Tuttlingen, Germany]
- J-710 Spektral-Polarimeters [Jasco, Easton, MD, USA]
- Delta 1-20KD [Christ, Osterode, Deutschland]

3.3 Peptides used in this work.

In this study, I used short model peptides which either consisted of residues 26-55 of C99 ($C99_{26-55}$) or residues 28-55 of C99 ($C99_{28-55}$) with an additional KK tag at the N-terminus (Table 3). The $C99_{26-55}$ peptides were used for global DHX experiments and CID experiments in the gas-phase. For ETD measurements, I had to use $C99_{28-55}$ based peptides in order to achieve proper fragmentation. Similar C99 TMD peptides were shown to be good substrates for γ-secretase [94,132]. Additionally, I used artificial model peptides, based on a poly-Leu sequence (Table 6 and Table 7). For a better overview, they are listed in the results (chapter 4).

For more native conditions, both terminal ends were blocked by acetylation (N-terminus) and amidation (C-terminus). Peptides were synthesized via Fmoc chemistry by PSL, Heidelberg, Germany and purified to > 90% purity as judged by mass spectrometry.

Table 3: C99-based peptides used in this work.

Alterations from $C99_{28-55}$ WT are marked in bold.

Peptide	Sequence
$C99_{26-55}$ WT	Ac-SNKGAIIGLMVGGVVIATVIVITLVMLKKK-NH_2
$C99_{26-55}$ G38L	Ac-SNKGAIIGLMVG**L**VVIATVIVITLVMLKKK-NH_2
$C99_{26-55}$ G38P	Ac-SNKGAIIGLMVG**P**VVIATVIVITLVMLKKK-NH_2
$C99_{26-55}$ I45T	Ac-SKKGAIIGLMVGGVVIATV**T**VITLVMLKKK-NH_2
$C99_{28-55}$ WT	Ac-KKKGAIIGLMVGGVVIATVIVITLVMLKKK-NH_2
C99 G38L	Ac-KKKGAIIGLMVG**L**VVIATVIVITLVMLKKK-NH_2
C99 G38P	Ac-KKKGAIIGLMVG**P**VVIATVIVITLVMLKKK-NH_2
C99 I47L/T48L	Ac-KKKGAIIGLMVGGVVIATVIV**LL**LVMLKKK-NH_2
C99 I47G/T48G	Ac-KKKGAIIGLMVGGVVIATVIV**GG**LVMLKKK-NH_2
C99 I45T	Ac-KKKGAIIGLMVGGVVIATV**T**VITLVMLKKK-NH_2

3.4 Solvation of peptides

All peptides were purchased from PSL (Heidelberg) and stored at -80°C. 2 mg of each peptide were solved in 2 ml of 2,2,2-trifluoroethanol (TFE) and sonicated for 15 min on ice (Sonorex RK 52 H). To remove undissolved peptides, the samples were centrifuged for 10 min at 13.000 rpm at 4°C (Hermle Z 233MK-2). The supernatant was transferred to a new Eppendorf tube. All dissolved peptides were stored at -20°C.

For experiments with dodecylphosphocholine (DPC) micelles, peptides were diluted into 2.5 mM DPC in 50% TFE/H_2O (v/v) to a final concentration of 12.5 µM, (peptide:detergent ratio of 1:200), sonicated for 15 min on ice, lyophilized (Christ Delta 1-20KD) and finally resuspended in 20 mM ammonium acetate (NH_4Ac) buffer + 1 mM Na-EDTA (2,2′,2″,2‴-(ethane-1,2-diyldinitrilo)tetraacetic acid), pH 6.8.

3.5 Deuteration of peptides

For complete deuteration, 300 µl of each peptide at a concentration of 300 µM were dried in the SpeedVac (Univapo 100H) at 50 mbar, for 30 min. The remaining peptides were redissolved in 300 µl 1,1,1,3,3,3-hexafluoro-2-propan(ol-d) (d_1-HFIP) and sonicated for 5 min. The samples were transferred to glass tubes and incubated for 7 d at 37°C (wtb Binder). Afterwards, the peptides were sonicated for 5 min and dried in the SpeedVac (50 mbar, 30 min). Subsequently, they were resolved in 80% d_1-TFE/D_2O (v/v) + 2mM deuterated ammonium acetate (ND_4Ac), sonicated for 5 min and diluted to a peptide concentration of 100 µM.

3.6 Mass-spectrometric experiments

All mass spectrometric experiments were run on a Synapt G2 Quadrupol-Time of Flight (Q-ToF) Electrospray Ionisation (ESI) mass spectrometer. A 100 µl Hamilton gastight syringe was used with a Harvard Apparatus 11plus, the flow rate was set to 5 µl/min. Spectra were acquired in a positive-ion mode with one scan for each second and 0.1 s interscan time. The Synapt G2 HDMS was run with the following parameters (Table 4):

Table 4: Settings of the Synapt G2 used in this work.

Parameter	CID	DHX	DHX-ETD
Scan time	1.0 sec	1.0 sec	1.0 sec
Data Type	Continuum	Continuum	Continuum
Source temperature	80°C	80°C	90°C
Cone gas flow	30 L/h	30 L/h	0 L/h
Desolvation gas flow	800 L/h	800 L/h	600 L/h
Make Up gas flow	-	-	30 mL/min
Capillary voltage	3 kV	3 kV	2.8 kV
Sampling cone voltage	20 V	30 V	20 V
Extraction cone voltage	4.0 V	4.0 V	2.0 V
Trap collision energy	2.0 – 40.0 V	4.0 V	4.0 V
Trap DC bias	2.0 V	2.0 V	2.0 V
Mass range	100 – 2000 m/z	100 – 2000 m/z	100 – 2000 m/z
TriWave Trap Wave Velocity	-	-	300 m/s
TriWave Trap Wave Height	-	-	1.50 V for intact peptide 0.2 V for ETD fragmentation
Trap gas flow	-	-	14.5 mL/min
Transfer gas flow	-	-	0.3 mL/min
Glow Discharge Current	-	-	60 µA
Glow Discharge: Sampling Cone Voltage	-	-	3.0 V
Glow Discharge: Extraction Cone Voltage	-	-	4.0 V
Acq Mode	Resolution	Resolution	Sensitivity

All measurements were repeated at least three times and the arithmetic mean was used for further evaluation.

Analysis of the spectra was performed with MassLynx 4.1, DriftScope 2.4 software (Waters, Milford, USA) and the GRAMS Suite (Thermo Fisher, Germering, Germany) including the MassMap plugin.

3.6.1 Global deuterium hydrogen exchange by MS/MS

Solutions of fully deuterated peptide (> 98% deuteration grade) were diluted 1:20 into 80% (v/v) TFE and 2 mM NH_4Ac, pH 5.0, and incubated at 20°C in a thermal cycler (Eppendorf, Germany). The final concentration was 5 µM. Incubation times were 0, 1, 2, 5, 10, 20, 30, 40, 50 min, and 1, 2, 3, 4, 6, 8, 12, 24, 48, 72 h. Exchange reactions were quenched by placing samples on ice and adding formic acid to a final concentration of 0.5% (v/v), resulting in a pH of 2.5. As a reference, non-deuterated peptides with a concentration of 3 µM in the corresponding proteinaceous solution were used. In both cases, triply charged peptide ions were observed.

Spectra of 1 min were combined for further analysis with MassLynx 4.1 software. The spectra were smoothed 5 times with 50 channels (Savitzky Golay) and centered over 80% area with 100 channels.

The amount of remaining deuterons was calculated with equation (25).

$$\text{Remaining Deuterons}: D(t) = z \times (m_D - m_H) - (\frac{1}{d_f} \times D_{\max}) \qquad (25)$$

D(t): Remaining Deuterons at time t

z: Charge of the peptides

m_D: m/z value of the deuterated peptides

m_H: m/z value of the not deuterated peptides (= non deuterated reference spectrum)

d_f: Dilution factor (in this case: 1:20, therefore 0.05)

D_{max}: Maximum number of exchangeable hydrogens

The correction with the dilution factor is necessary, to exclude the amount of deuterons that were present in the deuterated solution and statistically distributed on the peptides.

Regarding all amide bound exchange competent deuterons of the peptides, the observed DHX kinetics is a superposition of all individual exchange reactions. The exchange of each labile deuteron to hydrogen follows a reaction kinetics of first order with a characteristic rate constant. As all of these reactions happen at the same time, the exchange reaction of the peptide can be described by a sum of all rate constants.

In an analogous way, HDX in micelles was performed by diluting them 1:10 D_2O + 20 mM ND_4Ac, pD 5.9, set with AcOD. pD values were measured by using the pH-electrode and adding the correction constant of 0.4 [191]. However, now the applied equation (25) describes not the remaining, but the exchanged, deuterons.

3.6.2 Local deuterium hydrogen exchange by ETD-MS/MS

DHX reactions prior to ETD-fragmentation were performed analogously to the global DHX-kinetics (see 3.6.1). For electron transfer dissociation (ETD) 1,4-dicyanobenzene was used as reagent on 5+ charged peptides, preselected via MS/MS, as this charge state achieved the best ETD fragmentation results over the complete peptide sequence. In order to avoid scrambling of hydrogens, the settings were changed to:

Extraction cone voltage: 2.0 V, *sampling cone voltage*: 20 V, *T-wave velocity* 300 m/s, according to Rand, *et al.* [177,192].

The 1,4-dicyanobenzene solution was prepared daily. In the glow discharge mode of the Synapt G2, the *sampling cone voltage* was set to 1-4 V to achieve an ETD-reagent intensity of approximately 2-3e^6. To prevent the ETD-reagent from reacting with the peptide, a *trap wave height* of 1.5 V was applied, whereas a *wave height* of 0.2 V led to good fragmentation results. To evaluate the fragmentation efficiency, substance P was used as a standard. Hereby, the intensity of the three fragments 271.2, 1078.6, and 1103.6 m/z together, had to be at least 2% of the non-fragmented Substance P intensity. Substance P was dissolved in 1:1 Acetonitrile:H_2O (v/v) + 0,1% formic acid and diluted to a concentration of 2 µM.

ETD-measurements were performed after different incubation periods (from 1 min to 3 d) where exchange took place at pH 5.0. Shorter (0.1 min, 0.5 min) and longer (up to 62 d) incubation periods were simulated by lowering the pH to 4.0 or elevating the pH to 6.45, respectively, using matched periods. The differences to pH 5.0 were considered when calculating the corresponding rate constants. Noteworthy, base-catalyzed exchange is responsible for at least 95% of total deuteron exchange at ≥ pH 4.0. The resulting ETD c- and z-fragment spectra were evaluated using a semi-automated procedure (ETD FRAGMENT ANALYZER module of MassMap_2021-05-27 Software, MassMap GmbH & Co. KG, Freising, Germany).

The free energies ΔG required for H-bond opening were calculated from k_{exp} and k_{ch} (see equation (11) based on the Linderstrøm-Lang theory, assuming EX2 conditions and a predominantly folded state (see also 2.3) [193]:

$$\Delta G^0 = -R \cdot T \cdot \ln(K_{op}) = -R \cdot T \cdot \ln\left(\frac{k_{exp}}{k_{ch} - k_{exp}}\right) \qquad (11)$$

where k_{ch} represents the sequence specific chemical rate constants that were calculated by the online tool sphere: http://landing.foxchase.org/research/labs/roder/sphere/ (under the set conditions: D-to-H-exchange, reduced Cys, pH =5.0, T = 20.0°C).

Detailed theoretical background information is provided in 2.3.4. A detailed explanation of the evaluation with the MassMap Software, including error calculation, is described by the software developer in the publication of Yücel *et al.* [194].

It should be noted that the ΔG values obtained with this procedure are an upper estimate of the true values since (i) the molarity of water in 80% (v/v) TFE solvent is only 20% of the bulk molarity used for the determination of the reference chemical exchange rates k_{ch}, and (ii) the hydration of residues in the hydrophobic core of a TMD is possibly reduced relative to bulk. Both factors likely reduce the chemical exchange rate in our experiments. In addition, TFE might have an impact on the auto-ionization constant of water and the chemical exchange rate constants [91].

The extent of hydrogen scrambling could not be calculated with the ammonia loss method from Rand *et al.* [195] due to the blocked N-termini. However, previous experiments with similar peptides showed scrambling to be negligible under the applied conditions [196]. The absence of significant hydrogen scrambling is also indicated by the successful reconstruction of global exchange kinetics from the ETD data (Figure 16B).

The total workflow of the performed DHX experiments is shown in Figure 12.

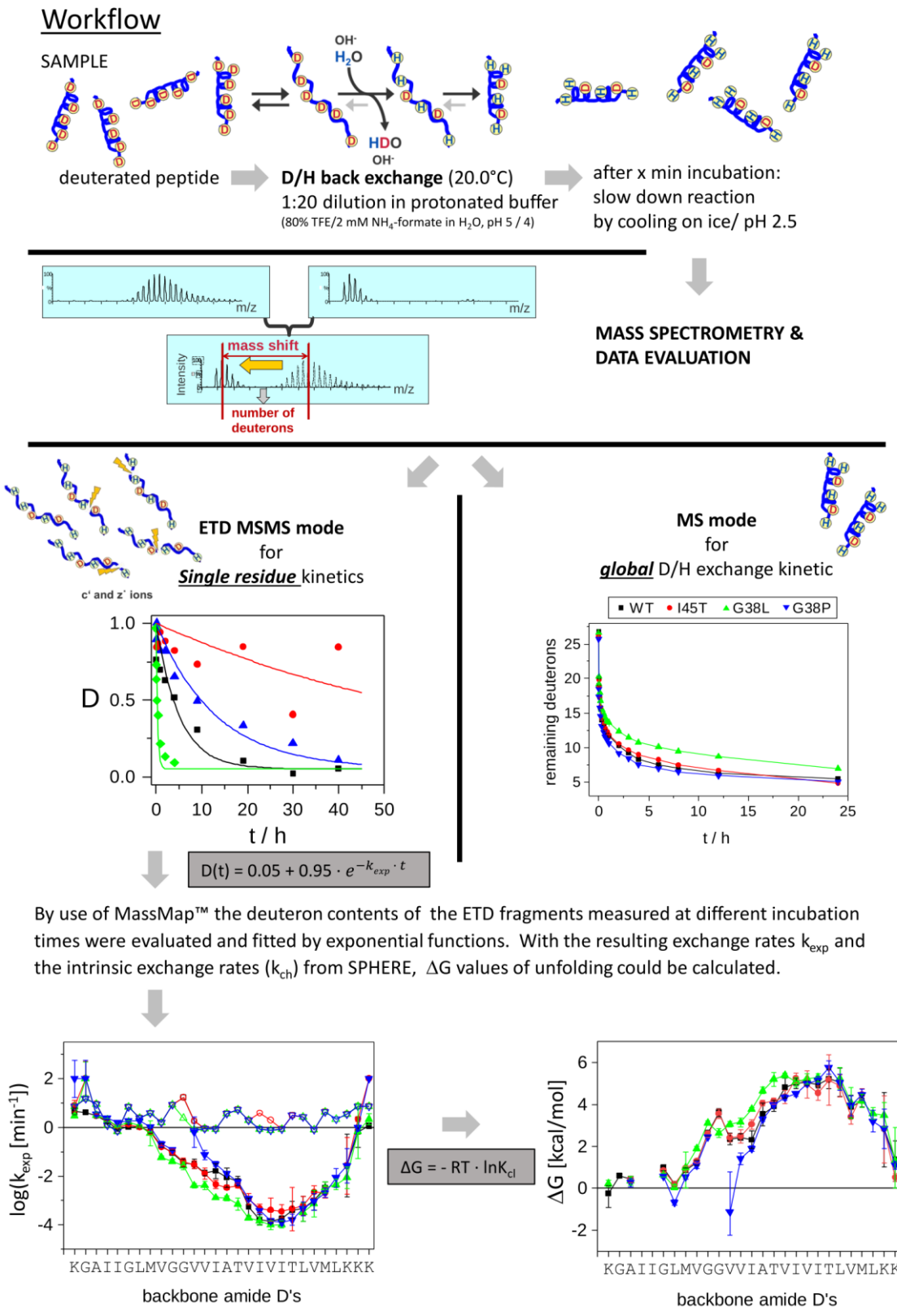

Figure 12: Scheme of the DHX-MS/MS workflow.

The workflow of the DHX experiments starts with the incubation of deuterated peptides in protonated solution, for distinct periods of times. Subsequently the peptides are either measured via MS for global exchange kinetics or fragmented via ETD and measured via MS/MS for single residue kinetics. The latter allows calculations of the individual exchange rates k_{exp} for each amide group and consequently the strength of the respective H-bonds. As examples C99WT (black), I45T (red), G38L (green) and G38P (blue) are shown.

3.6.3 Collision-induced dissociation (CID)

Experiments with increased trap collision energy were used to assess the patterns of CID fragmentation. For these experiments, peptides were diluted to a concentration of 3 µM in 80% TFE (v/v) + 2 mM NH_4Ac, pH 5.0 (set with AcOH).

Trap collision energies were increased to a value where the intensity of the intact precursor-peptide dropped to 50% (relative to the reference value at standard conditions), enabling sufficient fragmentation and comparable patterns for all peptides.

For analysis of the CID fragments, spectra of 1 min were combined, smoothed 2 times with 4 channels (Savitzky Golay method) and centered over 80% height with 3 channels. The respective fragment intensities were calculated in [%] of the corresponding precursor ion of the same measurement/spectrum. For calculation of fragment efficiency, respective b- and y-ions were summed up for each position (see 0).

3.7 Circular dichroism spectroscopy

For circular dichroism (CD) spectroscopy, peptides were dissolved in 80% 2,2,2-trifluoroethanol (TFE) with 2 mM NH_4-acetate, pH 5 at 50 µM. For each sample, 10 accumulated CD spectra from 190-260 nm were obtained using a Jasco J-710 CD spectrometer with a 0.2 data pitch, 1 sec response, bandwidth 2, 100 nm/min scan velocity, 100 mdeg/cm sensitivity, and a path length of 0.1 cm at 20°C. Mean molar residue ellipticities ($[\Theta]_{mr}$) were calculated based on the peptide concentrations which were estimated by UV spectroscopy using the absorbance of the peptide bond at 205 nm with an extinction coefficient e_{205} = 73.600 $mol^{-1}cm^{-1}$. This value was determined by calibration with the homologous peptide SNKWGAIIGLMVGGVVIATVIVITLVMLKKK whose concentration was determined using e_{280} = 5600 $mol^{-1}cm^{-1}$.

4 Results

The focus of this work was to investigate the helix flexibility of γ-secretase substrates and to connect these results with cleavage efficiencies and site specificities, known from previous works or obtained by collaborating partners.

Therefore, I analyzed a set of C99-TMD based peptides (Table 5), as well as a novel set of artificial peptides, based on poly-Leu and poly-Ala, holding sequence motifs of the C99 TMD (Table 6), via DHX-ETD. For both sets I assessed the effects of the G38G39 hinge motif on helix flexibility (C99 G38L and G38P, as well as pL-GG and pL-VGGV), as well as the influence of the ε-site (C99 I47L/T48L and I47G/T48G, as well as pL-cr). With the artificial poly-Leu peptides, I also tested the combined effects of the hinge motif and ε-site alterations (pL-VGGV-cr and pL-εGG) on helix flexibility. The peptides featuring the poly-Ala sequences were used to observe the effects of larger flexible regions at the N-terminus or the C-terminus, respectively. In addition to that, I investigated the I45T mutant, as this mutation shows a drastic drop of cleavage efficiency, compared to the WT, without a change of the preferential initial cleavage site. Details about the selection of the peptides are given in the respective chapters.

In a second set of experiments, I investigated the possibilities of CID fragmentation in the gas-phase to predict the helix flexibility of substrate TMDs. To validate the results from CID experiments, I introduced another set of smaller poly-Leu based peptides (Table 7) which were used to assess the long-range effects of the primary structure on dissociation efficiencies.

Table 5: C99-based peptides used for DHX-ETD experiments.

Alterations from $C99_{28-55}$ WT are marked in bold. $C99_{26-55}$ WT based peptides, as shown in Table 3 were used for CD-spectroscopy, CID experiments and global DHX-experiments.

Peptide	Sequence
$C99_{28-55}$ WT	Ac-KKKGAIIGLMVGGVVIATVIVITLVMLKKK-NH_2
C99 G38L	Ac-KKKGAIIGLMVG**L**VVIATVIVITLVMLKKK-NH_2
C99 G38P	Ac-KKKGAIIGLMVG**P**VVIATVIVITLVMLKKK-NH_2
C99 I47L/T48L	Ac-KKKGAIIGLMVGGVVIATVIV**LL**LVMLKKK-NH_2
C99 I47G/T48G	Ac-KKKGAIIGLMVGGVVIATVIV**GG**LVMLKKK-NH_2
C99 I45T	Ac-KKKGAIIGLMVGGVVIATV**T**VITLVMLKKK-NH_2

Table 6: pL24-based peptides used in this work.

Alterations from the poly-Leu sequence are marked in bold.

Peptide	Sequence
pL24	Ac-KKKLLLLLLLLLLLLLLLLLLLLLLKKK-NH_2
pL-GG	Ac-KKKLLLLLLLL**GG**LLLLLLLLLLLLLKKK-NH_2
pL-VGGV	Ac-KKKLLLLLLL**VGGV**LLLLLLLLLLLLLKKK-NH_2
pL-VGGV-cr	Ac-KKKLLLLLLL**VGGV**LLLL**VIVITLVM**LKKK-NH_2
pL-cr	Ac-KKKLLLLLLLLLLLLLL**VIVITLVM**LKKK-NH_2
pL-εGG	Ac-KKKLLLLLLL**VGGV**LLLLLLLL**GG**LLLKKK-NH_2
pA	Ac-KKKAAAAAAAAAAAAAAAAAAAAAAKKK-NH_2
pL-L15A9	Ac-KKKLLLLLLLLLLLLLLAAAAAAAAAKKK-NH_2
pL-A15L9	Ac-KKKAAAAAAAAAAAAAALLLLLLLLLKKK-NH_2

Table 7: LV5 control peptides.

Peptide	Sequence
LV5	KKKWLVLVLKKK
LV5-L3G	KKKWLVGVLKKK

4.1 Analysis of C99 TMD helicity via CD spectroscopy

As the main focus of this work was put on the helix flexibility of TMDs, it was crucial that the analyzed peptides show a high level of helicity in the applied experimental set-ups.

Thus, in a first set of experiments, the helicity of the $C99_{26\text{-}55}$ TMD peptide was analyzed via CD spectroscopy. For this, $C99_{26\text{-}55}$ WT, as well as the G38L and G39P mutants, were incorporated into micelles composed of DPC. DPC was identified as the optimal detergent, as it is an established micelle system for studies on transmembrane proteins [197–204], but also has a low critical micelle concentration (CMC) of 0.9 – 1.1 mM [197,205–211].

The latter is favorable in mass spectrometry experiments to avoid oversaturation of the instrument with detergent ions and to obtain high-quality spectra of the peptide.

The CD spectra revealed a high content of alpha-helical conformation in the micelles, as indicated by the minima at 208 nm and 218 nm (Figure 13 A). Although the spectra slightly differ in their amplitude, all three peptides feature a very similar shape of their CD spectra. Differences are likely to result from minimal differences in the respective concentrations of the peptides and does not indicate alterations in their helicity.

When the same peptides were dissolved in TFE/H_2O (80/20 v/v), ellipticity and shape of the spectra changed slightly, relative to DPC (Figure 13 B). The minima at 208 nm and at 220 nm also indicate a high degree of helicity. Again, a stabilizing/destabilizing effect of G38L and G38P, respectively, on the helical confirmation was not revealed in this solvent, as indicated by a highly similar shape of the spectra with only minimal differences in their respective amplitude.

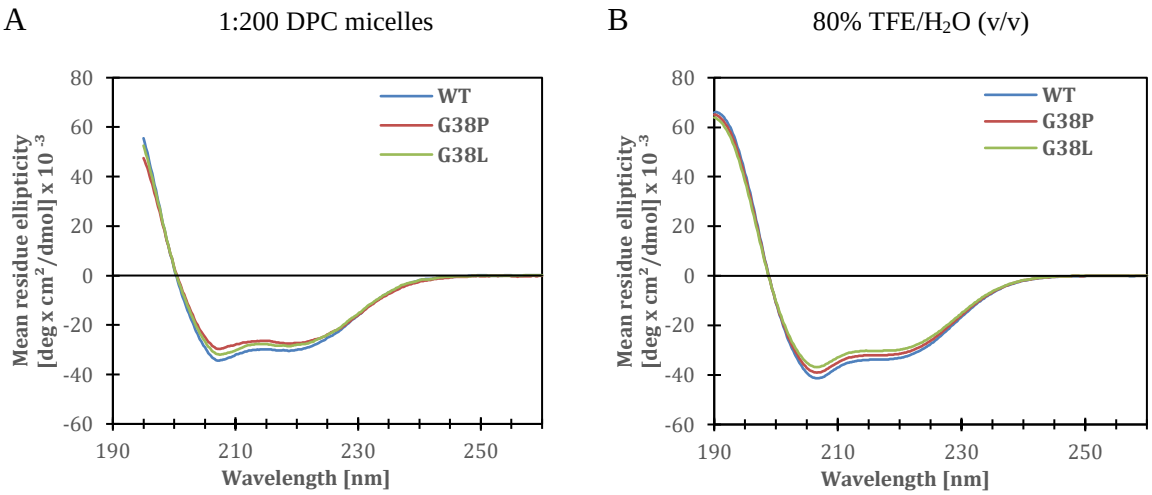

Figure 13: CD-Spectra of $C99_{26-55}$ based peptides.

$C99_{26-55}$ WT, G38L and G38P were reconstituted in A) DPC micelles (peptide to detergent ratio of 1:200) and dissolved in B) 80% TFE/H_2O (n = 3).

4.2 Overall deuterium-hydrogen exchange in micelles and in 80% TFE/H_2O

The conformational flexibility of an alpha-helix is mainly defined by the strength of its backbone H-bonds, established between the amide group at *n* and (in general) the carbonyl oxygen at *n-4*. The strength of these H-bonds, in turn, depends on side chain to side chain interactions, and, to a lesser extent, on side chain to main chain interactions [212].

In a first approach to investigate the strengths of these backbone H-bonds, global DHX experiments were performed. The strength of H-bonds correlates with the exchange rates of the respective amide groups. Also, exchange kinetics of each amide depend on the local concentration of the exchange catalyst (hydroxide ions) and are influenced by side chain chemistry [213,214].

To mimic the environment in the membrane, peptides were reconstituted in DPC micelles. As I was interested in the conformational flexibility of the substrate while it is incorporated in the γ-secretase, I also analyzed them in an 80% TFE/H_2O solution. The latter is expected to resemble the conditions in the interior of a transmembrane protein very well, due to its polarity and its accessibility to water [215–219].

Therefore, an exhaustively deuterated peptide ($C99_{26-55}$ WT, deuteration level > 98%) was incubated in 80% TFE/H_20 (pH 5.0, 20°C) and exchange reactions were stopped after specific incubation times, ranging from 1 min to 3 d. Subsequently, the exchange of backbone deuterium to hydrogen was determined via MS/MS. Thus, a wide distribution of incubation times made it possible to monitor backbone deuterium exchange over time. A concentration of 5 µm ensured a monomeric state in the solvent [93].

For analogous experiments in DPC micelles, the experiment had to be reversed and performed as hydrogen-deuterium-exchange (HDX), because high levels of deuteration could not be preserved during the several steps that are necessary to incorporate the peptide into the micelle. For this, the stock solution of DPC micelles with incorporated peptides was diluted 1:10 in D_2O + 20 mM ND_4Ac (pD 5.9, set with AcOD), to a final DPC concentration of 2.5 mM and a peptide concentration of 12.5 µl.

Figure 14 shows the respective global DHX and HDX kinetics of $C99_{26-55}$ WT in TFE/H_20 (A) and DPC micelles (B). In both the lipid bilayer and the solvent, global exchange kinetics are characterized by a rapid exchange in the first minutes which slows down gradually over time. This is due to the fact that some amide groups establish no or only labile hydrogen bonds (i.e., at the terminal regions where they lack H-bond partners) and therefore show fast exchange, while stronger H-bonds in the core region exchange significantly slower.

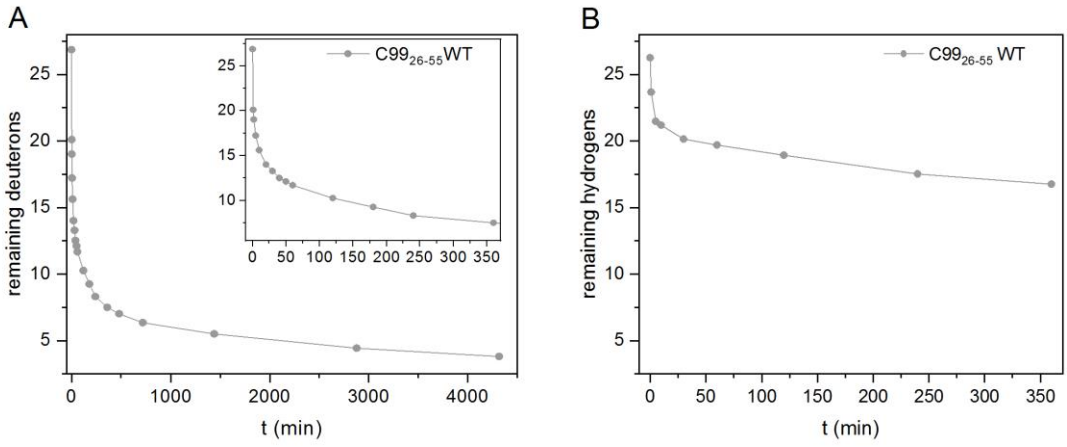

Figure 14: Overall exchange kinetics of $C99_{26-55}$ WT in 80% TFE/H_2O and DPC micelles.

A) Overall DHX kinetics of $C99_{26–55}$ WT measured with MS is shown. Complete deuteration was followed by back-exchange in TFE/H_2O (pH 5.0), T = 20°C. Exchange kinetics during 72 h were measured (n = 3, error bars showing SD are smaller than the size of the symbols). B) HDX kinetics of the same $C99_{26–55}$ WT in 1:200 DPC micelles. Note that HDX stalls after 360 min, even though a higher pH/pD (pD = 5.9) was applied, compared to the DHX experiments.

In 80% TFE/H_2O, nearly complete exchange was seen after 3 d. In contrast, experiments in DPC micelles suggested that the lipid bilayer shields the core region and thus prevents complete exchange of the peptide. After 6 h of incubation, exchange nearly stopped with 16.7 hydrogens remaining (vs. 7.5 remaining deuterons in the TFE experiment, after the same incubation period).

Also, isolating the peptide from the DPC detergent in the mass spectrometer required high cone voltages that would cause scrambling in later ETD experiments.

Consequently, further experiments were performed in the 80% TFE/H_2O environment, as this solution also reflects the conditions in the γ-secretase in a better way.

4.3 Calculation of residue-specific exchange rate constants

To map the conformational flexibility of the $C99_{26-55}$ WT TMD, it was necessary to advance from overall backbone amide DHX kinetics to individual exchange rate constants (k_{exp}) of each residue. This way, it is possible to determine the stability of backbone H-bonds at a residue-specific level. This enables detection of distinctive features or patterns in the conformational flexibility of TMD helices that might define cleavage probability and efficiency.

To determine k_{exp} values, DHX in solution was stopped after different periods of time (0.1 min to 62 d at pH 5.0) and the peptides were subsequently fragmented in the gas-phase via ETD. In contrast to CID, the ETD method preserves the deuteration pattern of the peptide. Resulting c- and z-fragment ions were then used to determine the deuteron content of each amide group at the different timepoints.

The deuteration level $D(R_n)$ of an amide group of residue R_n could be calculated by subtracting the amount of deuterons on fragment F_{n-1} from F_n (Figure 15) and residue-specific DHX kinetics were obtained (Figure S1).

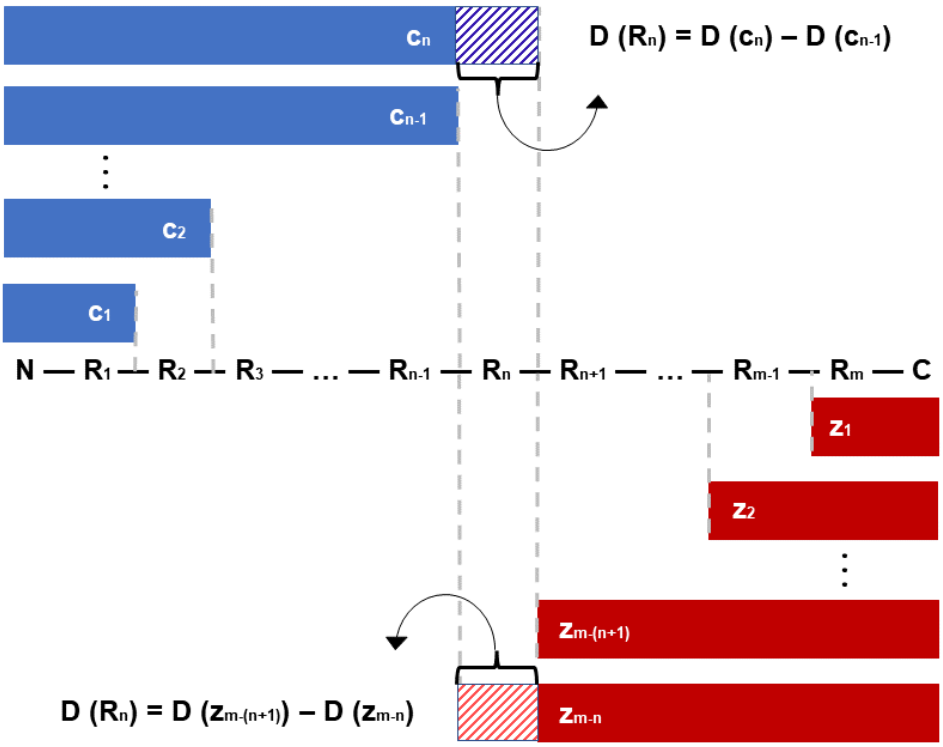

Figure 15: Obtaining site-specific D contents after ETD fragmentation.

Calculation of the deuterium amount for each residue after ETD. c-Fragments starting from the N-terminus are depicted in blue, z-fragments starting from the C-terminus in red. Both fragment types can be used to calculate the deuterium amount of residue R_n. To do this, the difference in the number of deuterons on the fragment containing the amide group of R_n and the fragment that contains one residue less, must be calculated (represented with the hatched areas). So, the deuterium amount of R_n, $D(R_n)$, is calculated by subtracting $D(c_{n-1})$ from $D(c_n)$. For z-ions, which are counted from the C-terminus, the calculation is $D(R_n) = D(z_{m-(n+1)}) - D(z_{m-n})$ with m being the total length of the peptide.

The decay of the deuteron content over time allowed calculation of the respective residue specific k_{exp} by equation (21) which was derived in chapter 2.3.4:

$$D(t) = 0.05 + 0.95 \cdot e^{-k_{exp} \cdot t} \qquad (21)$$

Thus, applying an exponential fit on the residue-specific DHX kinetics yields the respective k_{exp} values (Figure S1).

As the fragmentation via ETD provided only poor sequence coverage for the original $C99_{26\text{-}55}$ WT peptide, it was necessary to exchange S26 and N27 to lysine (termed $C99_{28\text{-}55}$ WT). To exclude major consequences of this sequence alteration on TMD dynamics, I compared the overall DHX kinetics of both peptides (Figure 16 A). Excellent agreement was

found for intermediate and long incubation times while some differences were observed for rapidly exchanging deuterons. Later evaluations showed that these rapidly exchanging deuterons belong to the frayed terminal regions. Therefore, no alterations in the core region of the peptides are expected as a result from the S26K and N27K mutations.

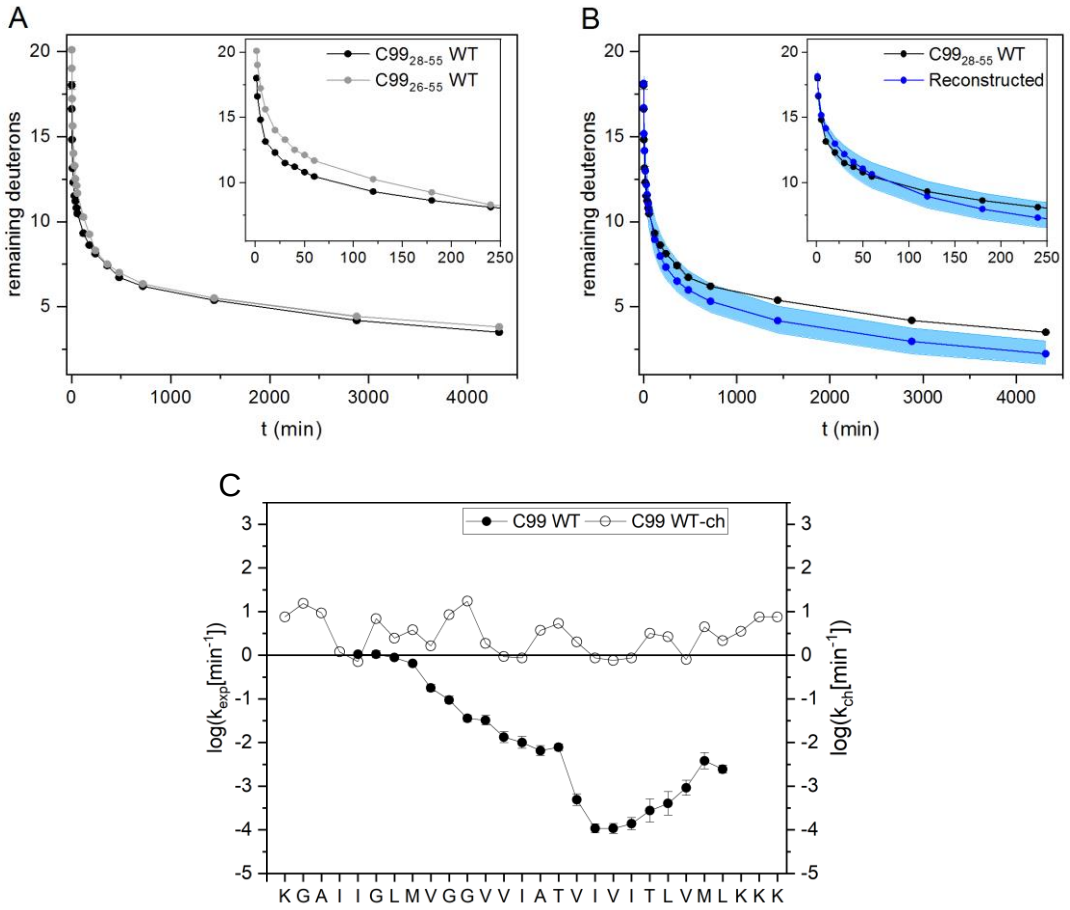

Figure 16: Single residue specific exchange rates of C99$_{28-55}$ WT.

A) Overall DHX kinetics of C99$_{28–55}$ WT compared to C99$_{26-55}$ WT. Complete deuteration was followed by back-exchange in 80% TFE/H_2O (pH 5.0), T = 20°C. Exchange kinetics were measured for 72 h (n = 3, error bars showing SE are smaller than the size of the symbols), the inset depicts the first 250 min. Both peptides show a high concordance with a slightly faster exchange of C99$_{26-55}$ WT in the first minutes. B) Reconstructed global exchange of C99$_{28-55}$ WT, back-calculated from the single residue specific k_{exp} values and compared to the measured global exchange kinetics. 95% confidence interval of k_{exp} values is shown in light blue. The back-calculation shows good agreement with the measured global exchange. Only the slowest deuterons in the core region exchange slower than calculated. C) Exchange rate constants k_{exp} [min^{-1}] of individual amide deuterons. The values of k_{exp} (filled symbols, mean values ± SE) were derived from exponential fits of the residue-specific DHX kinetics as obtained from ETD experiments (Figure S1). Residues without values are not covered by sufficient data points. Empty symbols represent the respective chemical exchange rate constant k_{ch} [min^{-1}] that reflects the DHX kinetics in an unfolded state.

The individual k_{exp} values, derived from the single reside DHX kinetics, are depicted against the $C99_{28-55}$ WT sequence in Figure 16 C.

The lower the calculated k_{exp} values are, the slower the exchange of the respective H-bond is. Regarding $C99_{28-55}$ WT, the determined k_{exp} values are below the respective chemical amide exchange rate constants k_{ch} between G33 and L52. On one hand, this indicates participation of these residues in the secondary structure, hence helix formation. On the other hand, this shows unfolding of the termini due to a lack of H-bond partners. In addition to that, these terminal residues exchange so fast that the deuteration level even at t = 0 was already too low for a proper fit and therefore no reliable k_{exp} values can be calculated.

The k_{exp} rate profile also reveals a rapid exchange in the N-terminal region (lg k_{exp} [min^{-1}] values between 0 and -1.5), which gradually decreases towards the very slow exchanging C-terminal region that contains the ε-cleavage sites (lg k_{exp} [min^{-1}] of about -4).

In contrast to previous NMR measurements in micelles [95] and molecular dynamics (MD) simulations, [92,93,103,220] no locally increased exchange rate constants around the G37G38 motif could be observed. In MD simulations, the very flexible N-terminal region upstream of the putative hinge was calculated to be more stable. Nevertheless, these measurements are in good agreement with previous studies that also investigated the C99 TMD via DHX and ETD [91–93].

To verify the determined k_{exp} rate constants, they were used to reconstruct global DHX kinetics. The reconstructed kinetics show high concordance with the directly measured global kinetics, except for the very slowly exchanging deuterons (Figure 16 B). For the last remaining deuterons, the reconstructed exchange is a little too fast, meaning that the calculated k_{exp} values slightly underestimate stability in the very rigid C-terminal region.

4.4 Estimation of H-bond strength ΔG

As explained earlier, experimentally determined k_{exp} rates are based on the stability of the respective amide H-bonds, as well as the local concentration of the exchange catalyst and the chemical exchange rate k_{ch}. The latter, in turn, depends on the pH and side chain chemistry. As side chain chemistry is a matter of the primary sequence, this circumstance makes it difficult to compare peptides with different sequences via k_{exp} rate constants.

By converting k_{exp} rates into the free energy change of H-bond formation (ΔG), these effects of the primary structure are taken into account. The detailed calculation of ΔG is described in section 2.3.3. According to the theory of Linderstrøm-Lang, ΔG is a direct measure of H-bond stability [193]. Thus, ΔG is ideal to compare backbone flexibilities of different peptides, independent from pH, temperature, or primary structure. Thus, the comparison of different

peptides in the following chapters will focus on ΔG values and the k_{exp} profiles will be shown as reference.

For $C99_{28-55}$ WT, the profile of ΔG values confirms the high flexibility of the N-terminal region (ΔG < 2 kcal/mol) followed by a rigid C-terminal region (ΔG ~ 5 kcal/mol) (Figure 17). In contrast to the k_{exp} rate constants, ΔG values now also reveal a local drop in ΔG at V39, V40 and I41, consistent with the G38G39 hinge, previously found by NMR measurements [95,96], MD simulations [93,97–101] and DHX experiments [91]. This local drop becomes apparent after considering the different k_{ch} rates of each residue.

It must be noted that the reported ΔG values represent the upper estimates of true values, as the reference k_{ch} values used for the calculation of ΔG derived from unfolded peptides in H_2O [194], as detailed in chapter 2.3.3.

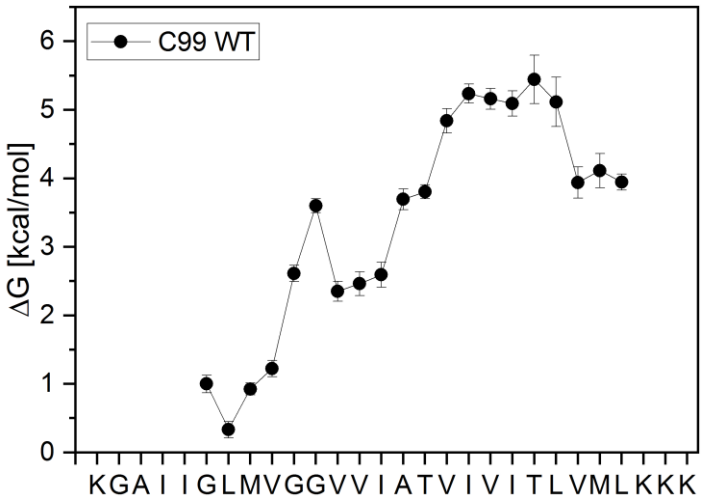

Figure 17: Free energy change ΔG of intrahelical amide H-bond formation.

Strength (ΔG) of intrahelical amide H-bonds based on calculated exchange rate constants (k_{exp}). Calculation of ΔG was not possible for residues where k_{exp} was not given or exceeded by k_{ch}. Error bars correspond to standard confidence intervals calculated from the standard errors of k_{exp}.

4.5 Effects of point mutations on TMD backbone flexibility of $C99_{28-55}$ WT

To gain deeper insights into how the backbone flexibility of substrate TMDs affects cleavage in γ-secretase, I investigated mutations of C99 that were known or assumed to increase or decrease cleavage efficiency. This way, differences in the ΔG profile were connected to cleavage data.

These point mutations were located at regions of high relevance:

1. Recent studies showed that most FAD associated mutations are in the vicinity of the cleavage region [221] but do not destabilize the ε-site itself. Significant effects are rather observed for the H-bonds upstream of the ε-cleavage sites [215] and in case of the 'Austrian' mutation T43I even around the G37G38 hinge [91]. It was proposed that the G37G38 hinge plays a crucial role in the coordination of large-scale movements required to move the cleavage region towards the active center of the γ-secretase [27,102,221]. Hence, the first focus was put on the putative G37G38 hinge. In detail, the aim was to alter hinge dynamics with a helix-promoting G38L mutation (stabilization) and the helix-perturbing G38P (destabilization). The expectation was that the stabilized helix causes a reduction in cleavage efficiency, while a destabilized helix shows the opposite effect.

2. As proteolysis requires unfolding of the initial cleavage site, the ε-site is a promising target for cleavage studies. In previous works, Fernandez *et al.* [139] exchanged I47 and T48 of C99 WT to presumably helix-promoting leucine or helix-destabilizing glycine, respectively. In their study, the I47L/T48L mutation caused a 4-fold decrease of cleavage efficiency, while the introduction of the glycines at the same position increased efficiency by the factor of 3.5 [139].

These changes in cleavage efficiency had been explained with supposed flexibility changes at the cleavage region. I reasoned that inspecting the actual ΔG profiles of these mutants would test this assumption.

3. From the many FAD mutations, the I45T mutation is clearly outstanding. The cleavage efficiency is strongly reduced and one of the lowest among all FAD mutations [112,113]. But in contrast to most FAD mutations, the preferential initial cleavage site is not shifted to ε48.[111] As a shifted cleavage site might already be one reason for reduced cleavage efficiency, this mutation could offer an exclusive insight into the role of helix flexibility in cleavage efficiency.

4.5.1 How mutations of the G38G39 hinge motif alter helix flexibility

Global DHX showed slower exchange kinetics for G38L, thus a higher stability of backbone H-bonds, as well as faster exchange of G38P (Figure 18A). As the proline residue of G38P does not contribute an amide deuterium which hinders comparability to other peptides, the number of remaining deuterons was normalized to the maximal amount of deuterons D_{max} of each peptide (D_{max} = 45 for $C99_{26-55}$ WT and $C99_{26-55}$ G38L; D_{max} = 44 for $C99_{26-55}$ G38P).

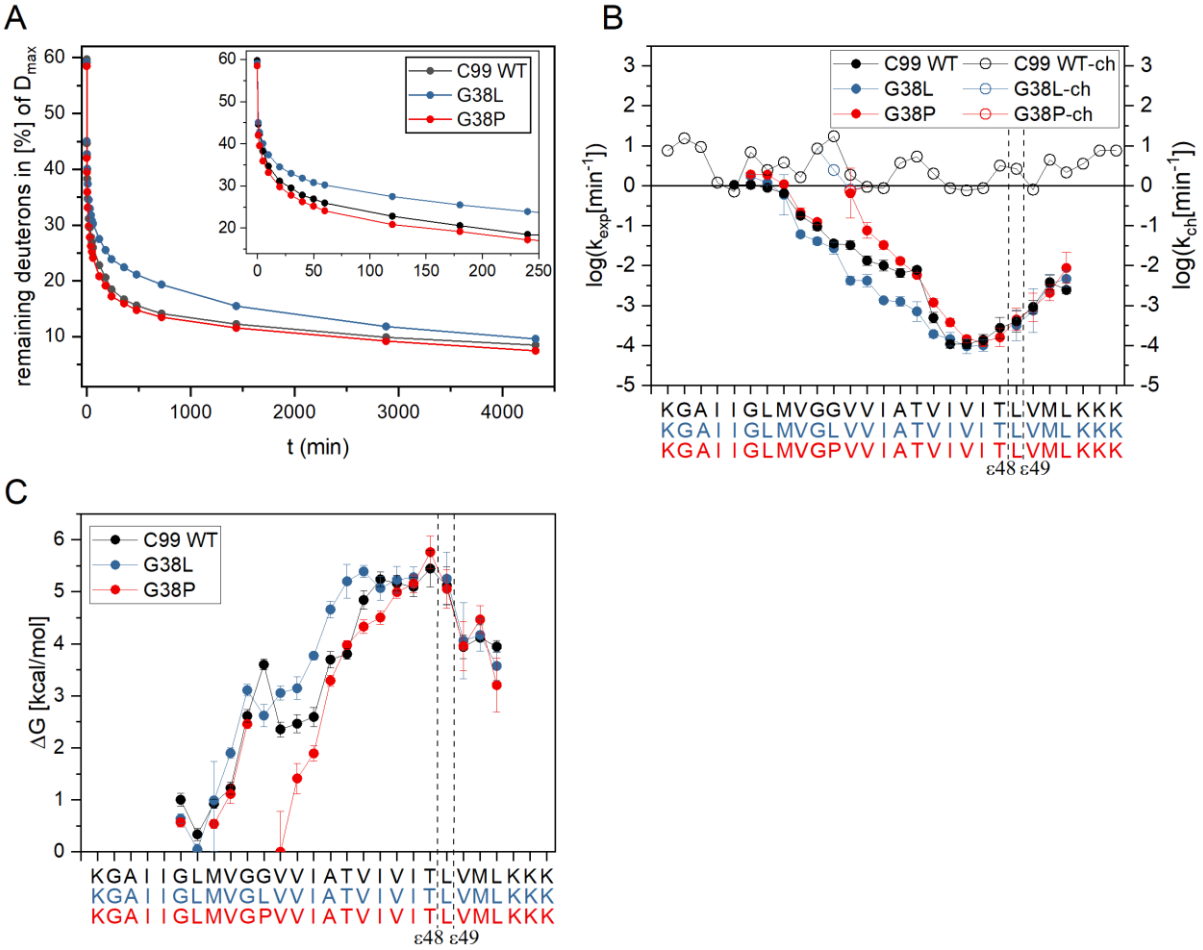

Figure 18: Deuterium-hydrogen exchange kinetics and H-bond stabilities of G38X mutants, determined by DHX-ETD.

A) Overall DHX kinetics of G38L and G38P mutants compared to C99 WT (80% TFE/H_2O, pH 5.0, T = 20°C). Exchange kinetics were measured for 72 h (n ≥ 3, error bars showing SE are smaller than the size of the symbols), the inset depicts the first 250 min. The number of remaining deuterons was normalized to the maximal amount of deuterons D_{max} of each peptide (D_{max} = 45 for $C99_{26-55}$ WT and $C99_{26-55}$ G38L; D_{max} = 44 for $C99_{26-55}$ G38P). B) DHX rate constants k_{exp} [min^{-1}] of individual amide deuterons (filled symbols, n ≥ 3, mean values ± SE), derived from exponential fits of the residue-specific DHX kinetics (Figure S1). Residues without values are not sufficiently covered by data points. Empty symbols represent the respective chemical exchange rate constant k_{ch} [min^{-1}] that reflect the DHX kinetics in an unfolded state. C) Strength (ΔG) of intrahelical amide H-bonds based on individual k_{exp} values. Calculation of ΔG was not possible for residues where k_{exp} was not given or exceeded by k_{ch}. Error bars correspond to standard confidence intervals calculated from the standard errors of k_{exp}.

Analyzing the ΔG values revealed that both mutations alter the H-bond strengths downstream of the mutation site (Figure 18C). While the G38L mutation causes increased H-bond strengths between V39 and V44 (up to 1.2 kcal/mol), G38P destabilizes H-bonds from V39 to I41. The effect of the G38P mutation did not extend as far as that of the G38L mutation, however, the impact on local H-bonds was higher (up to 2.5 kcal/mol). Similar to the WT, both mutations feature a very rigid C-terminal region and show no effect on H-bond strengths around the ε-sites.

This indicates that the G38X mutations indeed cause the expected stabilization/destabilization around the hinge motif, respectively, but do not affect H-bond stabilities at the ε-site.

Due to the side chain conformation of proline and the mechanism of ETD, it is not possible to achieve fragmentation between G37 and P38 and therefore no kinetic data could be determined for P38.

4.5.2 How mutations of I47T48 at the ε-site alter helix flexibility

Analyzing the individual H-bond strengths of C99 I47G/T48G and C99 I47L/T48L revealed a surprise (Figure 19). In contrast to the assumptions of Fernandez *et al.* [139], both peptides show decreased H-bond stabilities (up to 1.2 kcal/mol), relative to WT, at sites between the mutation site and V44, one turn upstream. The I47G/T48G mutation also has a strong destabilizing effect at the mutation site and downstream, where H-bond strengths are reduced by up to 2.6 kcal/mol. In contrast, the I47L/T48L mutation shows H-bond stabilities similar to the WT. While the sequence between V39 and T43 is identical to $C99_{28\text{-}55}$WT, both peptides also show some reduction of H-bond strength at the G38G39 motif. This is in agreement with previous studies with the T43I FAD mutation which affects H-bond strengths at G38G39 [91,215].

Previous studies outlined how threonine residues in the C99 TMD, namely T43 and T48, rigidify the helix by forming H-bonds between their side chains and the peptide's main chain [91,103]. Thus, removal of a T48 - main chain H-bond explains the surprising decrease of ΔG values for the I47L/T48L mutation, which was expected to promote helicity and thus, rigidity. This is a clear indication that the differences in cleavage efficiency observed by Fernandez *et al.* [139] are not correlated to backbone flexibility at the ε-site.

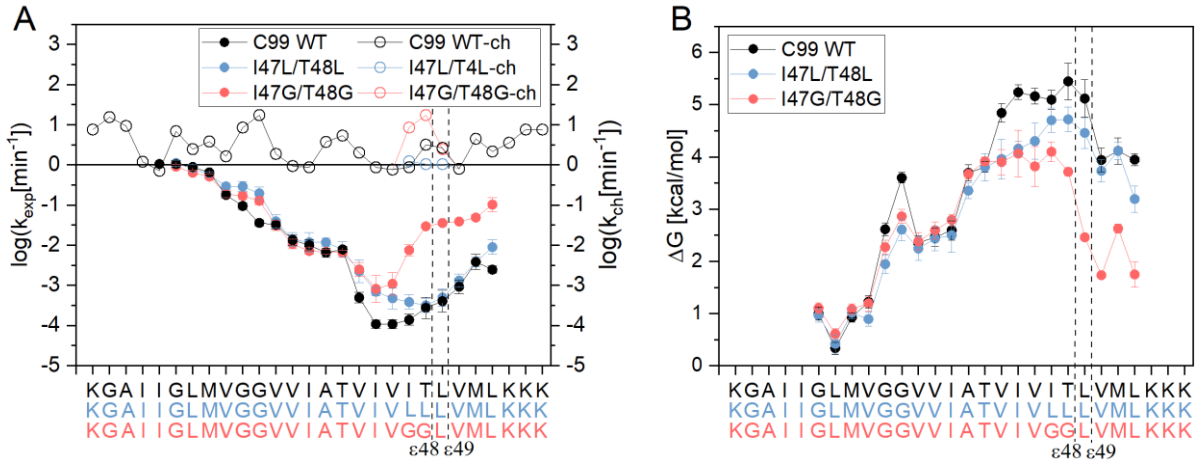

Figure 19: Deuterium-hydrogen exchange kinetics and H-bond stabilities of ε-site mutants, determined by DHX-ETD.

A) DHX rate constants k_{exp} [min^{-1}] of individual amide deuterons (filled symbols, $n \geq 3$, mean values ± SE), derived from exponential fits of the residue-specific DHX kinetics (Figure S2). Residues without values are not sufficiently covered by data points. Empty symbols represent the respective chemical exchange rate constant k_{ch} [min^{-1}] that reflects the DHX kinetics in an unfolded state. B) Strength (ΔG) of intrahelical amide H-bonds based on individual k_{exp} values. Calculation of ΔG was not possible for residues where k_{exp} was not given or exceeded by k_{ch}. Error bars correspond to standard confidence intervals calculated from the standard errors of k_{exp}.

4.5.3 Effects of the I45T FAD mutation on helix flexibility

Comparison of overall DHX kinetics from $C99_{26-55}$ WT and the $C99_{26-55}$ I45T mutant shows very similar exchange kinetics for both peptides. Deuterons of I45T exchanging with intermediate velocity exhibit a difference of ~1 D after 6 h. Beyond this timepoint, exchange of I45T was significantly faster than of the WT, which resulted in a crossing of the exchange curves after ~16 h (Figure 20 A).

Detailed analysis of the individual k_{exp} rates explains this observation with lower rates of I45T for the residues I41-T43 (intermediate velocity) and higher rates at the mutation site T45 (slowly exchanging).

However, considering the k_{ch} rates reveals that the partly faster exchange of T45 is only due to chemical effects of the altered primary structure. Thus, the only difference in H-bond strengths is from I41 to T43, where the I45T mutant shows increased ΔG values of about ~0.4 kcal/mol. This position is exactly one turn upstream of the mutation site.

As already described, previous studies pointed out that side chain - main chain interactions of Thr residues can rigidify the C99 TMD helix.[91,103] This leads to the assumption that the introduced threonine of I45T stabilizes the helix one turn upstream. Indeed, recent MD simulations revealed that the I45T mutant forms an additional H-bond between the side chain of T45 and the backbone carbonyl oxygen of I41 [222].

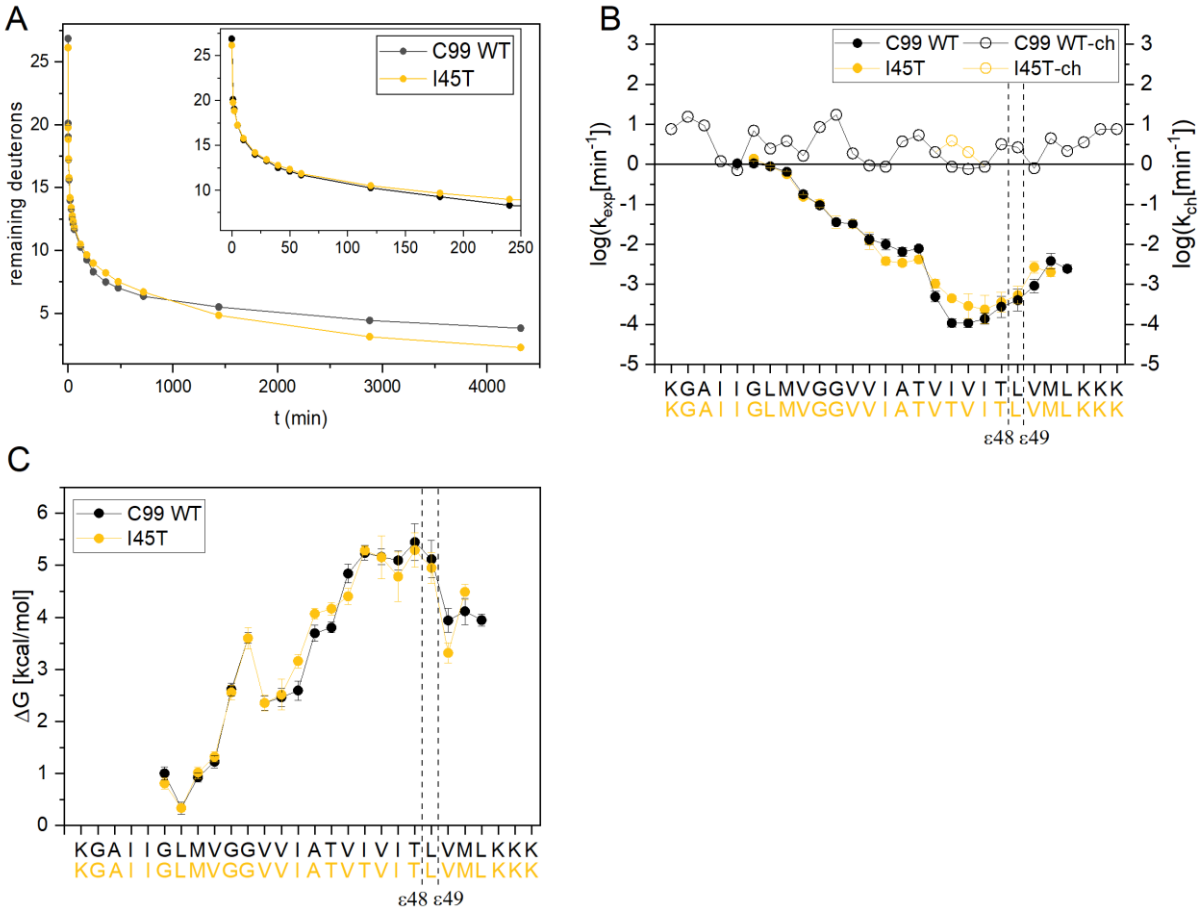

Figure 20: Deuterium-hydrogen exchange kinetics and H-bond stabilities of FAD mutant I45T, determined by DHX-ETD.

A) Overall DHX kinetics of FAD mutant I45T compared to C99 WT (80% TFE/H_2O, pH 5.0, T = 20°C). Exchange kinetics were measured for 72 h ($n \geq 3$, error bars showing SE are smaller than the size of the symbols), the inset depicts the first 250 min. B) DHX rate constants k_{exp} [min^{-1}] of individual amide deuterons (filled symbols, $n \geq 3$, mean values ± SE), derived from exponential fits of the residue-specific DHX kinetics (Figure S1). Residues without values are not sufficiently covered by data points. Empty symbols represent the respective chemical exchange rate constant k_{ch} [min^{-1}] that reflects the DHX kinetics in an unfolded state. C) Strength (ΔG) of intrahelical amide H-bonds based on individual k_{exp} values. Calculation of ΔG was not possible for residues where k_{exp} was not given or exceeded by k_{ch}. Error bars correspond to standard confidence intervals calculated from the standard errors of k_{exp}.

4.6 Backbone flexibility of artificial model peptides

To address the connection between substrate TMD flexibility and cleavage efficiency by γ-secretase in a systematic way and with maximally reduced complexity, a set of artificial model-substrates was introduced (Table 6).

These model-substrates are based on a very rigid, non-cleavable poly-Leu TMD of 24 residues, flanked by three lysine residues at each terminus, respectively. The lysine residues are necessary for proper solvation of the peptides and successful fragmentation via ETD. A similar model-peptide with a poly-Leu TMD of 16 residues was already established to systematically study the relationship of fusogenicity and helix stability [223]. This peptide's TMD proved to be very rigid and slowly exchanging in DHX experiments [224]. Later MD simulations showed that the high rigidity arises from strong side chain to side chain van der Waals (VDW) interactions between consecutive turns of the helix [212].

In a first set of experiments, motifs of the native C99 WT sequence were stepwisely introduced into the poly-Leu TMD, to analyze their effects on helix flexibility. For these experiments, I focused on the G37G38 hinge motif and the sequence around the ε-site.

In a second approach, I swapped the entire N- or C-terminal regions, respectively, of the pL24 peptide to a poly-Ala sequence in order to investigate the impact of alanine on helix flexibility. Although both Ala and Leu are known to be very helix-promoting [225,226], I reasoned that the smaller side chain of Ala allows fewer side chain to side chain VDW interactions and thus increases helix flexibility.

To connect backbone flexibility to cleavage efficiency in γ-secretase, two cooperating research groups performed experimental cleavage assays *in vitro* and *in cellulo* with C99 constructs holding the same TMDs. The obtained cleavage results and insights from them are later discussed (see discussion 5.3).

4.6.1 Consequences of local reconstitutions of C99 WT sequence on the TMD flexibility

4.6.1.1 Effects of introducing the hinge motif

Previous studies had suggested an impact of the G37G38 hinge motif on C99 TMD flexibility and the positioning of the substrate in the γ-secretase [91,215], with consequences for cleavage efficiency. This hypothesis was confirmed by experiments with the G38X mutations (chapter 4.5.1), where stabilizing and destabilizing mutations of the hinge motif caused severe changes to the TMD flexibility, as well as highly reduced cleavage efficiency, as later discussed in chapter 5.2.1. Also, previous studies pointed out the importance of the two flanking valine residues (V36 and V39) for the flexibility of the hinge [103]. Hence, I introduced the GG, as well

as the VGGV motif, into the poly-Leu sequence in order to test the consequences, resulting in the pL-GG and pL-VGGV peptides (Table 6).

Unfortunately, the maternal pL24 peptide, which all mutants are based on, could not be analyzed via ETD. The isotope patterns of ETD fragments showed a bimodal shape after long incubation periods (> 10.000 min), which made it impossible to evaluate these fragments and to calculate k_{exp} and ΔG values. Based on the first 17 N-terminal residues of L15A9 (see chapter 4.6.2), I expect a very rigid TMD with H-bond strengths of about 6 kcal/mol for the central region of the pL24 peptide.
A bimodal isotope pattern usually indicates EX1 kinetics, which means correlated exchange of residues and therefore occurs, when k_{ch} vastly exceeds k_{cl}. This is typical for a protein or a region that is unstable and unfolded most of the time. Therefore, bimodal shapes should occur immediately at very short incubation periods. This is clearly not the case for the very rigid pL24 peptide. So, it is plausible to assume that the pL24 exchanges under EX2 kinetics and there might be experimental artefacts causing the observed bimodal isotope pattern. The experimental set-up was tested in regard of pH (from pH 3.0 to pH 7.6), peptide concentration (from 0.5 µM to 25 µM), and time in the DHX reaction chamber (from 1 min to 50 d). However, none of these parameters had an effect on the bimodal isotope patterns.

Figure 21 shows the exchange rate constants $k_{exp,}$ (A) and the according free H-bond energies ΔG (B) of pL-GG and pL-VGGV in comparison to the $C99_{28-55}$ WT. As the sequences of $C99_{28-55}$ WT and the poly-Leu peptides differ for the most part, they also feature different intrinsic exchange constants k_{ch}. Consequently, the comparison is focused on the calculated ΔG values, which takes the different k_{ch} values into account.
Also, when describing the residues or positions of various pL-based peptides, the nomenclature of the C99 WT will be used for simplicity.

Unsurprisingly, pL-GG and pL-VGGV show a very similar pattern. Compared to $C99_{28-55}$ WT, both pL-GG and pL-VGGV are significantly more stable within their N-terminal part (4.6 and 4.3 kcal/mol, respectively) as well as in the core region and the C-terminal half, where H-bond strengths exceed the ones of $C99_{28-55}$ WT by at least 1 kcal/mol. However, directly at the position of the hinge motif (corresponding to G38 and V39 of C99 WT), k_{exp} and ΔG values drop to levels similar to the WT (~3.8 and 2.8 kcal/mol, respectively).

Comparing pL-GG and pL-VGGV to each other reveals that the two additional valine residues reduce the H-bond strengths by about 0.3 to 0.6 kcal/mol around the hinge motif plus the two flanking residues up- and downstream, respectively. This underlines the importance of the valines to the flexibility of the hinge.

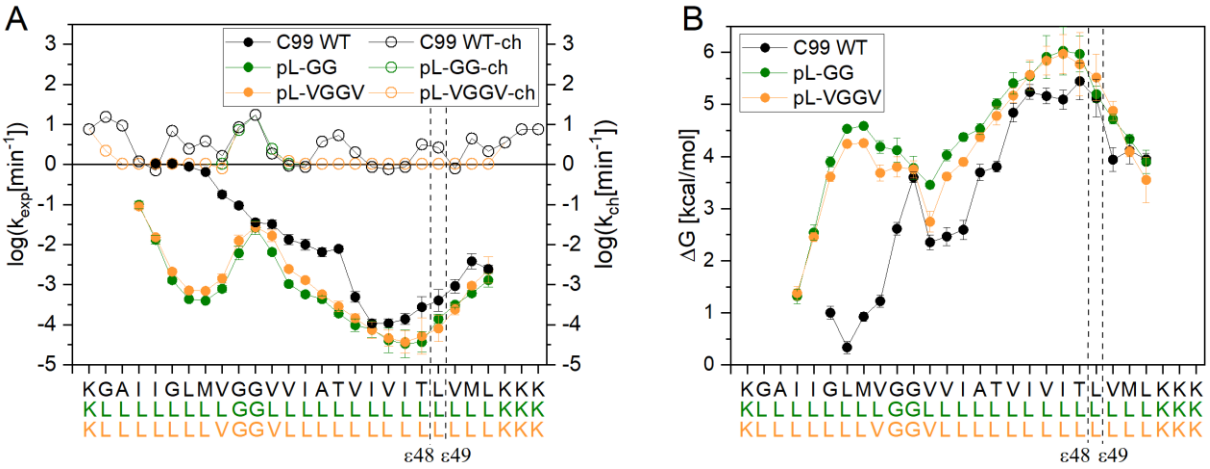

Figure 21: Deuterium-hydrogen exchange kinetics and H-bond stabilities of artificial pL-peptides with reconstituted hinge motif, determined by DHX-ETD.

A) DHX rate constants k_{exp} [min^{-1}] of individual amide deuterons (filled symbols, $n \geq 3$, mean values ± SE), derived from exponential fits of the residue-specific DHX kinetics (Figure S3). Residues without values are not sufficiently covered by data points. Empty symbols represent the respective chemical exchange rate constant k_{ch} [min^{-1}] that reflects the DHX kinetics in an unfolded state. B) Strength (ΔG) of intrahelical amide H-bonds based on individual k_{exp} values. Calculation of ΔG was not possible for residues where k_{exp} was not given or exceeded by k_{ch}. Error bars correspond to standard confidence intervals calculated from the standard errors of k_{exp}.

4.6.1.2 Effects of introducing the cleavage region

To investigate the role of the cleavage domain of C99 for backbone flexibility, the C99 sequence from V44 to L52 was introduced into the poly-Leu peptide, with and without the hinge motif (termed pL-VGGV-cr and pL-cr, respectively). The length of this part of the native C99 sequence was chosen to cover the ε-site between T48 and L49, as well as the respective H-bond network that spans from *i-4* to *i+4*.

In addition, recent papers showed that the C-terminal parts of C83 and Notch establish hybrid β-sheets together with the γ-secretase [141]. Consequently, high flexibility might be required to allow this refolding step of a substrate TMD. To enhance flexibility at the C-terminus, I also established the pL-εGG peptide, based on pL-VGGV with a GlyGly motif at the position of the ε-sites of the C99 TMD.

Remarkably, backbone H-bond strengths of pL-VGGV-cr were highly similar to the ones of pL-VGGV, explicitly also in the cleavage domain where the poly-Leu sequence was exchanged

to the native one of C99. The only difference between pL-VGGV-cr and pL-VGGV can be observed between I41 and T43 where pL-VGGV-cr is more flexible (by 0.3 to 0.6 kcal/mol). This indicates a conformational interaction between the cleavage domain and the core region between I41 and T43. The reason for the stabilized cleavage domain (compared to $C99_{28-55}$ WT) despite the native sequence of pL-VGGV-cr must be located in the upstream poly-Leu sequence. At the same time, increased flexibility of the central poly-Leu region (compared to pL-VGGV) must have its origin in the native sequence in the cleavage domain.

Similar to pL24, the isotope patterns of ETD fragments of pL-cr showed a bimodal shape and thus hindered analysis of exchange kinetics. Due to the unclear flexibility of the native C99 sequence in the cleavage domain of this construct, it is not possible to estimate plausible ΔG values.

Introducing the G48G49 mutation in the pL-εGG peptide causes a significant unfolding of the C-terminus. Weakened H-bonds, relative to the parental pL-VGGV, can be observed downstream of position I45. C-terminal of the G48G49 mutation, H-bond strengths only reach 1.2 - 1.5 kcal/mol. The N-terminal part is unaffected by this mutation.

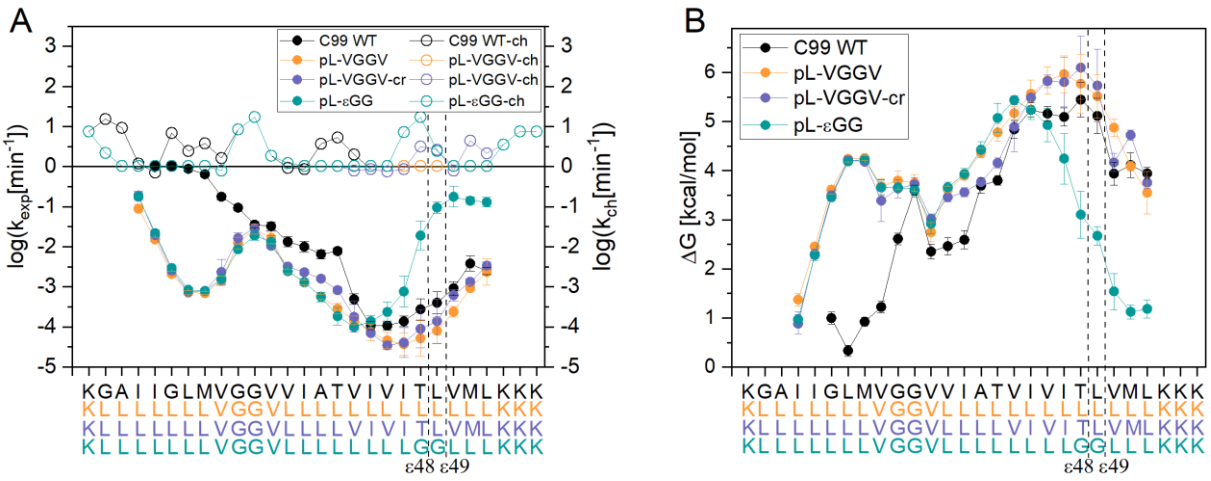

Figure 22: Deuterium-hydrogen exchange kinetics and H-bond stabilities of artificial pL-peptides with mutations addressing the ε-site.

A) DHX rate constants k_{exp} [min^{-1}] of individual amide deuterons (filled symbols, $n \geq 3$, mean values ± SE), derived from exponential fits of the residue-specific DHX kinetics (Figure S3). Residues without values are not sufficiently covered by data points. Empty symbols represent the respective chemical exchange rate constant k_{ch} [min^{-1}] that reflects the DHX kinetics in an unfolded state. B) Strength (ΔG) of intrahelical amide H-bonds based on individual k_{exp} values. Calculation of ΔG was not possible for residues where k_{exp} was not given or exceeded by k_{ch}. Error bars correspond to standard confidence intervals calculated from the standard errors of k_{exp}.

4.6.2 Effects of swapping regions to poly-Ala

In a second set of experiments, peptide composition was restricted to more helix-promoting leucine and the less helix-promoting alanine. Specifically, peptides with 15 N-terminal leucine residues, followed by nine alanine residues were introduced (pL-L15A9), as well as corresponding peptides with 15 N-terminal alanine residues, followed by nine leucines (pL-A15L9). The length of nine residues at the C-terminus was chosen for a better comparison to the pL-VGGV-cr and pL-cr peptides. Additionally, a very flexible poly-Ala TMD (pA) was analyzed. All peptides are listed in Table 6.

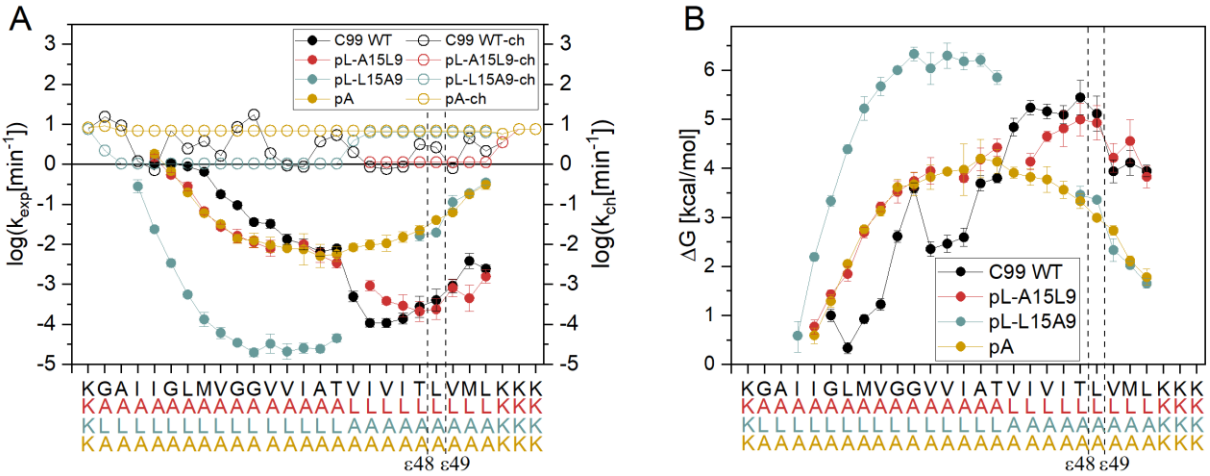

Figure 23: Deuterium-hydrogen exchange kinetics and H-bond stabilities of artificial poly-Leu/poly-Ala constructs.

A) DHX rate constants k_{exp} [min^{-1}] of individual amide deuterons (filled symbols, $n \geq 3$, mean values ± SE), derived from exponential fits of the residue-specific DHX kinetics (Figure S4). Residues without values are not sufficiently covered by data points. Empty symbols represent the respective chemical exchange rate constant k_{ch} [min^{-1}] that reflects the DHX kinetics in an unfolded state. B) Strength (ΔG) of intrahelical amide H-bonds based on individual k_{exp} values. Calculation of ΔG was not possible for residues where k_{exp} was not given or exceeded by k_{ch}. Error bars correspond to standard confidence intervals calculated from the standard errors of k_{exp}.

As expected, ΔG values indicate a very rigid N-terminal half of pL-L15A9 with H-bond strengths of up to 6.3 kcal/mol. In the same region, pL-A15L9 and pA show nearly identical H-bond strengths (up to 3.8 kcal/mol) which are below those of pL-L15A9. However, the latter two peptides with the alanine-composed N-terminal region are still more rigid than the $C99_{28-55}$ WT with its glycine-rich dimerization domain within TM-N.

Regarding the C-terminal region, the two peptides pA and pL-L15A9 that share the same poly-Ala sequence in the C-terminal part, also share the same ΔG values with a maximum of 3.8 kcal/mol. It must be noted that in the region of pL-L15A9 where the poly-Leu sequence shifts to poly-Ala, the first four residues do not show the regular sigmoidal exchange pattern. Consequently, these data could not be evaluated.

In comparison to pA and pL-L15A9, the C-terminal region of pL-A15L9 with the strongly helix-promoting poly-Leu sequence is more rigid with H-bond strengths of 4.5-5 kcal/mol. Thus, H-bond strength in the C-terminal region of pL-A15L9 is similar to the one of $C99_{28-55}$ WT.

Noteworthily, the H-bond strength in the C-terminal region of pL-A15L9 is significantly lower than in pL-GG and pL-VGGV (both around 6 kcal/mol) that also feature a poly-Leu sequence near the C-terminus. By contrast to these TMDs, the N-terminal part of pL-A15L9 is composed of poly-Ala. Thus, there seems to be a connection between the conformational flexibility of the N-terminal region of the peptide and the C-terminal region with the cleavage sites.

4.7 Gas-phase fragmentation as a method to measure H-bond strength

Based on the mobile-proton model (see 2.4.1) I hypothesized that gas-phase dissociation can be an economical approach to assess TMD backbone dynamics. As the model relies on the capture of a mobile proton by the carbonyl-oxygen of A_n prior to dissociation between A_n and A_{n+1}, I reasoned that fragmentation efficiency might be used as a measure of the accessibility of the carbonyl-oxygen at position *n* and thus report on the dynamics of the backbone H-bond that this carbonyl-oxygen is involved in.

To test this hypothesis, I applied CID to 3+, 4+ and 5+ charged peptides ($C99_{26-55}$ WT, as well as corresponding G38L and G39P mutants).

The resulting b- and y-fragment ions were counted and summed up for each respective residue. To compensate for variations in the peptides' concentrations or their likelihood of proper ionization, fragments were counted in % of the respective precursor peptide's intensity.

Initial results looked promising, with a pronounced accumulation of CID fragments around the flexible hinge area (Figure 24 A) and a clear difference between each peptide, according to their flexibility known from DHX. This means lower fragment intensities for the G38L mutant and enhanced fragmentation for the G38P mutant. However, the impact of the well documented primary structure effect on CID efficiency [183] remained unclear. Each residue affects the gas phase basicity of its carbonyl oxygen and thus its propensity of capturing a mobile proton. This effect is supposed to be short-ranged and not to affect the H-capture propensities of distant residues [183].

To clarify whether the observed fragmentation patterns were really related to the flexibility of the secondary structure, I introduced two short model-peptides, based on the previously used L16 peptides [196]. The first new peptide consisted of only 5 alternating leucines and valines, flanked by triple lysine anchors at each terminus and a tryptophan for quantification (LV5).

The second peptide was identical to LV5, except for a central glycine at position 3 (LV5-L3G, both peptides are listed in Table 7). Due to the short length of these two peptides, they showed no secondary structure, as confirmed by CD spectroscopy (Figure S5).

In gas-phase dissociation experiments, the LV5-L3G peptide showed higher fragmentation over the complete sequence beyond the glycine, compared to LV5 (Figure 24 B). This clearly indicates that the fragmentation-facilitating effect of the single glycine residue extends to distant positions, irrespective of any secondary structure. This was unexpected, considering the claims made by Zhang [183].

Thus, discriminating the effects of primary structure and secondary structure on observed fragmentation efficiencies remains an open problem that must be addressed before this method can be used as a measure of backbone H-bond flexibility.

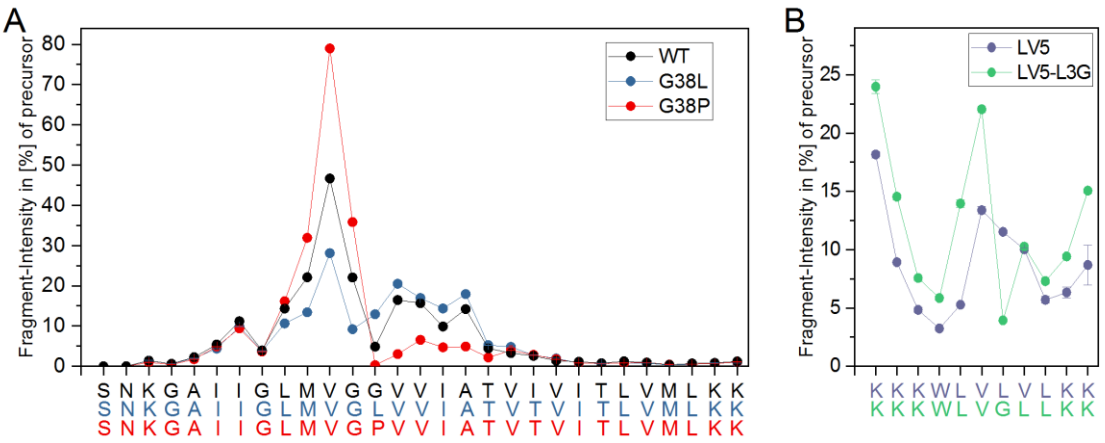

Figure 24: CID fragmentation profiles.

Summed up CID fragment-Intensities in [%] of the respective precursor-peptide ($n \geq 3$, error bars showing SE are smaller than the size of the symbols). Higher fragment intensity indicates more dissociation at the given position and indicates capture of a mobile proton. A) $C99_{26\text{-}55}$WT and corresponding G38L/P mutants. 3+, 4+ and 5+ charged peptides were used for fragmentation, 1+, 2+, 3+ b- and y-ions were counted. B) LV5 and LV5-L3G peptides. 2+, 3+ and 4+ charged peptides were used for fragmentation, 1+, 2+, 3+ b- and y-ions were counted.

5 Discussion

5.1 A new level of MS/MS DHX experiments

In this work, the Langosch group and I extended the widely used method of HDX/DHX-MS/MS experiments from a technique to measure global stability of proteins or peptides, to a method to precisely calculate individual amide H-bond strengths (ΔG) at each residue of a respective peptide. Thus, we are the first to systematically determine the exchange kinetics of each single amide group, based on ETD-fragments. I used these individual exchange kinetics to calculate the free energy ΔG of respective H-bonds. This allowed me to compare backbone flexibilities of different peptides at a previously unknown level of detail and precision. Also, these differences in backbone flexibility were correlated to cleavage efficiency and site specificity in γ-secretase mediated proteolysis, done in parallel by collaborators.

The aim of this effort was to investigate which properties of a γ-secretase substrate TMD determine a substrate as such and how cleavage is affected by the flexibility of different regions of the TMD.

All experiments that contributed to the mapping of ΔG values were performed in 80% TFE/H_2O and not in micelles due to several reasons. From a practical side, DPC micelles shielded the core regions of the peptides from exchange in HDX experiments, as shown by the global exchange kinetics (Figure 14). Also, removal of detergent prior to ETD is very likely to induce scrambling and compromise deuteration patterns.

From a theoretical point of view, 80% TFE is also the better choice, as I am not interested in the TMD flexibility in a membrane, but in the interior of γ-secretase. 80% TFE /H2O was shown to be a very good mimic for this environment, as polarity and water-accessibility match the ones found in the solvated interior of proteins [215–219].

I started by mapping the H-bond strengths of the native $C99_{28\text{-}55}$ WT TMD sequence. The results confirmed previous findings of a very flexible N-terminal region and a rigid cleavage domain in the C-terminal region [92,93,98,103,123,215]. While a local peak in ΔG at G38 may first seem counterintuitive to the reported hinge motif around V36G37G38V39 [91,95,103,215] one must keep in mind that we look at the amide groups from which the H-bonds originate and span to the residues at *i-4* (α-helix) or *i-3* (3_{10}-helix).

Thus, the H-bonds originating from the amide groups of V39 to I41 span across the hinge to the carbonyl oxygens of M35 to G37. Consequently, their drop in H-bond strengths (ΔΔG of

about 1.2 kcal/mol) compared to the flanking G38 and A42 residues, indicates rather weak H-bonds across the hinge motif and thus high flexibility.

At the same time, this first experiment was a good method to probe the theoretical assumptions and the kinetic model. Back-calculation of global DHX kinetics, based on the determined k_{exp} values of the single amide groups, showed very high concordance with the actual experimentally measured global exchange kinetics and confirmed the experimental approach.

However, estimation of exchange kinetics and ΔG values was not possible for all residues. Fraying of both terminal regions and lack of H-bond partners for the first three residues of the N-terminus led to very fast exchange in these regions and made it impossible to obtain deuterium levels that were sufficient for proper calculation of exchange rate constants. Also, exchange kinetics for these very fast exchanging amide groups often did not match the exponential fit supposed by the kinetic model. This could be caused by deuterium scrambling emanating from the terminal lysine residues which hold very labile side chain deuterons [173–175]. Also, exchange at the termini might be so fast that it is not completely slowed down at our stop conditions and thus may corrupt the estimation of deuterium levels, as the exchange slowly continues during the measurements.

A critical review of the experimental data showed that some single residue exchange kinetics did not perfectly match the monoexponential fit that is used to determine k_{exp} values. Specifically, exchange at the start of the exchange curve was frequently faster than during later periods (equivalent to the first 5-15% of the exchange curve). This was especially the case for unstable amides at frayed termini and near hinge regions. A plausible explanation for this is rare, correlated exchange. Correlated exchange is expected to accelerate DHX at the beginning of the exchange experiment but not at later periods where pairs of neighboring amide deuterons may be too rare to impact on k_{exp} upon correlated exchange. This means that k_{exp} values should be determined from the slower main parts of the exchange curves.
Since the fast initial parts only account for minor extents of the kinetics and since the density of data points prevented reliable biphasic fitting, I preferred monophasic fitting.
For the publication [227], my data was complemented by additional measurements in this early exchange phase and exchange curves were reevaluated. This reevaluation showed very little deviation to my data and indicated that all conclusions from this study are valid.

5.2 Impact of hinge and ε-site flexibility on cleavage efficiency and specificity

5.2.1 Effects of the hinge flexibility on cleavage efficiency and specificity

Recent studies showed that most FAD associated mutations are in the vicinity of the cleavage region [221]. However, they do not destabilize the helix around the ε-site. Significant effects are rather observed at upstream H-bonds, including the G37G38 hinge and the γ-sites [91,103,139,215]. Hence, a special focus in this thesis was put on how effects of mutations on the helix flexibility near the G37G38 hinge relate to cleavage efficiency, which was measured by others [220].

In detail, the aim was to alter hinge dynamics with the helix-promoting G38L mutation (stabilization) and the helix-perturbing G38P (destabilization). The expectation was that the stabilized hinge causes a reduction in cleavage efficiency, while an enhanced hinge shows the opposite effect.

DHX experiments showed that both mutations caused the expected impacts on the flexibility of their TMD backbones. In detail, the G38L mutant increased H-bond strengths (compared to $C99_{28\text{-}55}$ WT) by about 0.7-1.2 kcal/mol from V36 to T43 with the single exception of the mutation site itself (L38) where ΔG was 1.0 kcal/mol lower. So, stabilizing the hinge motif with leucine increased H-bond strengths and thus rigidity of the TMD over an extended distance, especially between the hinge motif and the γ-sites. This is of special interest, as MD simulations suggested a second hinge-like motif between T43 and I45 [215,222], which was not known at the time, when the experiment was designed. But as the data show, this second hinge also gets stabilized by the G38L mutation, at least partly.

The helix-distorting effect of proline in contrast, was rather short-ranged. ΔG calculations of the G38P mutant showed an extremely weak H-bond at V39 (ΔG ~ 0 kcal/mol) and highly reduced H-bond strengths for V40 and I41 (1.0 and 0.7 kcal/mol lower than $C99_{28\text{-}55}$ WT, respectively). A minor effect is also seen for V44 and I45 where ΔG values drop about 0.5 kcal/mol.

Proline was shown to have the strongest destabilizing effect of all amino acids on transmembrane helices [228,229]. This disruptive effect is also reflected by a significant enrichment of proline C-terminal of kinks, in general [230–234]. In a helix, proline at position *i* cannot establish an amide H-bond to residues *i-4* and *i-3*, while its side chain clashes with the *i-1* carbonyl oxygen [235]. As a result, proline can introduce permanent helix kinks. This can enhance helix flexibility in terms of bending or swivel motions [236,237] but might also lock the helix in a certain kinked conformation. Thus, the observed effects of the G38P mutant on the H-bond network matched our expectations.

For both G38X peptides, the ε-sites were unaffected by the respective mutation and very similar to $C99_{28-55}$ WT.

However, *in vitro* cleavage experiments of Mylonas *et al.* [220] revealed that in fact both mutations hamper cleavage efficiency dramatically. The impairing effect is even more pronounced for the G38P mutations and covers both AICD release and Aβ fragment production. This shows that cleavage efficiency is heavily impaired, even though the flexibility of the ε-sites is unaffected by the introduced mutations. Yet, this also indicates that cleavage efficiency is not directly related to flexibility around the hinge and the interpretation is more complex.
As described in the introduction (chapter 1.5), processing of the substrate involves the translocation of the substrate from its binding site [88] towards the active site of the enzyme complex, as well as fitting of the scissile bonds into the active site. It is likely that these steps require a substrate-TMD to adapt to the enzyme, presumably by evolving a pattern of conformational flexibility that facilitates substrate translocation and/or docking [27,102,238].
This pattern of conformations may involve bending and/or twisting motions of rigid regions around more flexible regions as shown by MD simulations [220].
It is plausible to assume that actually both mutations reduce this set of conformations, either by reduced flexibility around the hinge and the core region (G38L) or by the proline residue that was shown by NMR to induce a more pronounced kink in the helix (G38P) [239]. Consequently, translocation and/or fitting into the active site is hampered which reduces cleavage efficiency.

Additionally, with G38L, the major product of proteolysis changed from Aβ40 to Aβ37, indicating enhanced processivity. This effect was absent in the G38P mutation where, in contrast to the WT, no Aβ37 and Aβ38 species were produced at all. One can argue that this change in processivity is also an effect of an altered orientation or movements of TM-C, relative to TM-N. Another option is that the Aβ40 fragments of C99 WT and G38P are flexible enough to easily exit γ-secretase, while higher rigidity of G38L-Aβ40 fragments hampers release. The enhanced time in the active site of γ-secretase could enable the additional proteolytic cut to the Aβ37 fragment, which is finally flexible enough to exit the proteolytic complex. This idea was later supported by the experiments with the pL-based peptides (see chapter 5.3).

Taken together, mutating the hinge motif heavily affected cleavage efficiency, possibly mediated by hampering the translocation and fitting into the γ-secretase's active site, while there was no observable effect on the ε-site.

5.2.2 Effects of ε-site flexibility on cleavage efficiency and specificity

In their 2016 released publication, Fernandez *et al.* followed a quite direct approach to investigate the relationship between ε-site flexibility and cleavage efficiency. As proteolysis requires unfolding of the initial cleavage site, they exchanged I47 and T48 of C99 WT to helix-promoting leucine or helix-destabilizing glycine, respectively. In their study, the I47L/T48L mutation caused a 4-fold decrease of cleavage efficiency, while the introduction of the glycines at the same position increased efficiency by the factor of 3.5 [139].

These high discrepancies in cleavage efficiency were explained with the supposed flexibility of the cleavage region.

To investigate this theory in detail, I mapped the H-bond strengths of both mutant TMDs.

Surprisingly, both mutations increase flexibility of the cleavage region between V44 and L49. Still, the destabilizing effect is more pronounced for the double-glycine mutation and also extends to the C-terminus with a drastic drop of ΔG-values ~ 2kcal/mol lower than the WT, downstream of T48.

What is the reason for this surprising result? Previous publications already pointed out, how the side chains of T43 and T48 establish H-bonds to the TMD's backbone and thus stabilize the helix [103,215]. Mutating these residues alters cleavage efficiency at the ε-site, as well as ε-site preference [103,112,113,140].

Consequently, mutating T48 to either Gly or Leu eradicates this stabilizing back-bonding interaction to V44. While helix flexibility is strongly increased with the destabilizing Gly mutation, the helix-promoting Leu mutation can partially compensate for this loss of the additional H-bond by enhanced side chain to side chain interactions [212].

Interestingly, both mutations also feature an increased flexibility around the hinge motif. This indicates a long-range interaction between the hinge, the newly discovered second hinge from T43 to I45 [215,222] and the Thr side chains in the cleavage region.

How does this match with the reported cleavage data?

In case of the double-glycine mutation, the results fit the expectations. In fact, there are several factors that might contribute to the enhanced cleavage efficiency. First, as expected by Fernandez *et al.* [139], flexibility around the cleavage site is enhanced, indicated by lower H-bond strengths. This may facilitate refolding to fit conformational requirements in the active site as well as unfolding prior to proteolysis. Second, H-bond strengths are also reduced around both hinge motifs. As already discussed in chapter 5.2.1, these regions may provide the flexibility needed for the translocation from the binding site towards the active site. A higher flexibility

in these regions might facilitate or accelerate access to the active site which ultimately increases cleavage efficiency. Third, glycine is known to attract H_2O molecules and might thereby increase the concentration of the catalyst in the active site.

Yet, looking at the backbone flexibility reveals no clear reason for the reduced efficiency of the I47L/T48L mutant. Both mutants feature very similar ΔG-values around the prominent G37G38 hinge, as well as at the second hinge around T43 to I45. Thus, increased conformational flexibility is expected to facilitate cleavage. Starting from T48, the I47LT48L mutant shows stronger H-bonds than the I47G/T48G variant but is similar to the WT or even lower (L51), which also cannot explain the 4-fold reduction in cleavage efficiency. What else might explain this outcome? It is possible that the large side chains of Leu sterically hinder cleavage and thus reduce its efficiency.
To sum up, there is no simple, direct correlation between cleavage efficiency and the stability around the ε-site. Instead, higher flexibility around the ε-site might facilitate cleavage but is not mandatory and other aspects, like steric hindrance, may contribute to cleavage efficiency, as well.

5.2.3 How the I45T FAD mutation alters TMD flexibility and the cleavage process

The I45T FAD mutation exhibits strongly reduced cleavage efficiency [112,113], but in contrast to most FAD mutations, the preferential cleavage site remains at ε49 [111]. I therefore reasoned that this mutation could offer an exclusive insight into the reasons underlying changed efficiency, independent of an altered cleavage site. Also, changes in backbone flexibility might explain the later pathway-switch from the initial Aβ40 product line towards the Aβ42 product line.

ETD experiments revealed that the TMD H-bond strengths are highly similar between I45T and C99 WT. The only difference can be found between I41 and T43 where I45T showed slightly increased ΔG values. This is caused by the additional H-bond between the side chain of T45 and the carbonyl-oxygen of I41, which strengthens the H-bond network and rigidifies the helical turn in between. Similar effects had been observed for T43 and T48 [103,215]. As a result of this additional H-bond, the flexible region between T43 and I/T45 is rigidified, reducing the flexibility at the ε-site, relative to TM-N and the center of the helix. Similar to the G38X mutations (chapter 5.2.1), this reduction of conformational space may limit the ability of I45T to fit the ε-site in the active center of γ-secretase in the right position.

However, this mutation it does not seem to alter the flexibility around the ε-site and downstream. This is evident from the highly similar H-bond strengths between I45T and the WT in this region. So, once the peptide is located in the active site, it will likely establish the same hybrid β-sheet with γ-secretase as the wild type and lock the peptide in the "correct" position. Therefore, the ε-site preference is not changed.

After the initial cleavage, the altered backbone dynamics around the ζ- and γ-cleavage sites might come into play during the "repositioning" of the peptide into the catalytic cleft and cause the switch towards the Aβ42 product line, resulting in increased levels of Aβ42 and Aβ38. Note that this switch must occur prior to the second cleavage step, since this cleavage removes T45 from the remaining Aβ fragment and thus its impact on the substrate's dynamics. This idea is supported by MD-simulations which suggest a combined unwinding/sliding mechanism for the repositioning of the substrate's scissile bond to induce subsequent hydrolysis steps [240]. It is possible that this combined unwinding/sliding mechanism is affected by the increased backbone strength of the I45T mutation.

5.3 General requirements for a γ-secretase substrate

Based on the first results of the C99 mutations, a second set of experiments was designed to systematically investigate how conformational flexibility defines substrates and non-substrates of γ-secretase. Cleavage data for this project were provided by my cooperation partners Dr. Nadine Werner (*in vitro* assays) and Gökhan Güner (*in cellulo* assays) [227]. In general, we evaluated the efficiency of both, AICD and Aβ, fragment production. *In cellulo* assays always confirmed the trends observed in the *in vitro* studies. The basis for this approach was a poly-Leu TMD (termed pL) that was shown to be practically uncleavable by γ-secretase in both assays.

We first grafted the short G37G38 hinge motif, as well as the extended V36G37G38V39 hinge motif into the pL TMD. DHX experiments confirmed that both motifs induce a hinge with weak H-bonds in an otherwise very rigid TMD. The destabilizing effect was significantly stronger with the extended VGGV hinge motif. This is in line with previous publications that pointed out the importance of the two valine residues in the flexibility of the hinge [103,212]. Noteworthily, both peptides feature a significantly more rigid N-terminal part, compared to the C99 WT. Cleavage assays revealed that the G37G38 hinge motif is sufficient to restore cleavability by γ-secretase, at least partly (33% AICD and 19% Aβ of WT). Cleavage efficiency was even higher with the extended hinge motif (40% AICD and 26% Aβ of WT). That shows how crucial this region is for the conformational flexibility that may be required for substrate translocation and to enter the catalytic cleft, as discussed above.

Interestingly, for both peptides, the preferential cleavage site was shifted to the position that corresponds to ε48 in C99. Moreover, the most abundant Aβ-fragment was Aβ34, indicating strongly enhanced processivity.

Apart from the hinge, we also investigated the ε-site. We probed the effect of enhanced flexibility on cleavage by changing the ε-site to G48G49 (pL-εGG). The latter peptide was expected to be a "supersubstrate" as it features the hinge motif of pL-VGGV and a highly flexible cleavage domain, which should facilitate refolding in the active site to establish the hybrid β-sheet and unfolding prior to proteolysis. In fact, DHX experiments confirmed very low H-bond strengths around the ε-site and downstream, especially between the residues M51 to K54 that are involved in the hybrid β-sheet with presenilin [141].

However, cleavage assays report efficiencies that are nearly identical to pL-VGGV. Thus, the extremely flexible C-terminus has no effect on the cleavage efficiency. Consequently, the two steps of β-sheet formation and unfolding before proteolysis are not rate-limiting.

In addition, we grafted the C99 sequence from V44 to L52 onto the poly-Leu peptide, with and without the hinge motif. The length of the native C99 sequence was chosen in a way that it covers the ε-site between T48 and L49, as well as the respective H-bond network that spans from *i-4* (for the amide groups) to *i+4* (for the carbonyl oxygens). pL-VGGV-cr showed that adding the native cleavage region to pL-VGGV significantly enhanced AICD and Aβ production to 82% and 68% of WT, respectively.

The ΔG profile of pL-VGGV-cr is very interesting, as it is nearly identical to the parental pL-VGGV, explicitly also in the swapped region between V44 and L52. Thus, the H-bond strengths in the grafted region are somewhat higher than in the WT.

The only difference in the ΔG profiles of pL-VGGV and pL-VGGV-cr is between I41 and T43, where pL-VGGV-cr is highly similar to the WT. This is the exact region that was previously found to be of high relevance with the G38X mutations (chapter 5.2.1), as well as I45T (chapter 5.2.3). This indicates two interesting aspects:

First, there is a conformational interaction between the cleavage region and the central region of the TMD. Swapping in of the native sequence destabilizes the upstream central region (pL-VGGV-cr compared to pL-VGGV) to levels similar of the WT. The other way around, helix-promoting poly-Leu in the central region stabilizes the cleavage region (compared to the WT). Second, the second "hinge" around T43, suggested by MD simulations [215,222], may thus be of high relevance in the fine-tuning of the conformational flexibility that facilitates the

translocation of the substrate and the fitting into the catalytic cleft and by this determines cleavage efficiency.

For pL-cr, cleavage assays found efficiencies similar to pL-VGGV. Hence, the cleavage region itself must also provide some features that enable cleavage, irrespective of the hinge motif. Unfortunately, pL-cr could not be measured via DHX-ETD, as it showed bimodal isotope patterns, similar to pL. Based on the results of pL-VGGV-cr, lowered H-bond strengths at the second hinge around T43 can be assumed for pL-cr. However, this is rather speculative, and it is unclear how pronounced this effect is without the flexibility from the first hinge around V36G37G38V39. So, cleavability of pL-cr might be enhanced by the conformational flexibility of the second hinge around T43-I45, but this could not be confirmed experimentally.
In summary, unfolding of the ε-site and C-terminus is not rate-limiting, while weaker H-bonds in the center of the TMD enable more conformational flexibility and enhance cleavage efficiency.

Cleavage assays also revealed that all three peptides had their preferential cleavage site at the position equivalent to ε48 with additional minor cleavage at ε49. The most abundant Aβ-fragment was Aβ34 for pL-εGG and pL-VGGV-cr and Aβ36 for pL-cr. These Aβ-fragments are much shorter than the products of WT or FAD mutations.
The latter finding indicates that the progress of the stepwise proteolytic process in γ-secretase depends on the flexibility of the substrate's N-terminal region. All pL-peptides that I analyzed are highly similar N-terminal of the G37G38 hinge motif and substantially more rigid than the WT (ΔΔG up to 4 kcal/mol). At the same time, H-bond strengths C-terminal of this hinge vary significantly, as does cleavage efficiency.
Yet, the surprisingly short Aβ-fragments occur with all pL-peptides. This makes it unlikely, that the final Aβ-fragment length depends on the positioning of the substrate in the catalytic cleft or the cleavage efficiency. Instead, the strong N-terminal H-bond network of the pL-peptides could reduce the flexibility, which is required for the release of the remaining fragment from the catalytic cleft. Consequently, the substrate remains longer in the catalytic cleft and proteolysis progresses until the remaining fragment is short/flexible enough to exit the γ-secretase. The more rigid the N-terminal half is, the longer the substrate stays in the catalytic cleft and the shorter the finally released Aβ-like-fragments are. This idea is in line with the results of G38L where N-terminal H-bonds are stronger than the WT but weaker than the pL-peptides and a shift from Aβ40 to Aβ37 is observed. Additionally, it was already shown for

some FAD mutations of PS1 that the dissociation rate of the fragment affects the length of the released product [126,127].

It must be noted that this concept proposes additional cleavage steps in case of more rigid substrates and not a "skipping" of the γ40- or γ42-cleavage-sites due to increased H-bonds strengths. ΔG values at these γ-cleavage-sites were always weaker than at the ε-and ζ-sites (except for pL-εGG). Also, results from the peptides with double glycines at the ε-site show that H-bond strength itself is irrelevant for the cleavage efficiency at this site. Thus, a skipping is rather unlikely. However, this idea does not explain how most substrate FAD mutations that are located in the cleavage region (and are therefore cleaved off, prior to the final cleavage steps) can alter Aβ38 and Aβ37 levels.

The initial cleavage sites of all pL-peptides at position 48 and 49 match the ones of the C99 WT, although the preferential cleavage site is shifted from ε49 to the position corresponding to ε48. This applies to all pL-peptides, irrespective of the sequence or the flexibility in the cleavage region. This indicates that ε-cleavage by γ-secretase is largely independent from the substrate's sequence. The initial cleavage site rather depends on the presentation of the scissile sites to the catalytic aspartates as a result of the overall geometry of the substrate/enzyme complex. The exact positioning of the scissile sites relative to the enzyme is probably fine-tuned by the conformational flexibility of the substrate's TMD, resulting in a preferential cleavage site at ε48 or ε49, respectively. Of course, positioning of the substrate relative to the active site might also be altered by the numerous FAD mutations in presenilin, which were not in the focus of this work. [88,221]

Unfortunately, it was not possible to obtain cleavage results for the peptides with the poly-Ala sequences. These peptides could be very interesting to further probe our assumptions about cleavage efficiency as a result of conformational flexibility. In detail, I would expect pL-L15A9 to show very low cleavage efficiencies, as its backbone is very stable till position 43 and does not feature any kind of hinge motif. The rather flexible C-terminus should have no beneficial effect, based on the observations of the I47G/T48G mutation and the pL-εGG peptide.

In contrast, I would expect the cleavage efficiencies of pA and pL-A15L9 to be lower than the C99 WT, but significantly higher than pL-L15A9, based on the ΔG values in their central region. Both peptides only differ in the H-bond strengths in the C-terminal cleavage region. As ΔG values around the cleavage site are shown to be not rate-limiting, I expect highly similar cleavage efficiencies for pA and pL-A15L9.

5.4 Summary and Outlook

Results from the $C99_{28-55}$ WT based mutants and the artificial model peptides based on pL draw a coherent picture of the correlation between cleavage by γ-secretase and substrate TMD flexibility. A combination of sophisticated DHX experiments and cleavage assays revealed four major findings:

First, flexibility of the C-terminal region has no impact on cleavage efficiency. Neither refolding of the substrate to establish the reported hybrid β-sheet [141,142] nor unfolding prior to proteolysis seems to be rate-limiting.

Second, a hinge motif in the center of the peptide plays a crucial role for cleavage by γ-secretase. Altering the G37G38 hinge motif in C99 dramatically lowered cleavage efficiency. At the same time, introducing the hinge motif into an otherwise uncleavable poly-Leu sequence, partially restored proteolysis by γ-secretase. Above that, enhancing this hinge motif with V36 and V39 further increased cleavage efficiency. Additionally, recent studies discussed a second hinge around T43 of C99 [215,222]. The results from the pL-VGGV-cr and I45T peptides are consistent with the idea that this region highly affects the fine-tuning of substrate-enzyme interaction and plays a major role for cleavage efficiency. As discussed earlier and also supported by MD-simulations [239], these hinges enable bending motions that allow C99 to enter presenilin and subsequently its catalytic cleft.

Transferred to γ-secretase substrates in general, this indicates that translocation from the binding site and subsequent fitting into the catalytic cleft requires a certain amount of flexibility or a hinge motif in the center of the TMD. This enables a specific set of conformational movements and flexibility between TM-N and TM-C that allows adapting of the substrate to the structure and dynamics of γ-secretase surface during translocation.

Consequently, cleavage rate is driven by the ability of the respective substrate to move around the steric hindrances of the presenilin TMDs during translocation and its ability to form a cleavage-competent state in the catalytic cleft. The latter might by influenced by effects of the primary sequence, as seen with the I47T48 mutants, i.e., by steric hindrances or the attraction of catalytic water molecules.

This model is supported by observed flexible regions within the TMD of other γ-secretase substrates, such as Notch1 [241]. Even more, the same principle is also discussed for other transmembrane proteases of the SPP and SPPL families, where removal of flexible regions in the TMD of the substrates Xbp1u and TNFα reduces or even abolished cleavability [194,242].

Third, the position of ε-site cleavage is not very sequence specific. Rather presentation of a bond to the catalytic aspartates may be determined by the overall geometry of the substrate/enzyme complex.

Fourth, the H-bond network in the N-terminal region could define the length of the final Aβ or Aβ-like fragments. The results indicate that stronger H-bonds in TM-N lead to shorter fragments. The reason might be that a more rigid TM-N hinders release of the remaining fragment from the enzyme. As the peptide remains longer in the catalytic cleft, the stepwise proteolysis continues further, until the shorter fragments are finally able to exit.

What does this mean for the role of γ-secretase?

Given the high relevance of intramembrane-proteolysis and the drastic consequences of miscleavage, proteolysis by γ-secretase appears to be surprisingly simple and unspecific.

Discrimination between substrates and non-substrates is likely just a matter of flexibility in the core-region of the TMD. This of course implies that the given substrate's ectodomain is short enough to fit under nicastrin and enter the γ-secretase-complex.

Currently, there are 149 known substrates of γ-secretase [34] but only 2 clearly established non-substrates, namely integrin β1 (ITGB1) [75] and telencephalin (ICAM-5). [243,244]. This overabundance of substrates indicates that the conformational requirements are met by the majority of type-1 transmembrane proteins.

Due to this large number of known substrates, γ-secretase was already discussed to be the "proteasome of the membrane" [43,245]. The rather poor discrimination between substrates and non-substrates, at least from their TMD, seems to support this theory. Even more that we now know that the exact cleavage site is not sequence-specific but instead depends on the positioning of the substrate in the catalytic cleft.

However, for at least 61 of the 149 known substrates, there is good evidence that their cleavage by γ-secretase has functional consequences [34]. This clearly contradicts a somewhat erratic "digestion" by γ-secretase.

What else might define the function of γ-secretase?

The main difference between the currently known substrates is their turnover-rate. Cleavage efficiency is driven by the ability of the respective substrate to move around the steric hindrances of the presenilin TMDs during translocation and enter its catalytic cleft.

These differences in cleavage efficiency might be the discrimination between *functional* substrates and non-substrates in the physiological context of a cell.

It was already shown that the two prominent γ-secretase substrates APP and Notch1 have disparate exosite preferences [246–248]. This suggests different translocation pathways after the initial binding, even though both peptides probably enter the catalytic cleft via the same gate which is discussed to form between TMD2 and TMD6 [249–251] or TMD2 and TMD3 [246] of PS1.

Thus, it is likely that different potential substrates feature alternate translocation pathways and compete against each other for cleavage in the catalytic cleft. The ones that manage the translocation process faster could surpass and supersede the slower ones. This would cause that in the cell, only the proteins with a fast translocation (measured as high turn-over rates) serve as actual substrates of γ-secretase.

Transmembrane proteolysis is very slow and takes minutes to hours [28,29]. As the chemistry of peptide bond hydrolysis is rather fast (k_{cat} rates >1 s^{-1} [137]), this indicates long translocation times and thus enough space for competition between potential substrates.

It would be interesting to see, whether the 61 substrates of which we know of functional consequences in the cell, also feature higher cleavage rates, compared to the ones without known consequences. The latter ones might also have functional consequences, which we are just not aware of by now, though.

Another aspect that is completely left out in this thesis is the effect of the ectodomains.

Recent studies pointed out their importance for proteolysis by γ-secretase. The length of the ECD after shedding affects the cleavage specificity of APP [76,252,253]. Moreover, mutations in the ECD of APP also change the cleavage efficiency [254,255]. For other γ-secretase substrates it was shown that swapping the extramembrane domains can inhibit cleavage of their TMD. [256,257]

It appears that a rather complex combination of the conformational flexibility of the TMD and the effects of the ECD defines the cleavage process of γ-secretase. To further investigate this combination will be a challenging task for the future.

The findings in this work also propose potential targets for the future treatment or rather prevention of Alzheimer's disease:

The problem with the FAD mutants is the release of the longer and therefore more hydrophobic Aβ42 fragments which are prone to form neurotoxic aggregates. Results from the pL-peptides indicate that prolonged time in the catalytic cleft leads to the release of shorter Aβ-like fragments.

Thus, forcing the Aβ fragments to stay longer in the catalytic cleft before release, might facilitate additional cleavage to shorter fragments like Aβ38 or Aβ34. This could be an interesting target for future pharmaceuticals. The shorter fragments are less likely to form aggregates and would therefore prevent formation of amyloid plaques.

Drugs targeting the release of Aβ fragments would also not hamper the release of often functional ICD fragments, which is a major problem with the current γ-secretase-inhibitors.

6 References

1. Nelson, D. L. & Cox, M. M. *Lehninger Principles of Biochemistry (5th ed.)*. (2008).
2. Berg, J., Tymoczko, J. & Stryer, L. *Stryer Biochemie*. (Springer Spektrum, 2014).
3. Klebba, P. E. The Porinologist. *J Bacteriol* **187**, 8232–8236 (2005).
4. Tamm, L. K., Hong, H. & Liang, B. Folding and assembly of β-barrel membrane proteins. *Biochimica et Biophysica Acta (BBA) - Biomembranes* **1666**, 250–263 (2004).
5. Lichtenthaler, S. F., Haass, C. & Steiner, H. Regulated intramembrane proteolysis - lessons from amyloid precursor protein processing. *J Neurochem* **117**, 779–796 (2011).
6. Strisovsky, K. Structural and mechanistic principles of intramembrane proteolysis - lessons from rhomboids. *FEBS Journal* **280**, 1579–1603 (2013).
7. Wolfe, M. S. Processive proteolysis by γ-secretase and the mechanism of Alzheimer's disease. *bchm* **393**, 899–905 (2012).
8. Vinothkumar, K. R. & Freeman, M. Intramembrane proteolysis by rhomboids: catalytic mechanisms and regulatory principles. *Curr Opin Struct Biol* **23**, 851–858 (2013).
9. Wolfe, M. S. Intramembrane-cleaving Proteases. *Journal of Biological Chemistry* **284**, 13969–13973 (2009).
10. Aster, J. C., Pear, W. S. & Blacklow, S. C. The Varied Roles of Notch in Cancer. *Annual Review of Pathology: Mechanisms of Disease* **12**, 245–275 (2017).
11. Sharma, V. M., Draheim, K. M. & Kelliher, M. A. The Notch1/c-Myc Pathway in T Cell Leukemia. *Cell Cycle* **6**, 927–930 (2007).
12. Weng, A. P. *et al.* Activating Mutations of NOTCH1 in Human T Cell Acute Lymphoblastic Leukemia. *Science (1979)* **306**, 269–271 (2004).
13. Göthert, J. R. *et al.* NOTCH1 pathway activation is an early hallmark of SCL T leukemogenesis. *Blood* **110**, 3753–3762 (2007).
14. Chan, E. Y. L. & McQuibban, G. A. The mitochondrial rhomboid protease: Its rise from obscurity to the pinnacle of disease-relevant genes. *Biochimica et Biophysica Acta (BBA) - Biomembranes* **1828**, 2916–2925 (2013).
15. Sun, L., Li, X. & Shi, Y. Structural biology of intramembrane proteases: mechanistic insights from rhomboid and S2P to γ-secretase. *Curr Opin Struct Biol* **37**, 97–107 (2016).
16. Uzman, A. Molecular biology of the cell (4th ed.): Alberts, B., Johnson, A., Lewis, J., Raff, M., Roberts, K., and Walter, P. *Biochemistry and Molecular Biology Education* **31**, 212–214 (2003).
17. Wolfe, M. S. *et al.* Two transmembrane aspartates in presenilin-1 required for presenilin endoproteolysis and γ-secretase activity. *Nature* **398**, 513–517 (1999).
18. De Strooper, B. *et al.* A presenilin-1-dependent γ-secretase-like protease mediates release of Notch intracellular domain. *Nature* **398**, 518–522 (1999).
19. De Strooper, B., Iwatsubo, T. & Wolfe, M. S. Presenilins and -Secretase: Structure, Function, and Role in Alzheimer Disease. *Cold Spring Harb Perspect Med* **2**, a006304–a006304 (2012).
20. Friedmann, E. *et al.* SPPL2a and SPPL2b promote intramembrane proteolysis of TNFα in activated dendritic cells to trigger IL-12 production. *Nat Cell Biol* **8**, 843–848 (2006).
21. Weihofen, A., Binns, K., Lemberg, M. K., Ashman, K. & Martoglio, B. Identification of Signal Peptide Peptidase, a Presenilin-Type Aspartic Protease. *Science (1979)* **296**, 2215–2218 (2002).
22. Urban, S., Lee, J. R. & Freeman, M. Drosophila Rhomboid-1 Defines a Family of Putative Intramembrane Serine Proteases. *Cell* **107**, 173–182 (2001).

23. Rawson, R. B. *et al.* Complementation Cloning of S2P, a Gene Encoding a Putative Metalloprotease Required for Intramembrane Cleavage of SREBPs. *Mol Cell* **1**, 47–57 (1997).
24. Kroos, L. & Akiyama, Y. Biochemical and structural insights into intramembrane metalloprotease mechanisms. *Biochimica et Biophysica Acta (BBA) - Biomembranes* **1828**, 2873–2885 (2013).
25. Manolaridis, I. *et al.* Mechanism of farnesylated CAAX protein processing by the intramembrane protease Rce1. *Nature* **504**, 301–305 (2013).
26. Hampton, S. E., Dore, T. M. & Schmidt, W. K. Rce1: mechanism and inhibition. *Crit Rev Biochem Mol Biol* **53**, 157–174 (2018).
27. Langosch, D., Scharnagl, C., Steiner, H. & Lemberg, M. K. Understanding intramembrane proteolysis: from protein dynamics to reaction kinetics. *Trends Biochem Sci* **40**, 318–327 (2015).
28. Dickey, S. W., Baker, R. P., Cho, S. & Urban, S. Proteolysis inside the Membrane Is a Rate-Governed Reaction Not Driven by Substrate Affinity. *Cell* **155**, 1270–1281 (2013).
29. Kamp, F. *et al.* Intramembrane Proteolysis of β-Amyloid Precursor Protein by γ-Secretase Is an Unusually Slow Process. *Biophys J* **108**, 1229–1237 (2015).
30. Arutyunova, E. *et al.* Allosteric regulation of rhomboid intramembrane proteolysis. *EMBO J* **33**, 1869–1881 (2014).
31. Sanders, C. R. & Hutchison, J. M. Membrane properties that shape the evolution of membrane enzymes. *Curr Opin Struct Biol* **51**, 80–91 (2018).
32. Beard, H. A., Barniol-Xicota, M., Yang, J. & Verhelst, S. H. L. Discovery of Cellular Roles of Intramembrane Proteases. *ACS Chem Biol* **14**, 2372–2388 (2019).
33. Haapasalo, A. & Kovacs, D. M. The Many Substrates of Presenilin/γ-Secretase. *Journal of Alzheimer's Disease* **25**, 3–28 (2011).
34. Güner, G. & Lichtenthaler, S. F. The substrate repertoire of γ-secretase/presenilin. *Semin Cell Dev Biol* **105**, 27–42 (2020).
35. Struhl, G. & Greenwald, I. Presenilin is required for activity and nuclear access of Notch in Drosophila. *Nature* **398**, 522–525 (1999).
36. Sato, C., Zhao, G. & Xenia G. Ilagan, Ma. An Overview of Notch Signaling in Adult Tissue Renewal and Maintenance. *Curr Alzheimer Res* **9**, 227–240 (2012).
37. Schroeter, E. H., Kisslinger, J. A. & Kopan, R. Notch-1 signalling requires ligand-induced proteolytic release of intracellular domain. *Nature* **393**, 382–386 (1998).
38. Cao, X. A Transcriptively Active Complex of APP with Fe65 and Histone Acetyltransferase Tip60. *Science (1979)* **293**, 115–120 (2001).
39. Hébert, S. S. *et al.* Regulated intramembrane proteolysis of amyloid precursor protein and regulation of expression of putative target genes. *EMBO Rep* **7**, 739–745 (2006).
40. Parent, A. T. Presenilin Attenuates Receptor-Mediated Signaling and Synaptic Function. *Journal of Neuroscience* **25**, 1540–1549 (2005).
41. Marambaud, P. *et al.* A CBP Binding Transcriptional Repressor Produced by the PS1/ϵ-Cleavage of N-Cadherin Is Inhibited by PS1 FAD Mutations. *Cell* **114**, 635–645 (2003).
42. Jurisch-Yaksi, N., Sannerud, R. & Annaert, W. A fast growing spectrum of biological functions of γ-secretase in development and disease. *Biochimica et Biophysica Acta (BBA) - Biomembranes* **1828**, 2815–2827 (2013).
43. Kopan, R. & Ilagan, Ma. X. G. γ-Secretase: proteasome of the membrane? *Nat Rev Mol Cell Biol* **5**, 499–504 (2004).
44. Lauritzen, I. *et al.* The β-Secretase-Derived C-Terminal Fragment of βAPP, C99, But Not Aβ, Is a Key Contributor to Early Intraneuronal Lesions in Triple-Transgenic Mouse Hippocampus. *Journal of Neuroscience* **32**, 16243–16255 (2012).

45. Bittner, T. *et al.* γ-Secretase Inhibition Reduces Spine Density In Vivo via an Amyloid Precursor Protein-Dependent Pathway. *Journal of Neuroscience* **29**, 10405–10409 (2009).
46. Mitani, Y. *et al.* Differential Effects between γ-Secretase Inhibitors and Modulators on Cognitive Function in Amyloid Precursor Protein-Transgenic and Nontransgenic Mice. *Journal of Neuroscience* **32**, 2037–2050 (2012).
47. Acx, H. *et al.* Inactivation of γ-secretases leads to accumulation of substrates and non-Alzheimer neurodegeneration. *EMBO Mol Med* **9**, 1088–1099 (2017).
48. Tamayev, R., Matsuda, S., Arancio, O. & D'Adamio, L. β- but not γ-secretase proteolysis of APP causes synaptic and memory deficits in a mouse model of dementia. *EMBO Mol Med* **4**, 171–179 (2012).
49. Edbauer, D. *et al.* Reconstitution of γ-secretase activity. *Nat Cell Biol* **5**, 486–488 (2003).
50. Kimberly, W. T. *et al.* γ-Secretase is a membrane protein complex comprised of presenilin, nicastrin, aph-1, and pen-2. *Proceedings of the National Academy of Sciences* **100**, 6382–6387 (2003).
51. Takasugi, N. *et al.* The role of presenilin cofactors in the γ-secretase complex. *Nature* **422**, 438–441 (2003).
52. Steiner, H. *et al.* A Loss of Function Mutation of Presenilin-2 Interferes with Amyloid β-Peptide Production and Notch Signaling. *Journal of Biological Chemistry* **274**, 28669–28673 (1999).
53. Kimberly, W. T., Xia, W., Rahmati, T., Wolfe, M. S. & Selkoe, D. J. The Transmembrane Aspartates in Presenilin 1 and 2 Are Obligatory for γ-Secretase Activity and Amyloid β-Protein Generation. *Journal of Biological Chemistry* **275**, 3173–3178 (2000).
54. Dries, D. & Yu, G. Assembly, Maturation, and Trafficking of the γ-Secretase Complex in Alzheimers Disease. *Curr Alzheimer Res* **5**, 132–146 (2008).
55. Podlisny, M. B. *et al.* Presenilin Proteins Undergo Heterogeneous Endoproteolysis between Thr291and Ala299and Occur as Stable N- and C-Terminal Fragments in Normal and Alzheimer Brain Tissue. *Neurobiol Dis* **3**, 325–337 (1997).
56. Fukumori, A., Fluhrer, R., Steiner, H. & Haass, C. Three-Amino Acid Spacing of Presenilin Endoproteolysis Suggests a General Stepwise Cleavage of γ-Secretase-Mediated Intramembrane Proteolysis. *Journal of Neuroscience* **30**, 7853–7862 (2010).
57. Beher, D. *et al.* Pharmacological Knock-down of the Presenilin 1 Heterodimer by a Novel γ-Secretase Inhibitor. *Journal of Biological Chemistry* **276**, 45394–45402 (2001).
58. Thinakaran, G. *et al.* Endoproteolysis of Presenilin 1 and Accumulation of Processed Derivatives In Vivo. *Neuron* **17**, 181–190 (1996).
59. Yu, G. *et al.* The Presenilin 1 Protein Is a Component of a High Molecular Weight Intracellular Complex That Contains β-Catenin. *Journal of Biological Chemistry* **273**, 16470–16475 (1998).
60. Meckler, X. & Checler, F. Presenilin 1 and Presenilin 2 Target γ-Secretase Complexes to Distinct Cellular Compartments. *Journal of Biological Chemistry* **291**, 12821–12837 (2016).
61. Sannerud, R. *et al.* Restricted Location of PSEN2/γ-Secretase Determines Substrate Specificity and Generates an Intracellular Aβ Pool. *Cell* **166**, 193–208 (2016).
62. Yu, G. *et al.* Nicastrin modulates presenilin-mediated notch/glp-1 signal transduction and βAPP processing. *Nature* **407**, 48–54 (2000).
63. Lu, P. *et al.* Three-dimensional structure of human γ-secretase. *Nature* **512**, 166–170 (2014).

64. Bolduc, D. M., Montagna, D. R., Gu, Y., Selkoe, D. J. & Wolfe, M. S. Nicastrin functions to sterically hinder γ-secretase–substrate interactions driven by substrate transmembrane domain. *Proceedings of the National Academy of Sciences* **113**, E509–E518 (2016).
65. Hébert, S. S. *et al.* Coordinated and widespread expression of γ-secretase in vivo: evidence for size and molecular heterogeneity. *Neurobiol Dis* **17**, 260–272 (2004).
66. Shirotani, K., Edbauer, D., Prokop, S., Haass, C. & Steiner, H. Identification of Distinct γ-Secretase Complexes with Different APH-1 Variants. *Journal of Biological Chemistry* **279**, 41340–41345 (2004).
67. Francis, R. *et al.* aph-1 and pen-2 Are Required for Notch Pathway Signaling, γ-Secretase Cleavage of βAPP, and Presenilin Protein Accumulation. *Dev Cell* **3**, 85–97 (2002).
68. Steiner, H. *et al.* PEN-2 Is an Integral Component of the γ-Secretase Complex Required for Coordinated Expression of Presenilin and Nicastrin. *Journal of Biological Chemistry* **277**, 39062–39065 (2002).
69. Sun, L. *et al.* Structural basis of human γ-secretase assembly. *Proceedings of the National Academy of Sciences* **112**, 6003–6008 (2015).
70. Zhang, X., Yu, C. J. & Sisodia, S. S. The topology of pen-2, a γ-secretase subunit, revisited: evidence for a reentrant loop and a single pass transmembrane domain. *Mol Neurodegener* **10**, 39 (2015).
71. Bai, X. *et al.* An atomic structure of human γ-secretase. *Nature* **525**, 212–217 (2015).
72. Bai, X.-C., Rajendra, E., Yang, G., Shi, Y. & Scheres, S. H. Sampling the conformational space of the catalytic subunit of human γ-secretase. *Elife* **4**, e11182–e11182 (2015).
73. Vincent, B. & Checler, F. α-Secretase in Alzheimers Disease and Beyond: Mechanistic, Regulation and Function in the Shedding of Membrane Proteins. *Curr Alzheimer Res* **9**, 140–156 (2012).
74. Laurent, S. A. *et al.* γ-secretase directly sheds the survival receptor BCMA from plasma cells. *Nat Commun* **6**, 7333 (2015).
75. Hemming, M. L., Elias, J. E., Gygi, S. P. & Selkoe, D. J. Proteomic Profiling of γ-Secretase Substrates and Mapping of Substrate Requirements. *PLoS Biol* **6**, e257 (2008).
76. Funamoto, S. *et al.* Substrate ectodomain is critical for substrate preference and inhibition of γ-secretase. *Nat Commun* **4**, 2529 (2013).
77. Struhl, G. & Adachi, A. Requirements for Presenilin-Dependent Cleavage of Notch and Other Transmembrane Proteins. *Mol Cell* **6**, 625–636 (2000).
78. Hayashi, I. *et al.* Neutralization of the γ-secretase activity by monoclonal antibody against extracellular domain of nicastrin. *Oncogene* **31**, 787–798 (2012).
79. Zhang, X. *et al.* Identification of a tetratricopeptide repeat-like domain in the nicastrin subunit of γ-secretase using synthetic antibodies. *Proceedings of the National Academy of Sciences* **109**, 8534–8539 (2012).
80. Müller, U. C., Deller, T. & Korte, M. Not just amyloid: physiological functions of the amyloid precursor protein family. *Nat Rev Neurosci* **18**, 281–298 (2017).
81. Selkoe, D. J. & Hardy, J. The amyloid hypothesis of Alzheimer's disease at 25 years. *EMBO Mol Med* **8**, 595–608 (2016).
82. Vassar, R., Kovacs, D. M., Yan, R. & Wong, P. C. The γ-Secretase Enzyme BACE in Health and Alzheimer's Disease: Regulation, Cell Biology, Function, and Therapeutic Potential. *Journal of Neuroscience* **29**, 12787–12794 (2009).
83. Morishima-Kawashima, M. Molecular mechanism of the intramembrane cleavage of the β-carboxyl terminal fragment of amyloid precursor protein by γ-secretase. *Front Physiol* **5**, (2014).

84. Lichtenthaler, S. F. α-secretase in Alzheimer's disease: molecular identity, regulation and therapeutic potential. *J Neurochem* **116**, 10–21 (2011).
85. Zhang, X. & Song, W. The role of APP and BACE1 trafficking in APP processing and amyloid-β generation. *Alzheimers Res Ther* **5**, 46 (2013).
86. Nunan, J. & Small, D. H. Regulation of APP cleavage by α-, β- and γ-secretases. *FEBS Lett* **483**, 6–10 (2000).
87. Hur, J.-Y. γ-Secretase in Alzheimer's disease. *Exp Mol Med* **54**, 433–446 (2022).
88. Fukumori, A. & Steiner, H. Substrate recruitment of γ-secretase and mechanism of clinical presenilin mutations revealed by photoaffinity mapping. *EMBO J* **35**, 1628–1643 (2016).
89. Das, A. *et al.* X-ray Snapshot of HIV-1 Protease in Action: Observation of Tetrahedral Intermediate and Short Ionic Hydrogen Bond SIHB with Catalytic Aspartate. *J Am Chem Soc* **132**, 6366–6373 (2010).
90. Suguna, K., Padlan, E. A., Smith, C. W., Carlson, W. D. & Davies, D. R. Binding of a reduced peptide inhibitor to the aspartic proteinase from Rhizopus chinensis: implications for a mechanism of action. *Proceedings of the National Academy of Sciences* **84**, 7009–7013 (1987).
91. Stelzer, W., Scharnagl, C., Leurs, U., Rand, K. D. & Langosch, D. The Impact of the 'Austrian' Mutation of the Amyloid Precursor Protein Transmembrane Helix is Communicated to the Hinge Region. *ChemistrySelect* **1**, 4408–4412 (2016).
92. Pester, O., Götz, A., Multhaup, G., Scharnagl, C. & Langosch, D. The cleavage domain of the amyloid precursor protein transmembrane helix does not exhibit above-average backbone dynamics. *ChemBioChem* **14**, 1943–1948 (2013).
93. Pester, O. *et al.* The backbone dynamics of the amyloid precursor protein transmembrane helix provides a rationale for the sequential cleavage mechanism of γ-secretase. *J Am Chem Soc* **135**, 1317–1329 (2013).
94. Chen, W. *et al.* Familial Alzheimer's mutations within APPTM increase Aβ42 production by enhancing accessibility of ε-cleavage site. *Nat Commun* **5**, 3037 (2014).
95. Barrett, P. J. *et al.* The Amyloid Precursor Protein Has a Flexible Transmembrane Domain and Binds Cholesterol. *Science (1979)* **336**, 1168–1171 (2012).
96. Nadezhdin, K. D., Bocharova, O. V, Bocharov, E. V & Arseniev, A. S. Structural and dynamic study of the transmembrane domain of the amyloid precursor protein. *Acta Naturae* **3**, 69–76 (2011).
97. Miyashita, N., Straub, J. E. & Thirumalai, D. Structures of β-Amyloid Peptide 1−40, 1−42, and 1−55—the 672−726 Fragment of APP—in a Membrane Environment with Implications for Interactions with γ-Secretase. *J Am Chem Soc* **131**, 17843–17852 (2009).
98. Dominguez, L., Foster, L., Straub, J. E. & Thirumalai, Dave. Impact of membrane lipid composition on the structure and stability of the transmembrane domain of amyloid precursor protein. *Proceedings of the National Academy of Sciences* **113**, E5281–E5287 (2016).
99. Dominguez, L., Meredith, S. C., Straub, J. E. & Thirumalai, D. Transmembrane fragment structures of amyloid precursor protein depend on membrane surface curvature. *J Am Chem Soc* **136**, 854–857 (2014).
100. Miyashita, N., Straub, J. E., Thirumalai, D. & Sugita, Y. Transmembrane Structures of Amyloid Precursor Protein Dimer Predicted by Replica-Exchange Molecular Dynamics Simulations. *J Am Chem Soc* **131**, 3438–3439 (2009).
101. Lemmin, T., Dimitrov, M., Fraering, P. C. & Dal Peraro, M. Perturbations of the straight transmembrane α-helical structure of the amyloid precursor protein affect its processing by γ-secretase. *Journal of Biological Chemistry* **289**, 6763–6774 (2014).

102. Langosch, D. & Steiner, H. Substrate processing in intramembrane proteolysis by γ-secretase – the role of protein dynamics. *Biol Chem* **398**, 441–453 (2017).
103. Scharnagl, C. *et al.* Side-chain to main-chain hydrogen bonding controls the intrinsic backbone dynamics of the amyloid precursor protein transmembrane helix. *Biophys J* **106**, 1318–1326 (2014).
104. Sastre, M. *et al.* Presenilin-dependent γ-secretase processing of β-amyloid precursor protein at a site corresponding to the S3 cleavage of Notch. *EMBO Rep* **2**, 835–841 (2001).
105. Gu, Y. *et al.* Distinct Intramembrane Cleavage of the β-Amyloid Precursor Protein Family Resembling γ-Secretase-like Cleavage of Notch. *Journal of Biological Chemistry* **276**, 35235–35238 (2001).
106. Yu, C. *et al.* Characterization of a Presenilin-mediated Amyloid Precursor Protein Carboxyl-terminal Fragment γ. *Journal of Biological Chemistry* **276**, 43756–43760 (2001).
107. Weidemann, A. *et al.* A Novel ε-Cleavage within the Transmembrane Domain of the Alzheimer Amyloid Precursor Protein Demonstrates Homology with Notch Processing. *Biochemistry* **41**, 2825–2835 (2002).
108. Qi-Takahara, Y. Longer Forms of Amyloid Protein: Implications for the Mechanism of Intramembrane Cleavage by γ-Secretase. *Journal of Neuroscience* **25**, 436–445 (2005).
109. Takami, M. *et al.* γ-Secretase: Successive Tripeptide and Tetrapeptide Release from the Transmembrane Domain of β-Carboxyl Terminal Fragment. *J Neurosci* **29**, 13042–13052 (2009).
110. Zhao, G. *et al.* γ-Cleavage Is Dependent on ζ-Cleavage during the Proteolytic Processing of Amyloid Precursor Protein within Its Transmembrane Domain. *Journal of Biological Chemistry* **280**, 37689–37697 (2005).
111. Bolduc, D. M., Montagna, D. R., Seghers, M. C., Wolfe, M. S. & Selkoe, D. J. The amyloid-beta forming tripeptide cleavage mechanism of γ-secretase. *Elife* **5**, 1–21 (2016).
112. Chávez-Gutiérrez, L. *et al.* The mechanism of γ-Secretase dysfunction in familial Alzheimer disease. *EMBO J* **31**, 2261–2274 (2012).
113. Xu, T.-H. *et al.* Alzheimer's disease-associated mutations increase amyloid precursor protein resistance to γ-secretase cleavage and the Aβ42/Aβ40 ratio. *Cell Discov* **2**, 16026 (2016).
114. Selkoe, D. J. Alzheimer's Disease. *Cold Spring Harb Perspect Biol* **3**, a004457–a004457 (2011).
115. Iwatsubo, T. *et al.* Visualization of Aβ42(43) and Aβ40 in senile plaques with end-specific Aβ monoclonals: Evidence that an initially deposited species is Aβ42(43). *Neuron* **13**, 45–53 (1994).
116. Levy-Lahad, E. *et al.* Candidate Gene for the Chromosome 1 Familial Alzheimer's Disease Locus. *Science (1979)* **269**, 973–977 (1995).
117. Rogaev, E. I. *et al.* Familial Alzheimer's disease in kindreds with missense mutations in a gene on chromosome 1 related to the Alzheimer's disease type 3 gene. *Nature* **376**, 775–778 (1995).
118. Sherrington, R. *et al.* Cloning of a gene bearing missense mutations in early-onset familial Alzheimer's disease. *Nature* **375**, 754–760 (1995).
119. Citron, M. *et al.* Mutant presenilins of Alzheimer's disease increase production of 42-residue amyloid β-protein in both transfected cells and transgenic mice. *Nat Med* **3**, 67–72 (1997).
120. Scheuner, D. *et al.* Secreted amyloid β–protein similar to that in the senile plaques of Alzheimer's disease is increased in vivo by the presenilin 1 and 2 and APP mutations linked to familial Alzheimer's disease. *Nat Med* **2**, 864–870 (1996).

121. Borchelt, D. R. *et al.* Familial Alzheimer's Disease–Linked Presenilin 1 Variants Elevate Aβ1–42/1–40 Ratio In Vitro and In Vivo. *Neuron* **17**, 1005–1013 (1996).
122. Murayama, O. *et al.* Enhancement of amyloid β 42 secretion by 28 different presenilin 1 mutations of familial Alzheimer's disease. *Neurosci Lett* **265**, 61–63 (1999).
123. Sato, T. *et al.* A helix-to-coil transition at the ε-cut site in the transmembrane dimer of the amyloid precursor protein is required for proteolysis. *Proceedings of the National Academy of Sciences* **106**, 1421–1426 (2009).
124. Fernandez, M. A., Klutkowski, J. A., Freret, T. & Wolfe, M. S. Alzheimer Presenilin-1 Mutations Dramatically Reduce Trimming of Long Amyloid β-Peptides (Aβ) by γ-Secretase to Increase 42-to-40-Residue Aβ. *Journal of Biological Chemistry* **289**, 31043–31052 (2014).
125. Szaruga, M. *et al.* Qualitative changes in human γ-secretase underlie familial Alzheimer's disease. *Journal of Experimental Medicine* **212**, 2003–2013 (2015).
126. Okochi, M. *et al.* γ-Secretase Modulators and Presenilin 1 Mutants Act Differently on Presenilin/γ-Secretase Function to Cleave Aβ42 and Aβ43. *Cell Rep* **3**, 42–51 (2013).
127. Szaruga, M. *et al.* Alzheimer's-Causing Mutations Shift Aβ Length by Destabilizing γ-Secretase-Aβn Interactions. *Cell* **170**, 443-456.e14 (2017).
128. Weggen, S. & Beher, D. Molecular consequences of amyloid precursor protein and presenilin mutations causing autosomal-dominant Alzheimer's disease. *Alzheimers Res Ther* **4**, 9 (2012).
129. Munter, L.-M. *et al.* Aberrant Amyloid Precursor Protein (APP) Processing in Hereditary Forms of Alzheimer Disease Caused by APP Familial Alzheimer Disease Mutations Can Be Rescued by Mutations in the APP GxxxG Motif. *Journal of Biological Chemistry* **285**, 21636–21643 (2010).
130. Page, R. C. *et al.* β-Amyloid Precursor Protein Mutants Respond to γ-Secretase Modulators. *Journal of Biological Chemistry* **285**, 17798–17810 (2010).
131. Suzuki, N. *et al.* An Increased Percentage of Long Amyloid β Protein Secreted by Familial Amyloid β Protein Precursor (βApp717) Mutants. *Science (1979)* **264**, 1336–1340 (1994).
132. Yin, Y. I. *et al.* γ-Secretase Substrate Concentration Modulates the Aβ42/Aβ40 Ratio. *Journal of Biological Chemistry* **282**, 23639–23644 (2007).
133. Kakuda, N. *et al.* Equimolar Production of Amyloid β-Protein and Amyloid Precursor Protein Intracellular Domain from β-Carboxyl-terminal Fragment by γ-Secretase. *Journal of Biological Chemistry* **281**, 14776–14786 (2006).
134. Olsson, F. *et al.* Characterization of intermediate steps in amyloid beta (Aβ) production under near-native conditions. *J Biol Chem* **289**, 1540–1550 (2014).
135. Sato, T. *et al.* Potential Link between Amyloid β-Protein 42 and C-terminal Fragment γ 49–99 of β-Amyloid Precursor Protein. *Journal of Biological Chemistry* **278**, 24294–24301 (2003).
136. Beel, A. J. & Sanders, C. R. Substrate specificity of γ-secretase and other intramembrane proteases. *Cellular and Molecular Life Sciences* **65**, 1311–1334 (2008).
137. Grossman, M. *et al.* Correlated structural kinetics and retarded solvent dynamics at the metalloprotease active site. *Nat Struct Mol Biol* **18**, 1102–1108 (2011).
138. Ousson, S. *et al.* Substrate determinants in the C99 juxtamembrane domains differentially affect γ-secretase cleavage specificity and modulator pharmacology. *J Neurochem* **125**, 610–619 (2013).
139. Fernandez, M. A. *et al.* Transmembrane Substrate Determinants for γ-Secretase Processing of APP CTFβ. *Biochemistry* **55**, 5675–5688 (2016).
140. Dimitrov, M. *et al.* Alzheimer's disease mutations in APP but not γ-secretase modulators affect epsilon-cleavage-dependent AICD production. *Nat Commun* **4**, 2246 (2013).

141. Zhou, R. *et al.* Recognition of the amyloid precursor protein by human γ-secretase. *Science (1979)* **363**, (2019).
142. Yang, G. *et al.* Structural basis of Notch recognition by human γ-secretase. *Nature* **565**, 192–197 (2019).
143. Englander, S. W. & Krishna, M. M. G. Hydrogen exchange. *Nat Struct Mol Biol* **8**, 741–742 (2001).
144. Bai, Y., Milne, J. S., Mayne, L. & Englander, S. W. Primary structure effects on peptide group hydrogen exchange. *Proteins: Structure, Function, and Bioinformatics* **17**, 75–86 (1993).
145. Teilum, K., Kragelund, B. B. & Poulsen, F. M. Application of Hydrogen Exchange Kinetics to Studies of Protein Folding. in *Protein Folding Handbook* 634–672 (Wiley, 2005). doi:10.1002/9783527619498.ch18.
146. Brier, S. and Engen, J. R. Hydrogen Exchange Mass Spectrometry: Principles and Capabilities. in *Mass spectrometry analysis for protein-protein interactions and dynamics; Chance, M., Ed.; Wiley-Blackwell: New York* vol. 1 11–43 (2008).
147. Connelly, G. P., Bai, Y., Jeng, M. F. & Englander, S. W. Isotope effects in peptide group hydrogen exchange. *Proteins* **17**, 87–92 (1993).
148. Hvidt, A. & Nielsen, S. O. Hydrogen exchange in proteins. *Adv Protein Chem* **21**, 287–386 (1966).
149. Hvidt, A. A discussion of the pH dependance of the hydrogen-deuterium exchange of proteins. *C R Trav Lab Carlsberg* (1964).
150. Hilton, B. D. & Woodward, C. K. Mechanism of isotope exchange kinetics of single protons in bovine pancreatic trypsin inhibitor. *Biochemistry* **18**, 5834–5841 (1979).
151. Woodward, C. K. & Hilton, B. D. Hydrogen isotope exchange kinetics of single protons in bovine pancreatic trypsin inhibitor. *Biophys J* **32**, 561–575 (1980).
152. Mayo, S. L. & Baldwin, R. L. Guanidinium Chloride Induction of Partial Unfolding in Amide Proton Exchange in RNase A. *Science (1979)* **262**, 873–876 (1993).
153. Qian, H., Mayo, S. L. & Morton, A. Protein Hydrogen Exchange in Denaturant: Quantitative Analysis by a Two-Process Model. *Biochemistry* **33**, 8167–8171 (1994).
154. Bai, Y., Sosnick, T. R., Mayne, L. & Englander, S. W. Protein Folding Intermediates: Native-State Hydrogen Exchange. *Science (1979)* **269**, 192–197 (1995).
155. Xiao, H. *et al.* Mapping protein energy landscapes with amide hydrogen exchange and mass spectrometry: I. A generalized model for a two-state protein and comparison with experiment. *Protein Science* **14**, 543–557 (2005).
156. Weis, D. D., Engen, J. R. & Kass, I. J. Semi-automated data processing of hydrogen exchange mass spectra using HX-Express. *J Am Soc Mass Spectrom* **17**, 1700–1703 (2006).
157. Ferraro, D. M., Lazo, N. D. & Robertson, A. D. EX1 Hydrogen Exchange and Protein Folding. *Biochemistry* **43**, 587–594 (2004).
158. Sivaraman, T., Arrington, C. B. & Robertson, A. D. Kinetics of unfolding and folding from amide hydrogen exchange in native ubiquitin. *Nat Struct Biol* (2001).
159. Eaton, W. A. *et al.* Fast Kinetics and Mechanisms in Protein Folding. *Annu Rev Biophys Biomol Struct* **29**, 327–359 (2000).
160. Veglia, G., Carolina Zeri, A., Ma, C. & Opella, S. J. Deuterium/Hydrogen Exchange Factors Measured by Solution Nuclear Magnetic Resonance Spectroscopy as Indicators of the Structure and Topology of Membrane Proteins. *Biophys J* **82**, 2176–2183 (2002).
161. Loh, S. N. & Markley, J. L. Hydrogen Bonding in Proteins As Studied by Amide Hydrogen D/H Fractionation Factors: Application to Staphylococcal Nuclease. *Biochemistry* **33**, 1029–1036 (1994).

162. Khare, D., Alexander, P. & Orban, J. Hydrogen Bonding and Equilibrium Protium−Deuterium Fractionation Factors in the Immunoglobulin G Binding Domain of Protein G. *Biochemistry* **38**, 3918–3925 (1999).
163. Edison, A. S., Weinhold, F., Markley, J. L., Weinhold, F. & Markley, J. L. Theoretical Studies of Protium/Deuterium Fractionation Factors and Cooperative Hydrogen Bonding in Peptides. *J Am Chem Soc* **117**, 9619–9624 (1995).
164. Bowers, P. M. & Klevit, R. E. Hydrogen bonding and equilibrium isotope enrichment in histidine-containing proteins. *Nat Struct Biol* (1996).
165. Parker, M. J. & Clarke, A. R. Amide backbone and water-related H/D isotope effects on the dynamics of a protein folding reaction. *Biochemistry* **36**, 5786–5794 (1997).
166. Krantz, B. A. *et al.* Understanding protein hydrogen bond formation with kinetic H/D amide isotope effects. *Nat Struct Biol* **9**, 458–463 (2002).
167. Jaravine, V. A., Cordier, F. & Grzesiek, S. Quantification of H/D Isotope Effects on Protein Hydrogen-bonds by h3 J NC and 1 J NC′ Couplings and Peptide Group 15 N and 13 C′ Chemical Shifts. *J Biomol NMR* **29**, 309–318 (2004).
168. Bowie, J. U. Membrane protein folding: How important are hydrogen bonds? *Current Opinion in Structural Biology* **21**(1), 42-49, (2011).
169. Linderstrom-Lang, K. U. Deuterium exchange and protein structure. *Neuberger, A., editor. Symposium on Protein Structure. London: Methuen* 23–34 (1958).
170. Linderstrom-Lang, K. U. Schellman, J. A. Protein structure and enzyme activity. *In: Boyer PD, Lardy H, Myrback K, editors. The enzymes. New York: Academic Press* **1**, 443–510 (1959).
171. Qian, H. & Chan, S. I. Hydrogen exchange kinetics of proteins in denaturants: a generalized two-process model. *J Mol Biol* **286**, 607–616 (1999).
172. Zhurov, K. O., Fornelli, L., Wodrich, M. D., Laskay, U. A. & Tsybin, Y. O. Principles of electron capture and transfer dissociation mass spectrometry applied to peptide and protein structure analysis. *Chem Soc Rev* **42**, 5014–5030 (2013).
173. Jørgensen, T. J. D., Bache, N., Roepstorff, P., Gårdsvoll, H. & Ploug, M. Collisional Activation by MALDI Tandem Time-of-flight Mass Spectrometry Induces Intramolecular Migration of Amide Hydrogens in Protonated Peptides. *Molecular & Cellular Proteomics* **4**, 1910–1919 (2005).
174. Jørgensen, T. J. D., Gårdsvoll, H., Ploug, M. & Roepstorff, P. Intramolecular Migration of Amide Hydrogens in Protonated Peptides upon Collisional Activation. *J Am Chem Soc* **127**, 2785–2793 (2005).
175. Rand, K. D., Adams, C. M., Zubarev, R. A. & Jorgensen, T. J. Electron capture dissociation proceeds with a low degree of intramolecular migration of peptide amide hydrogens. *J Am Chem Soc* **130**, 1341–1349 (2008).
176. Pringle, S. D. *et al.* An investigation of the mobility separation of some peptide and protein ions using a new hybrid quadrupole/travelling wave IMS/oa-ToF instrument. *Int J Mass Spectrom* **261**, 1–12 (2007).
177. Rand, K. D., Pringle, S. D., Morris, M., Engen, J. R. & Brown, J. M. ETD in a traveling wave ion guide at tuned Z-spray ion source conditions allows for site-specific hydrogen/deuterium exchange measurements. *J Am Soc Mass Spectrom* **22**, 1784–1793 (2011).
178. Wysocki, V. H., Tsaprailis, G., Smith, L. L. & Breci, L. A. Mobile and localized protons: a framework for understanding peptide dissociation. *Journal of Mass Spectrometry* **35**, 1399–1406 (2000).
179. Schlosser, A. & Lehmann, W. D. Five-membered ring formation in unimolecular reactions of peptides: a key structural element controlling low-energy collision-induced dissociation of peptides. *Journal of Mass Spectrometry* **35**, 1382–1390 (2000).

180. McCormack, A. L., Somogyi, A., Dongre, A. R. & Wysocki, V. H. Fragmentation of protonated peptides: surface-induced dissociation in conjunction with a quantum mechanical approach. *Anal Chem* **65**, 2859–2872 (1993).
181. Dongré, A. R., Somogyi, Á. & Wysocki, V. H. Surface-induced Dissociation: An Effective Tool to Probe Structure, Energetics and Fragmentation Mechanisms of Protonated Peptides. *Journal of Mass Spectrometry* **31**, 339–350 (1996).
182. Savitski, M. M., Kjeldsen, F., Nielsen, M. L. & Zubarev, R. A. Complementary sequence preferences of electron-capture dissociation and vibrational excitation in fragmentation of polypeptide polycations. *Angew Chem Int Ed Engl* **45**, 5301–5303 (2006).
183. Zhang, Z. Prediction of Low-Energy Collision-Induced Dissociation Spectra of Peptides. *Anal Chem* **76**, 3908–3922 (2004).
184. Savitski, M. M. *et al.* Backbone carbonyl group basicities are related to gas-phase fragmentation of peptides and protein folding. *Angew Chem Int Ed Engl* **46**, 1481–1484 (2007).
185. Skinner, O. S. *et al.* Fragmentation of integral membrane proteins in the gas phase. *Anal Chem* **86**, 4627–4634 (2014).
186. Zubarev, R. A., Kelleher, N. L. & McLafferty, F. W. Electron Capture Dissociation of Multiply Charged Protein Cations. A Nonergodic Process. *J Am Chem Soc* **120**, 3265–3266 (1998).
187. Sawicka, A., Skurski, P., Hudgins, R. R. & Simons, J. Model Calculations Relevant to Disulfide Bond Cleavage via Electron Capture Influenced by Positively Charged Groups. *J Phys Chem B* **107**, 13505–13511 (2003).
188. Syrstad, E. & Turecček, F. Toward a general mechanism of electron capture dissociation. *J Am Soc Mass Spectrom* **16**, 208–224 (2005).
189. Henry, E. R., Eaton, W. A. & Hochstrasser, R. M. Molecular dynamics simulations of cooling in laser-excited heme proteins. *Proc Natl Acad Sci U S A* **83**, 8982–8986 (1986).
190. Zhang, Z. Prediction of electron-transfer/capture dissociation spectra of peptides. *Anal Chem* **82**, 1990–2005 (2010).
191. Krężel, A. & Bal, W. A formula for correlating pKa values determined in D2O and H2O. *J Inorg Biochem* **98**, 161–166 (2004).
192. Rand, K. D., Pringle, S. D., Morris, M. & Brown, J. M. Site-specific analysis of gas-phase hydrogen/deuterium exchange of peptides and proteins by electron transfer dissociation. *Anal Chem* **84**, 1931–1940 (2012).
193. Skinner, J. J., Lim, W. K., Bédard, S., Black, B. E. & Englander, S. W. Protein dynamics viewed by hydrogen exchange. *Protein Science* **21**, 996–1005 (2012).
194. Yücel, S. S. *et al.* The Metastable XBP1u Transmembrane Domain Defines Determinants for Intramembrane Proteolysis by Signal Peptide Peptidase. *Cell Rep* **26**, 3087-3099.e11 (2019).
195. Rand, K. D., Zehl, M., Jensen, O. N. & Jorgensen, T. J. Loss of ammonia during electron-transfer dissociation of deuterated peptides as an inherent gauge of gas-phase hydrogen scrambling. *Anal Chem* **82**, 9755–9762 (2010).
196. Högel, P. *et al.* Glycine Perturbs Local and Global Conformational Flexibility of a Transmembrane Helix. *Biochemistry* **57**, 1326–1337 (2018).
197. Lauterwein, J., Bösch, C., Brown, L. R. & Wüthrich, K. Physicochemical studies of the protein-lipid interactions in melittin-containing micelles. *Biochimica et Biophysica Acta (BBA) - Biomembranes* **556**, 244–264 (1979).
198. Vinogradova, O., Sönnichsen, F. & Sanders, I. C. R. On choosing a detergent for solution NMR studies of membrane proteins. *J Biomol NMR* **11**, 381–386 (1998).

199. Arora, A. & Tamm, L. K. Biophysical approaches to membrane protein structure determination. *Curr Opin Struct Biol* **11**, 540–547 (2001).
200. Baleja, J. D. Structure Determination of Membrane-Associated Proteins from Nuclear Magnetic Resonance Data. *Anal Biochem* **288**, 1–15 (2001).
201. Choowongkomon, K., Carlin, C. R. & Sönnichsen, F. D. A Structural Model for the Membrane-bound Form of the Juxtamembrane Domain of the Epidermal Growth Factor Receptor. *Journal of Biological Chemistry* **280**, 24043–24052 (2005).
202. Oxenoid, K. & Chou, J. J. The structure of phospholamban pentamer reveals a channel-like architecture in membranes. *Proceedings of the National Academy of Sciences* **102**, 10870–10875 (2005).
203. Caillet-Saguy, C. *et al.* Mapping the Interaction between the Hemophore HasA and Its Outer Membrane Receptor HasR Using CRINEPT−TROSY NMR Spectroscopy. *J Am Chem Soc* **131**, 1736–1744 (2009).
204. Gorzelle, B. M. *et al.* Reconstitutive Refolding of Diacylglycerol Kinase, an Integral Membrane Protein. *Biochemistry* **38**, 16373–16382 (1999).
205. Yaseen, M., Wang, Y., Su, T. J. & Lu, J. R. Surface adsorption of zwitterionic surfactants: n-alkyl phosphocholines characterised by surface tensiometry and neutron reflection. *J Colloid Interface Sci* **288**, 361–370 (2005).
206. Lazaridis, T., Mallik, B. & Chen, Y. Implicit Solvent Simulations of DPC Micelle Formation. *J Phys Chem B* **109**, 15098–15106 (2005).
207. Kallick, D. A., Tessmer, M. R., Watts, C. R. & Li, C. Y. The Use of Dodecylphosphocholine Micelles in Solution NMR. *J Magn Reson B* **109**, 60–65 (1995).
208. Van Dam-Mieras, M. C. E., Slotboom, A. J., Pieterson, W. A. & De Haas, G. H. Interaction of phospholipase A2 with micellar interfaces. Role of the N-terminal region. *Biochemistry* **14**, 5387–5394 (1975).
209. Stafford, R. E., Fanni, T. & Dennis, E. A. Interfacial properties and critical micelle concentration of lysophospholipids. *Biochemistry* **28**, 5113–5120 (1989).
210. NAKAGAKI, M., KOMATSU, H. & HANDA, T. Estimation of critical micelle concentrations of lysolecithins with fluorescent probes. *Chem Pharm Bull (Tokyo)* **34**, 4479–4485 (1986).
211. Palladino, P., Rossi, F. & Ragone, R. Effective Critical Micellar Concentration of a Zwitterionic Detergent: A Fluorimetric Study on n-Dodecyl Phosphocholine. *J Fluoresc* **20**, 191–196 (2010).
212. Quint, S. *et al.* Residue-specific side-chain packing determines the backbone dynamics of transmembrane model helices. *Biophys J* **99**, 2541–2549 (2010).
213. Konermann, L., Pan, J. & Liu, Y.-H. Hydrogen exchange mass spectrometry for studying protein structure and dynamics. *Chem. Soc. Rev.* **40**, 1224–1234 (2011).
214. Konermann, L., Vahidi, S. & Sowole, M. A. Mass spectrometry methods for studying structure and dynamics of biological macromolecules. *Anal Chem* **86**, 213–232 (2014).
215. Götz, A. & Scharnagl, C. Dissecting conformational changes in APP's transmembrane domain linked to ε-efficiency in familial Alzheimer's disease. *PLoS One* **13**, e0200077 (2018).
216. Sato, C., Morohashi, Y., Tomita, T. & Iwatsubo, T. Structure of the catalytic pore of gamma-secretase probed by the accessibility of substituted cysteines. *J Neurosci* **26**, 12081–8 (2006).
217. Schutz, C. N. & Warshel, A. What are the dielectric 'constants' of proteins and how to validate electrostatic models? *Proteins: Structure, Function and Genetics* vol. 44 400–417 Preprint at https://doi.org/10.1002/prot.1106 (2001).

218. Tolia, A., Chávez-Gutiérrez, L. & De Strooper, B. Contribution of Presenilin Transmembrane Domains 6 and 7 to a Water-containing Cavity in the γ-Secretase Complex. *Journal of Biological Chemistry* **281**, 27633–27642 (2006).
219. Buck, M. Trifluoroethanol and colleagues: cosolvents come of age. Recent studies with peptides and proteins. *Q Rev Biophys* **31**, 297–355 (1998).
220. Götz, A. *et al.* Modulating Hinge Flexibility in the APP Transmembrane Domain Alters γ-Secretase Cleavage. *Biophys J* **116**, 2103–2120 (2019).
221. Steiner, H., Fukumori, A., Tagami, S. & Okochi, M. Making the final cut: Pathogenic amyloid-β peptide generation by γ-secretase. *Cell Stress* **2**, 292–310 (2018).
222. Götz, A. *et al.* Increased H-Bond Stability Relates to Altered ε-Cleavage Efficiency and Aβ Levels in the I45T Familial Alzheimer's Disease Mutant of APP. *Sci Rep* **9**, 5321 (2019).
223. Hofmann, M. W. *et al.* De novo design of conformationally flexible transmembrane peptides driving membrane fusion. *Proc Natl Acad Sci U S A* **101**, 14776–14781 (2004).
224. Poschner, B. C., Quint, S., Hofmann, M. W. & Langosch, D. Sequence-specific conformational dynamics of model transmembrane domains determines their membrane fusogenic function. *J Mol Biol* **386**, 733–741 (2009).
225. Doig, A. J., Errington, N. & Iqbalsyah, T. M. Stability and Design of α-Helices. in *Protein Folding Handbook* vol. 1 247–313 (2008).
226. Nick Pace, C. & Martin Scholtz, J. A Helix Propensity Scale Based on Experimental Studies of Peptides and Proteins. *Biophys J* **75**, 422–427 (1998).
227. Werner, N. T. *et al.* Cooperation of N- and C-terminal substrate transmembrane domain segments in intramembrane proteolysis by γ-secretase. *Commun Biol* **6**, 177 (2023).
228. Liu, L. P. & Deber, C. M. Uncoupling hydrophobicity and helicity in transmembrane segments. α- helical propensities of the amino acids in non-polar environments. *Journal of Biological Chemistry* **273**, 23645–23648 (1998).
229. Li, S. C. & Deber, C. M. A measure of helical propensity for amino acids in membrane environments. *Nat Struct Biol* **1**, 368–373 (1994).
230. Langelaan, D. N., Wieczorek, M., Blouin, C. & Rainey, J. K. Improved helix and kink characterization in membrane proteins allows evaluation of kink sequence predictors. *J Chem Inf Model* **50**, 2213–2220 (2010).
231. Kneissl, B., Mueller, S. C., Tautermann, C. S. & Hildebrandt, A. String kernels and high-quality data set for improved prediction of kinked helices in α-helical membrane proteins. *J Chem Inf Model* **51**, 3017–3025 (2011).
232. Hall, S. E., Roberts, K. & Vaidehi, N. Position of helical kinks in membrane protein crystal structures and the accuracy of computational prediction. *J Mol Graph Model* **27**, 944–950 (2009).
233. Meruelo, A. D., Samish, I. & Bowie, J. U. TMKink: A method to predict transmembrane helix kinks. *Protein Science* **20**, 1256–1264 (2011).
234. Shelar, A. & Bansal, M. Helix perturbations in membrane proteins assist in inter-helical interactions and optimal helix positioning in the bilayer. *Biochim Biophys Acta Biomembr* **1858**, 2804–2817 (2016).
235. Richardson, J. S. The Anatomy and Taxonomy of Protein Structure. *Adv Protein Chem* **34**, 167–339 (1981).
236. Cordes, F. S., Bright, J. N. & Sansom, M. S. P. Proline-induced distortions of transmembrane helices. *J Mol Biol* **323**, 951–960 (2002).
237. S.P. Sansom, M. & Weinstein, H. Hinges, swivels and switches: the role of prolines in signalling via transmembrane α-helices. *Trends Pharmacol Sci* **21**, 445–451 (2000).

238. Ma, B. & Nussinov, R. Enzyme dynamics point to stepwise conformational selection in catalysis. *Curr Opin Chem Biol* **14**, 652–659 (2010).
239. Silber, M., Hitzenberger, M., Zacharias, M. & Muhle-Goll, C. Altered Hinge Conformations in APP Transmembrane Helix Mutants May Affect Enzyme–Substrate Interactions of γ-Secretase. *ACS Chem Neurosci* **11**, 4426–4433 (2020).
240. Hitzenberger, M. & Zacharias, M. Structural Modeling of γ-Secretase Aβn Complex Formation and Substrate Processing. *ACS Chem Neurosci* **10**, 1826–1840 (2019).
241. Deatherage, C. L. *et al.* Structural and biochemical differences between the Notch and the amyloid precursor protein transmembrane domains. *Sci Adv* **3**, (2017).
242. Spitz, C. *et al.* Non-canonical Shedding of TNFα by SPPL2a Is Determined by the Conformational Flexibility of Its Transmembrane Helix. *iScience* **23**, 101775 (2020).
243. Esselens, C. *et al.* Presenilin 1 mediates the turnover of telencephalin in hippocampal neurons via an autophagic degradative pathway. *Journal of Cell Biology* **166**, 1041–1054 (2004).
244. Annaert, W. G. *et al.* Interaction with Telencephalin and the Amyloid Precursor Protein Predicts a Ring Structure for Presenilins. *Neuron* **32**, 579–589 (2001).
245. Wolfe, M. S. Unraveling the complexity of γ-secretase. *Semin Cell Dev Biol* **105**, 3–11 (2020).
246. Hitzenberger, M. *et al.* The dynamics of γ-secretase and its substrates. *Semin Cell Dev Biol* **105**, 86–101 (2020).
247. Hu, C. *et al.* Pen-2 and Presenilin are Sufficient to Catalyze Notch Processing. *Journal of Alzheimer's Disease* **56**, 1263–1269 (2017).
248. Hu, C. *et al.* Nicastrin is required for amyloid precursor protein (APP) but not Notch processing, while anterior pharynx-defective 1 is dispensable for processing of both APP and Notch. *J Neurochem* **136**, 1246–1258 (2016).
249. Dehury, B., Tang, N. & Kepp, K. P. Molecular dynamics of C99-bound γ-secretase reveal two binding modes with distinct compactness, stability, and active-site retention: implications for Aβ production. *Biochemical Journal* **476**, 1173–1189 (2019).
250. Somavarapu, A. K. & Kepp, K. P. The dynamic mechanism of presenilin-1 function: Sensitive gate dynamics and loop unplugging control protein access. *Neurobiol Dis* **89**, 147–156 (2016).
251. Kong, R., Chang, S., Xia, W. & Wong, S. T. C. Molecular dynamics simulation study reveals potential substrate entry path into γ-secretase/presenilin-1. *J Struct Biol* **191**, 120–129 (2015).
252. Petit, D. *et al.* Extracellular interface between APP and Nicastrin regulates Aβ length and response to γ-secretase modulators. *EMBO J* **38**, (2019).
253. Siegel, G. *et al.* The Alzheimer's Disease γ-Secretase Generates Higher 42:40 Ratios for β-Amyloid Than for p3 Peptides. *Cell Rep* **19**, 1967–1976 (2017).
254. Tang, T.-C. *et al.* Conformational Changes Induced by the A21G Flemish Mutation in the Amyloid Precursor Protein Lead to Increased Aβ Production. *Structure* **22**, 387–396 (2014).
255. Tian, Y., Bassit, B., Chau, D. & Li, Y.-M. An APP inhibitory domain containing the Flemish mutation residue modulates γ-secretase activity for Aβ production. *Nat Struct Mol Biol* **17**, 151–158 (2010).
256. Wilhelmsen, K. & van der Geer, P. Phorbol 12-Myristate 13-Acetate-Induced Release of the Colony-Stimulating Factor 1 Receptor Cytoplasmic Domain into the Cytosol Involves Two Separate Cleavage Events. *Mol Cell Biol* **24**, 454–464 (2004).
257. van Tetering, G. & Vooijs, M. Proteolytic Cleavage of Notch: 'HIT and RUN'. *Curr Mol Med* **11**, 255–269 (2011).

7 Appendix

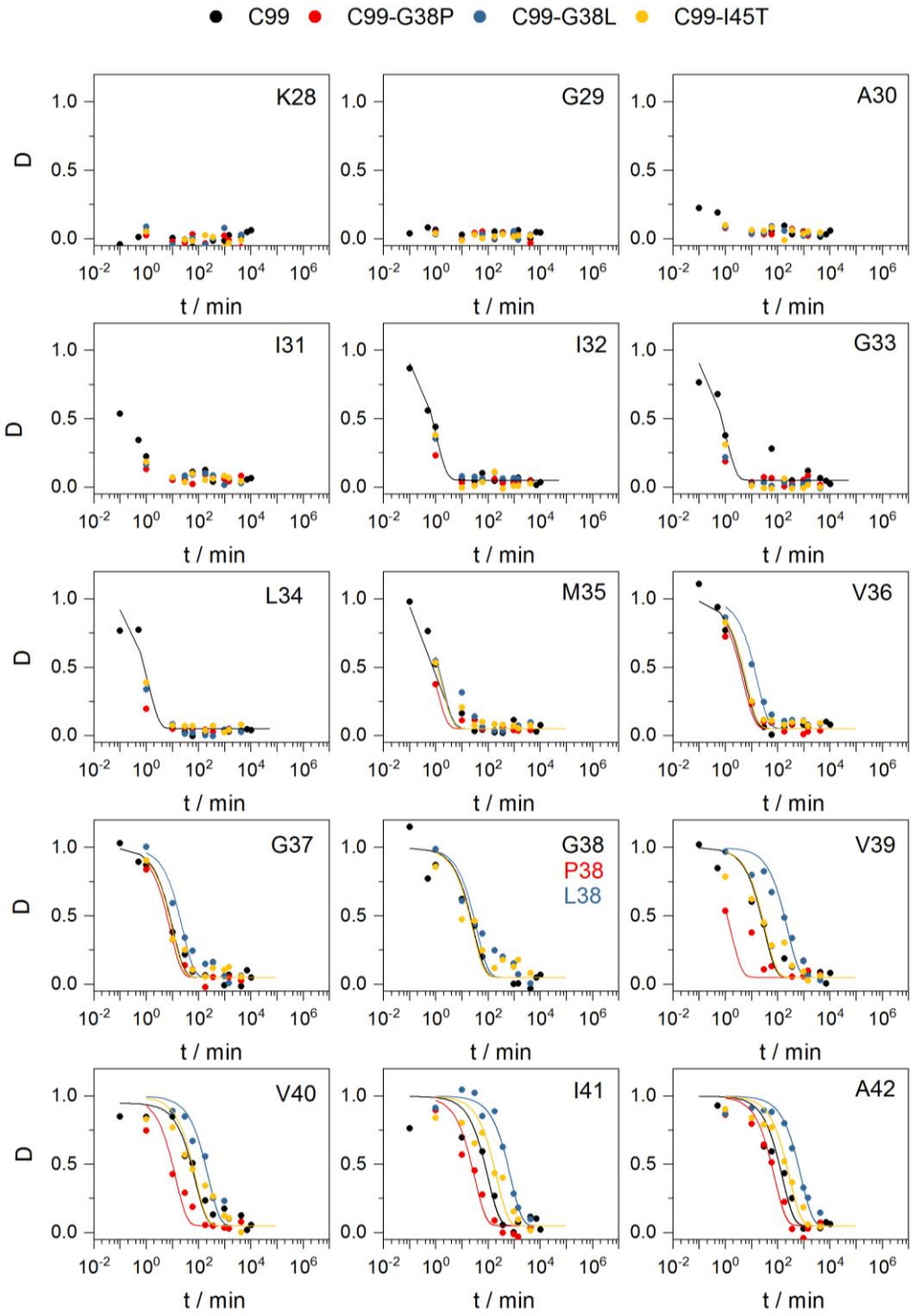
C99
C99-G38P
C99-G38L
C99-I45T
K28
G29
A30
I31
I32
G33
L34
M35
V36
G37
G38
P38
L38
V39
V40
I41
A42
D
t / min

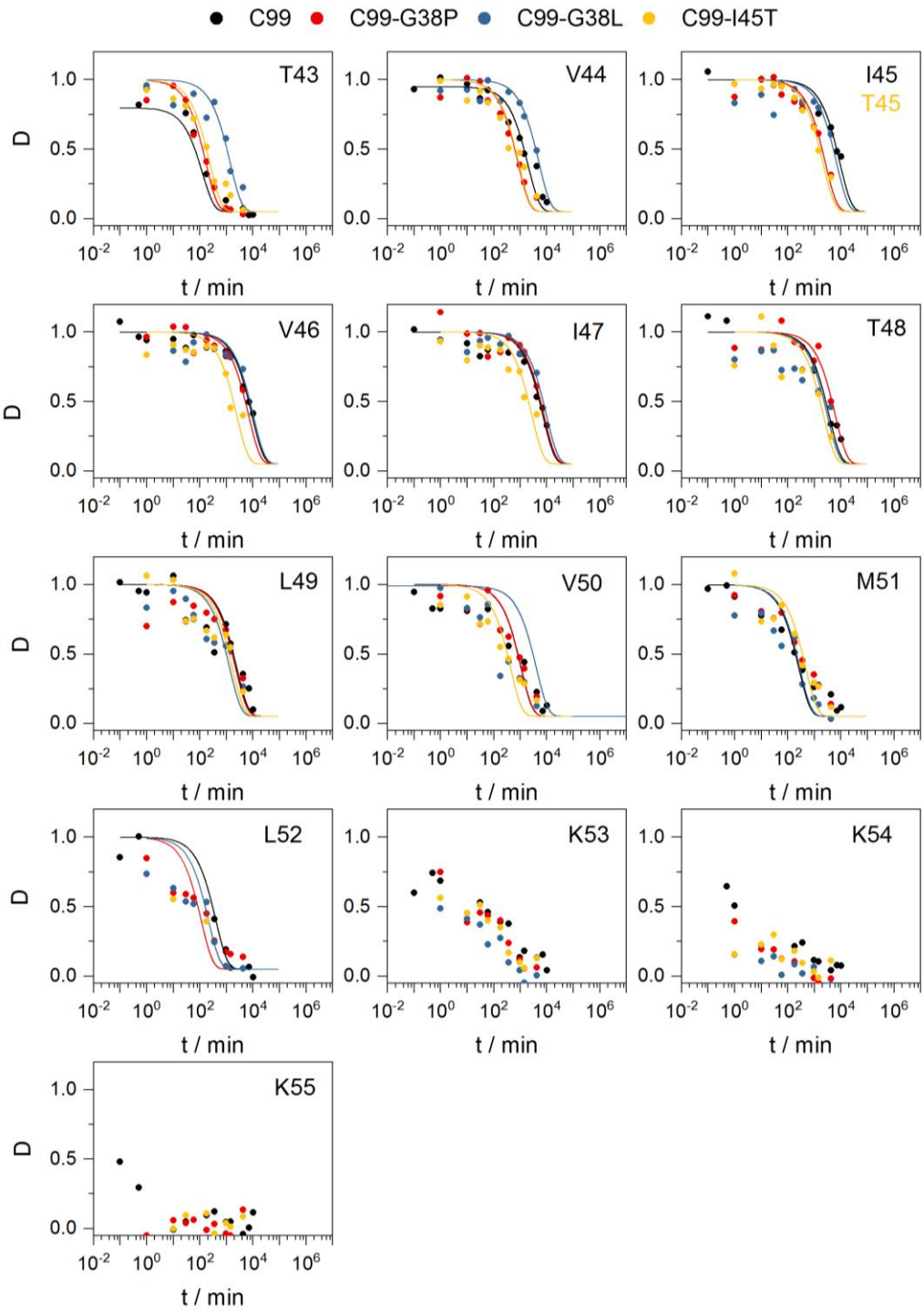

Figure S1: Residue-specific DHX kinetics obtained after ETD from $C99_{28-55}$ WT and C99 based mutants. The calculated deuterium contents D (mean values, n ≥ 3) of the respective amides are plotted against the log of the exchange period t. The identities of the $C99_{28-55}$ WT residues (in black), along with the identities of the respective mutants (color coded) are given in the insets. Exponential fits are shown for those kinetics that were complete enough for calculation of the exchange rate constants given in the results and in Table S1. In some cases, the obtained deuterium content at t = 0 (D_0) was lower than the maximum value of 1. This might be caused by too fast exchange of labile side chain deuterons or insufficient deuteration in the very rigid regions. The according fits were adjusted for the respective D_0 value to calculate correct k_{exp} values.

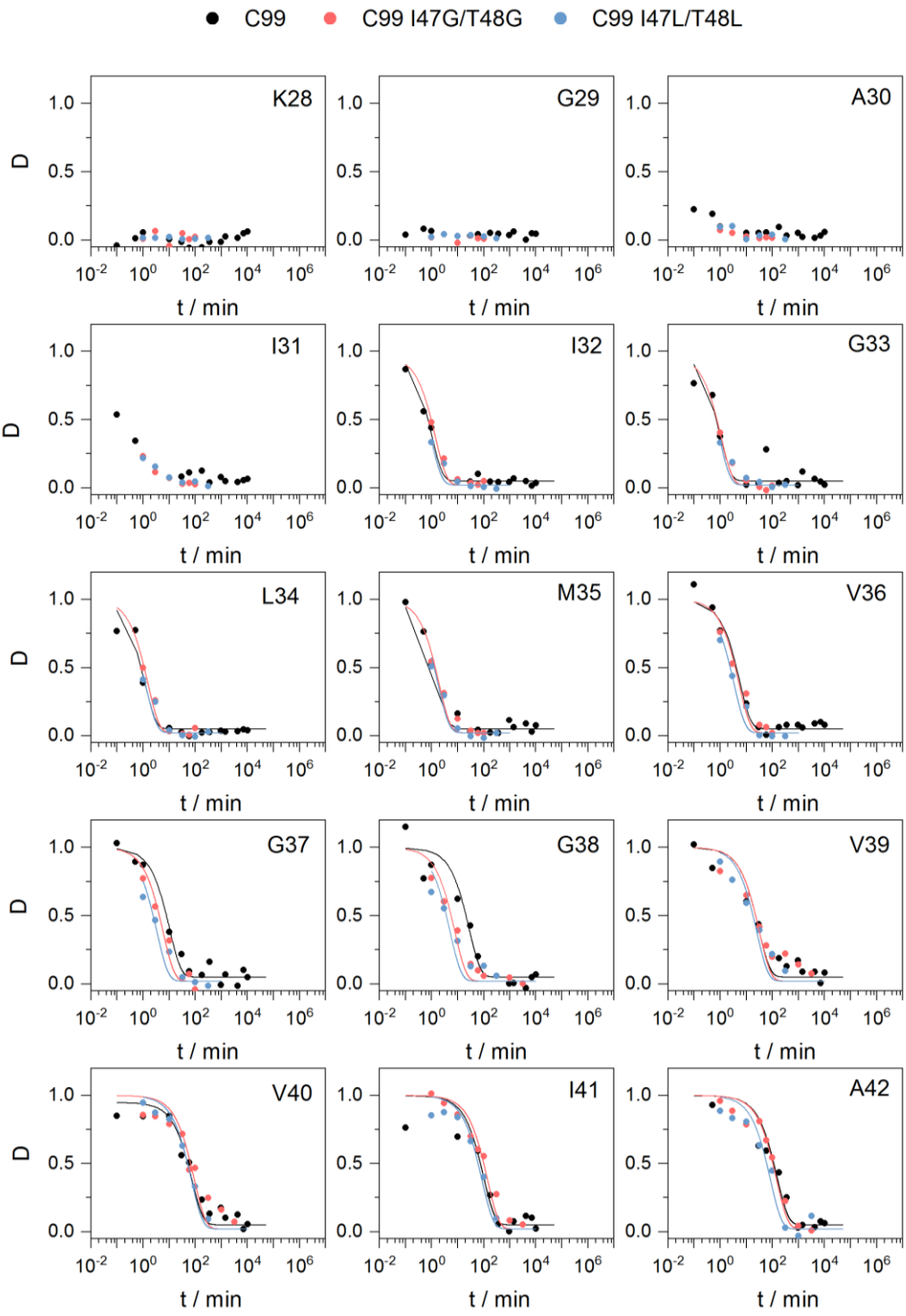
C99
C99 I47G/T48G
C99 I47L/T48L
K28
G29
A30
I31
I32
G33
L34
M35
V36
G37
G38
V39
V40
I41
A42
D
t / min
1.0
0.5
0.0
10^{-2}
10^{0}
10^{2}
10^{4}
10^{6}

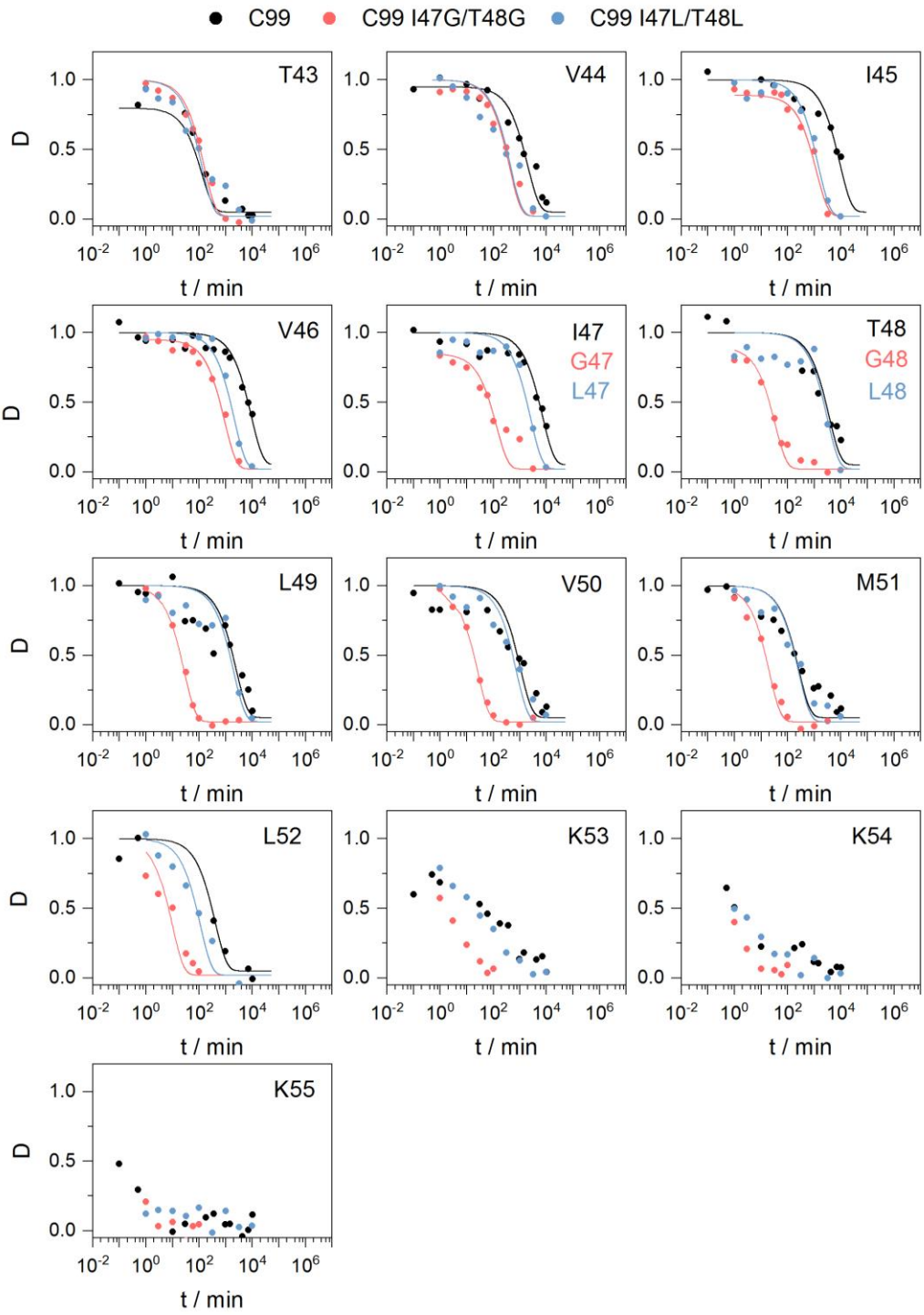

Figure S2: Residue-specific DHX kinetics obtained after ETD from $C99_{28-55}$ WT and C99 based mutants. The calculated deuterium contents D (mean values, n ≥ 3) of the respective amides are plotted against the log of the exchange period t. The identities of the $C99_{28-55}$ WT residues (in black), along with the identities of the respective mutants (color coded) are given in the insets. Exponential fits are shown for those kinetics that were complete enough for calculation of the exchange rate constants given in the results and in Table S2. In some cases, the obtained deuterium content at t = 0 (D_0) was lower than the maximum value of 1. This might be caused by too fast exchange of labile side chain deuterons or insufficient deuteration in the very rigid regions. The according fits were adjusted for the respective D_0 value to calculate correct k_{exp} values.

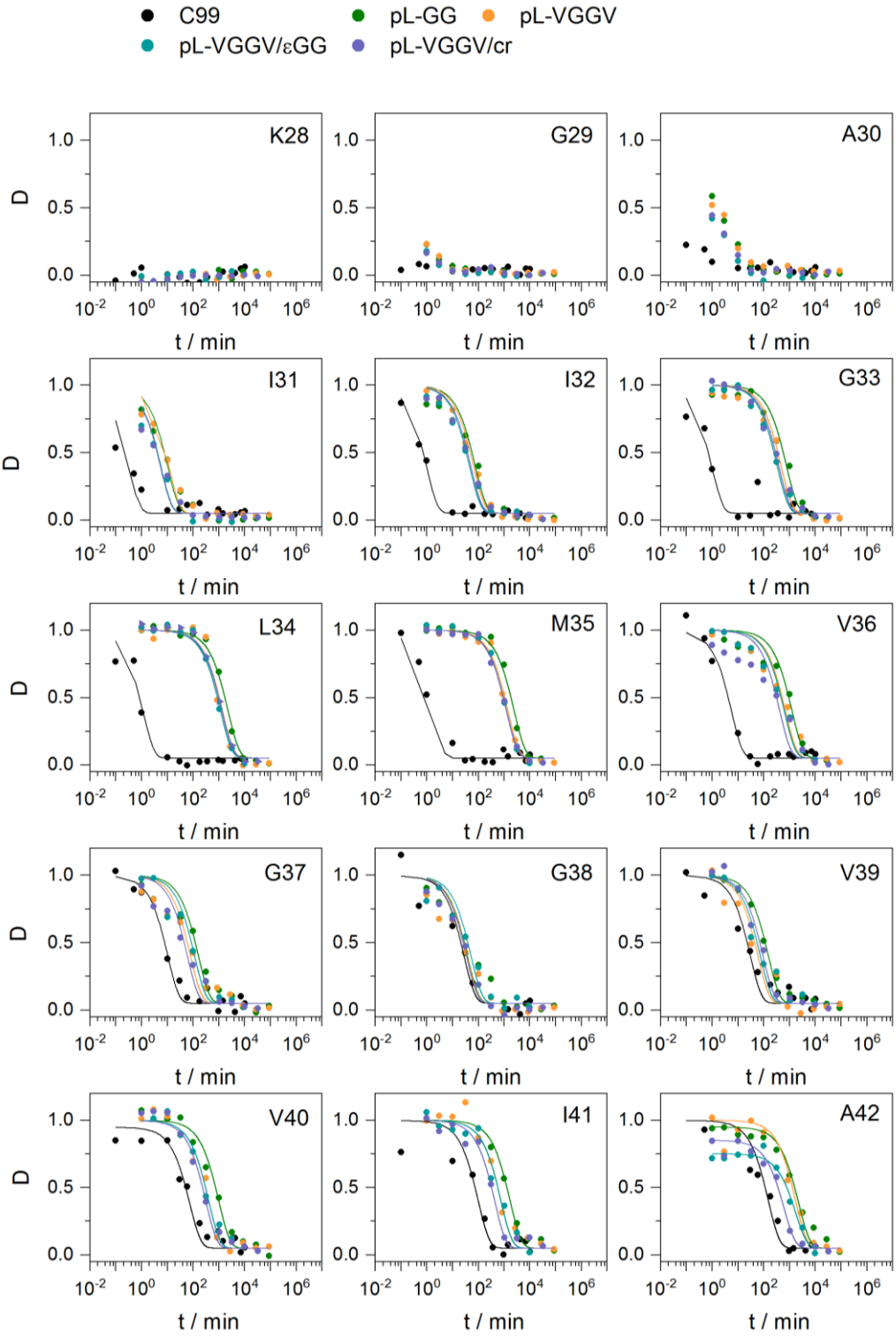
C99
pL-GG
pL-VGGV
pL-VGGV/εGG
pL-VGGV/cr
K28
G29
A30
I31
I32
G33
L34
M35
V36
G37
G38
V39
V40
I41
A42
D
t / min

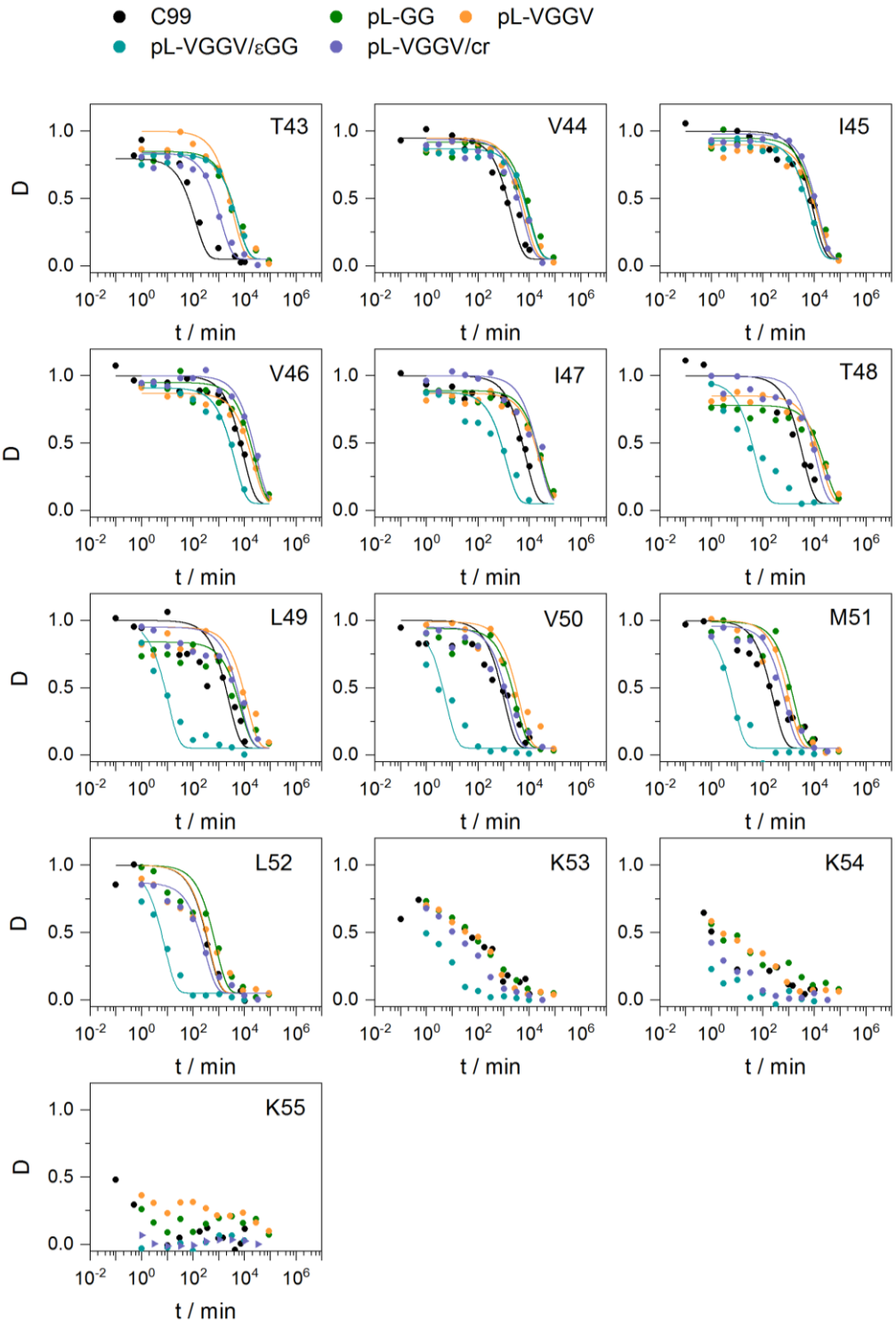

Figure S3: Residue-specific DHX kinetics obtained after ETD from $C99_{28-55}$ WT and artificial poly-Leu peptides.

The calculated deuterium contents D (mean values, n ≥ 3) of the respective amides are plotted against the log of the exchange period t. As reference, the identities of the $C99_{28-55}$ WT residues are given in the insets. Exponential fits are shown for those kinetics that were complete enough for calculation of the exchange rate constants given in the results and in Table S2. In some cases, the obtained deuterium content at t = 0 (D_0) was lower than the maximum value of 1. This might be caused by too fast exchange of the labile side chain deuterons or insufficient deuteration in the very rigid regions. The according fits were adjusted for the respective D_0 value to calculate correct k_{exp} values.

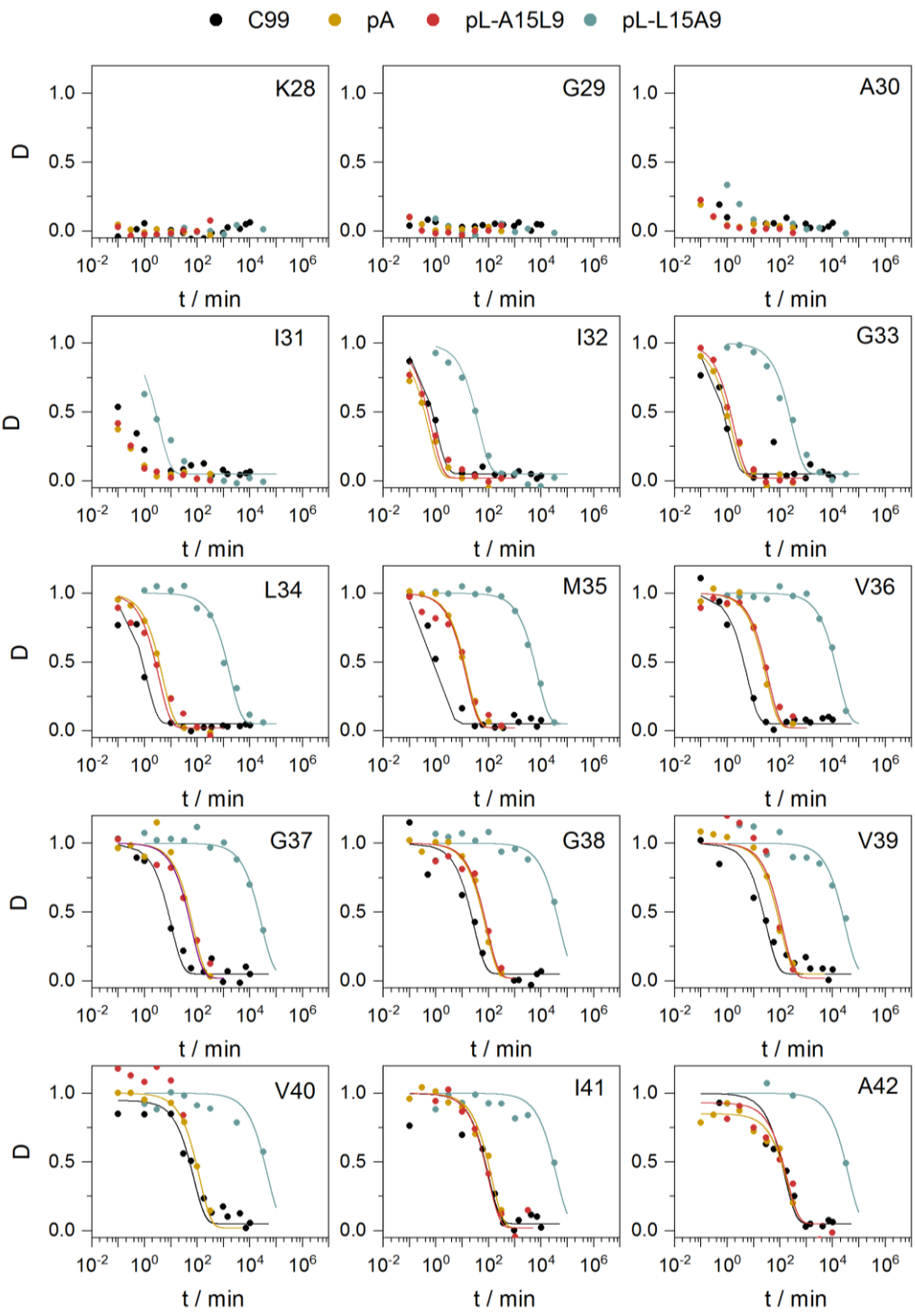
C99
pA
pL-A15L9
pL-L15A9
K28
G29
A30
I31
I32
G33
L34
M35
V36
G37
G38
V39
V40
I41
A42
D
t / min

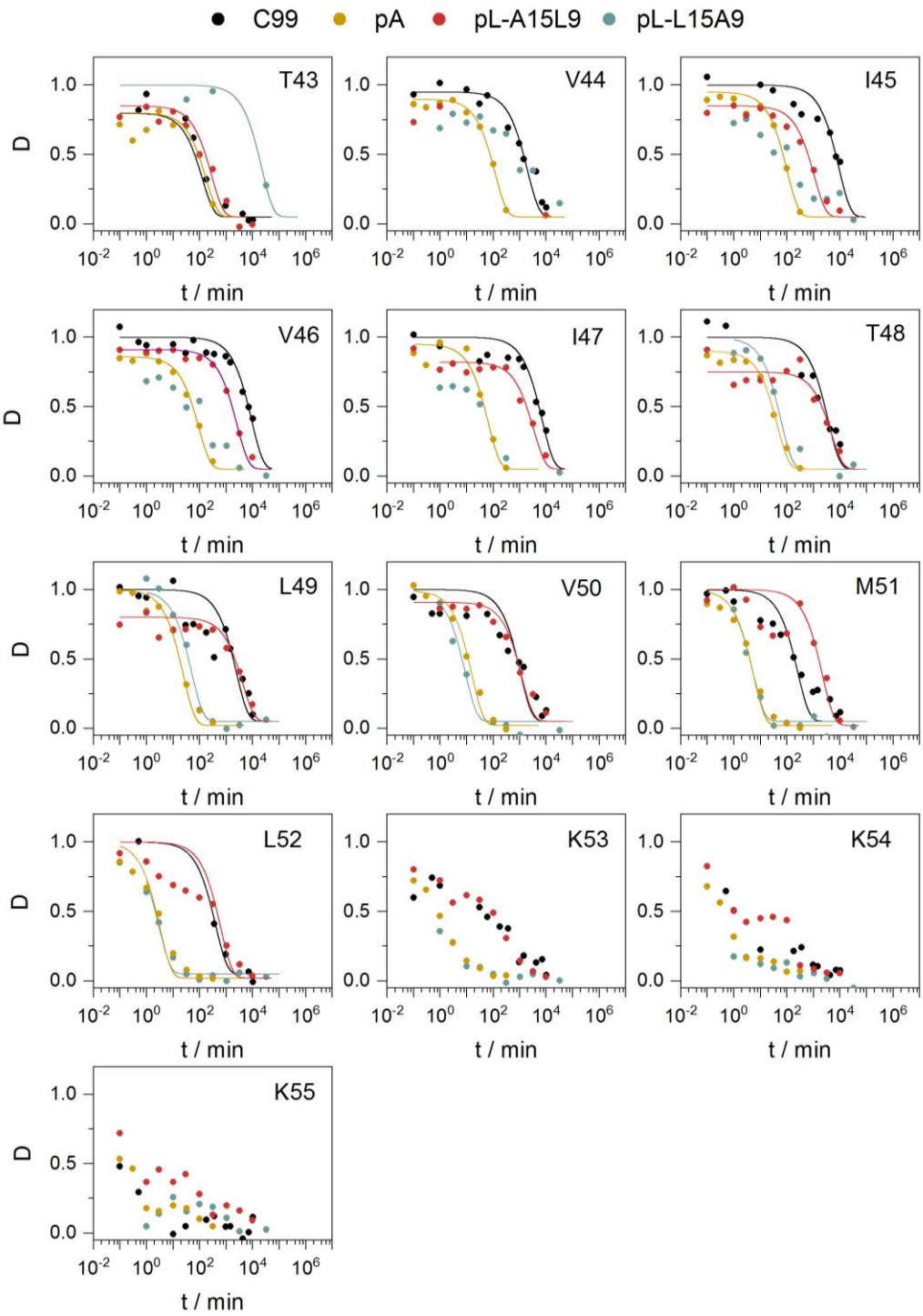

Figure S4: Residue-specific DHX kinetics obtained after ETD artificial poly-Leu and poly-Ala constructs. The calculated deuterium contents D (mean values, n ≥ 3) of the respective amides are plotted against the log of the exchange period t. As reference, the identities of the $C99_{28\text{-}55}$ WT residues are given in the insets. Exponential fits are shown for those kinetics that were complete enough for calculation of the exchange rate constants given in the results and in Table S2. In some cases, the obtained deuterium content at t = 0 (D_0) was lower than the maximum value of 1. This might be caused by too fast exchange of the labile side chain deuterons or insufficient deuteration in the very rigid regions. The according fits were adjusted for the respective D_0 value to calculate correct k_{exp} values.

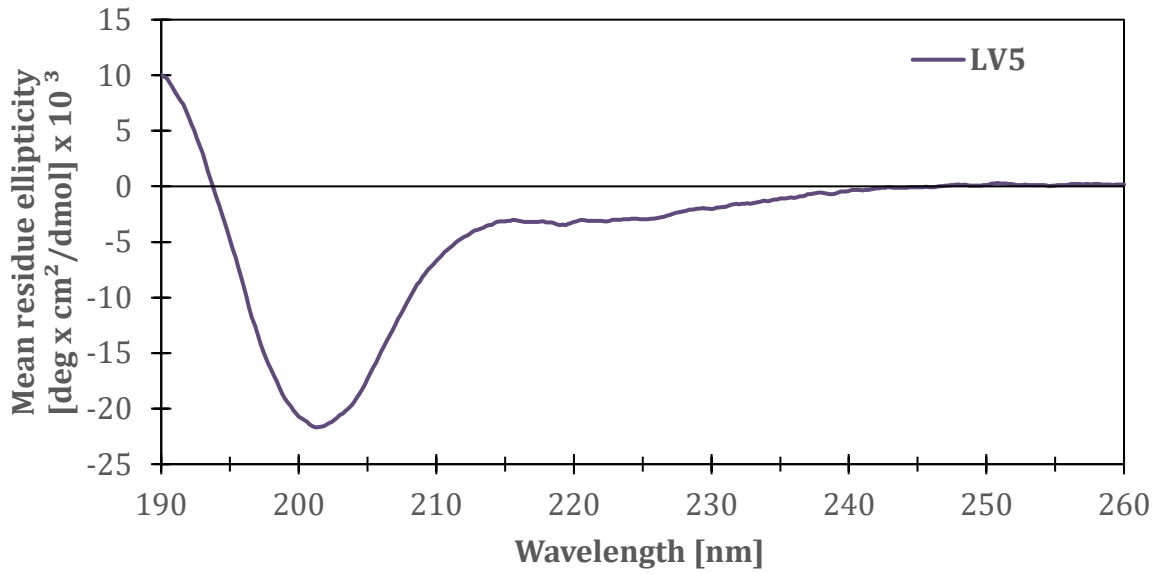

Figure S5: CD-Spectrum of LV5.

LV5 dissolved in 80% TFE/H_2O (n = 3, SDs smaller than the respective icons). Spectrum indicates an unfolded structure.

Table S1: Numerical values of k_{exp} and ΔG of $C99_{28-55}$ WT.

k_{exp} is from exponential fit of means ± SE. For exponential fits see Figure S1.
ΔG is listed with the confidence interval, based on the respective k_{exp} SEMs.
n.d. = not determined, as data points were not sufficient.

	$C99_{28-55}$ WT		
amide	**log k_{exp} [min^{-1}]**	**log k_{ch} [min^{-1}]**	**ΔG**
K	n.d.	0.88	n.d.
G	n.d.	1.19	n.d.
A	n.d.	0.97	n.d.
I	n.d.	0.08	n.d.
I	0.02 ± 0.03	-0.15	n.d.
G	0.02 ± 0.08	0.84	1.00 ± 0.13
L	-0.05 ± 0.06	0.39	0.34 ± 0.11
M	-0.19 ± 0.05	0.58	0.93 ± 0.09
V	-0.75 ± 0.08	0.21	1.23 ± 0.12
G	-1.02 ± 0.09	0.93	2.61 ± 0.12
G	-1.45 ± 0.08	1.24	3.60 ± 0.10
V	-1.49 ± 0.11	0.27	2.35 ± 0.14
V	-1.87 ± 0.13	-0.03	2.46 ± 0.17
I	-2.00 ± 0.14	-0.06	2.59 ± 0.18
A	-2.19 ± 0.11	0.57	3.69 ± 0.15
T	-2.11 ± 0.08	0.73	3.80 ± 0.10
V	-3.31 ± 0.13	0.30	4.84 ± 0.18
I	-3.97 ± 0.10	-0.06	5.24 ± 0.14
V	-3.97 ± 0.11	-0.12	5.16 ± 0.15
I	-3.86 ± 0.14	-0.06	5.09 ± 0.18
T	-3.56 ± 0.26	0.50	5.45 ± 0.35
L	-3.40 ± 0.27	0.42	5.12 ± 0.36
V	-3.04 ± 0.17	-0.10	3.94 ± 0.23
M	-2.42 ± 0.19	0.65	4.11 ± 0.25
L	-2.61 ± 0.09	0.33	3.95 ± 0.12
K	n.d.	0.55	n.d.
K	n.d.	0.88	n.d.
K	n.d.	0.88	n.d.

Table S2: Numerical values of k_{exp} and ΔG of G38L.

k_{exp} is from exponential fit of means ± SE. For exponential fits see Figure S1.
ΔG is listed with the confidence interval, based on the respective k_{exp} SEMs.
n.d. = not determined, as data points were not sufficient.

	G38L		
amide	**log k_{exp} [min^{-1}]**	**log k_{ch} [min^{-1}]**	**ΔG**
K	n.d.	0.88	n.d.
G	n.d.	1.19	n.d.
A	n.d.	0.97	n.d.
I	n.d.	0.08	n.d.
I	n.d.	-0.15	n.d.
G	0.24 ± 0.05	0.84	0.64 ± 0.09
L	0.07 ± 0.04	0.39	0.05 ± 0.11
M	-0.23 ± 0.51	0.58	0.99 ± 0.98
V	-1.22 ± 0.07	0.21	1.90 ± 0.10
G	-1.39 ± 0.08	0.93	3.11 ± 0.11
L	-1.57 ± 0.16	0.39	2.62 ± 0.21
V	-2.38 ± 0.10	-0.10	3.06 ± 0.13
V	-2.38 ± 0.16	-0.03	3.14 ± 0.22
I	-2.87 ± 0.05	-0.06	3.77 ± 0.07
A	-2.90 ± 0.12	0.57	4.66 ± 0.16
T	-3.15 ± 0.24	0.73	5.20 ± 0.33
V	-3.72 ± 0.08	0.30	5.39 ± 0.11
I	-3.84 ± 0.17	-0.06	5.07 ± 0.23
V	-4.02 ± 0.19	-0.12	5.23 ± 0.26
I	-4.00 ± 0.15	-0.06	5.28 ± 0.20
T	n.d.	0.50	n.d.
L	-3.49 ± 0.38	0.42	5.25 ± 0.51
V	-3.13 ± 0.55	-0.10	4.06 ± 0.73
M	-2.46 ± 0.23	0.65	4.17 ± 0.31
L	-2.33 ± 0.20	0.33	3.57 ± 0.27
K	n.d.	0.55	n.d.
K	n.d.	0.88	n.d.
K	n.d.	0.88	n.d.

Table S3: Numerical values of k_{exp} and ΔG of G38P.

k_{exp} is from exponential fit of means ± SE. For exponential fits see Figure S1.
ΔG is listed with the confidence interval, based on the respective k_{exp} SEMs.
n.d. = not determined, as data points were not sufficient.

	G38P		
amide	**log k_{exp} [min^{-1}]**	**log k_{ch} [min^{-1}]**	**ΔG**
K	n.d.	0.88	n.d.
G	n.d.	1.19	n.d.
A	n.d.	0.97	n.d.
I	n.d.	0.08	n.d.
I	n.d.	-0.15	n.d.
G	0.28 ± 0.05	0.84	0.57 ± 0.08
L	0.27 ± 0.02	0.39	n.d.
M	0.04 ± 0.05	0.58	0.54 ± 0.09
V	-0.68 ± 0.12	0.21	1.11 ± 0.12
G	-0.91 ± 0.06	0.93	2.46 ± 0.12
P	n.d.	n.d.	n.d.
V	-0.19 ± 0.62	-0.13	0 ± 0,77
V	-1.12 ± 0.20	-0.03	1.41 ± 0.28
I	-1.49 ± 0.10	-0.06	1.89 ± 0.14
A	-1.89 ± 0.08	0.57	3.29 ± 0.11
T	-2.24 ± 0.07	0.73	3.97 ± 0.09
V	-2.93 ± 0.10	0.30	4.33 ± 0.13
I	-3.42 ± 0.10	-0.06	4.50 ± 0.13
V	-3.84 ± 0.08	-0.12	4.99 ± 0.11
I	-3.91 ± 0.12	-0.06	5.15 ± 0.17
T	-3.80 ± 0.23	0.50	5.76 ± 0.31
L	-3.35 ± 0.28	0.42	5.06 ± 0.37
V	-3.05 ± 0.35	-0.10	3.95 ± 0.47
M	-2.68 ± 0.20	0.65	4.47 ± 0.27
L	-2.06 ± 0.38	0.33	3.20 ± 0.52
K	n.d.	0.55	n.d.
K	n.d.	0.88	n.d.
K	n.d.	0.88	n.d.

Table S4: Numerical values of k_{exp} and ΔG of I45T.

k_{exp} is from exponential fit of means ± SE. For exponential fits see Figure S1.
ΔG is listed with the confidence interval, based on the respective k_{exp} SEMs.
n.d. = not determined, as data points were not sufficient.

	I45T		
amide	**log k_{exp} [min^{-1}]**	**log k_{ch} [min^{-1}]**	**ΔG**
K	n.d.	0.88	n.d.
G	n.d.	1.19	n.d.
A	n.d.	0.97	n.d.
I	n.d.	0.08	n.d.
I	n.d.	-0.15	n.d.
G	0.14 ± 0.06	0.84	0.81 ± 0.10
L	-0.05 ± 0.03	0.39	0.34 ± 0.06
M	-0.25 ± 0.07	0.58	1.02 ± 0.11
V	-0.81 ± 0.06	0.21	1.32 ± 0.09
G	-0.98 ± 0.10	0.93	2.56 ± 0.14
G	-1.45 ± 0.15	1.24	3.60 ± 0.21
V	-1.49 ± 0.11	0.27	2.35 ± 0.15
V	-1.91 ± 0.22	-0.03	2.51 ± 0.29
I	-2.42 ± 0.10	-0.06	3.16 ± 0.13
A	-2.46 ± 0.07	0.57	4.07 ± 0.10
T	-2.38 ± 0.09	0.73	4.17 ± 0.12
V	-2.98 ± 0.12	0.30	4.40 ± 0.16
I	-3.35 ± 0.06	0.59	5.28 ± 0.08
V	-3.54 ± 0.31	0.30	5.15 ± 0.42
I	-3.63 ± 0.36	-0.06	4.78 ± 0.48
T	-3.45 ± 0.25	0.50	5.29 ± 0.33
L	-3.27 ± 0.22	0.42	4.95 ± 0.30
V	-2.57 ± 0.14	-0.10	3.32 ± 0.19
M	-2.70 ± 0.11	0.65	4.49 ± 0.14
L	n.d.	0.33	n.d.
K	n.d.	0.55	n.d.
K	n.d.	0.88	n.d.
K	n.d.	0.88	n.d.

Table S5: Numerical values of k_{exp} and ΔG of I47L/T48L.

k_{exp} is from exponential fit of means ± SE. For exponential fits see Figure S2.
ΔG is listed with the confidence interval, based on the respective k_{exp} SEMs.
n.d. = not determined, as data points were not sufficient.

	I47LT48L		
amide	**log k_{exp} [min^{-1}]**	**log k_{ch} [min^{-1}]**	**ΔG**
K	n.d.	0.88	n.d.
G	n.d.	1.19	n.d.
A	n.d.	0.97	n.d.
I	n.d.	0.08	n.d.
I	n.d.	-0.15	n.d.
G	0.04 ± 0.08	0.84	0.97 ± 0.12
L	-0.09 ± 0.09	0.39	0.42 ± 0.18
M	-0.25 ± 0.07	0.58	1.01 ± 0.10
V	-0.54 ± 0.08	0.21	0.89 ± 0.13
G	-0.54 ± 0.13	0.93	1.95 ± 0.18
G	-0.71 ± 0.16	1.24	2.61 ± 0.21
V	-1.41 ± 0.17	0.27	2.24 ± 0.23
V	-1.86 ± 0.17	-0.03	2.44 ± 0.23
I	-1.93 ± 0.24	-0.06	2.50 ± 0.33
A	-1.93 ± 0.11	0.57	3.35 ± 0.15
T	-2.11 ± 0.20	0.73	3.80 ± 0.26
V	-2.65 ± 0.28	0.30	3.96 ± 0.38
I	-3.16 ± 0.10	-0.06	4.16 ± 0.14
V	-3.33 ± 0.26	-0.12	4.30 ± 0.35
L	-3.42 ± 0.17	0.09	4.70 ± 0.23
L	-3.50 ± 0.17	0.02	4.72 ± 0.23
L	-3.31 ± 0.22	0.02	4.46 ± 0.29
V	-2.88 ± 0.16	-0.10	3.73 ± 0.22
M	-2.42 ± 0.12	0.65	4.11 ± 0.16
L	-2.05 ± 0.19	0.33	3.19 ± 0.25
K	n.d.	0.55	n.d.
K	n.d.	0.88	n.d.
K	n.d.	0.88	n.d.

Table S6: Numerical values of k_{exp} and ΔG of I47G/T48G.

k_{exp} is from exponential fit of means ± SE. For exponential fits see Figure S2.
ΔG is listed with the confidence interval, based on the respective k_{exp} SEMs.
n.d. = not determined, as data points were not sufficient.

	I47GT48G		
amide	**log k_{exp} [min^{-1}]**	**log k_{ch} [min^{-1}]**	**ΔG**
K	n.d.	0.88	n.d.
G	n.d.	1.19	n.d.
A	n.d.	0.97	n.d.
I	n.d.	0.08	n.d.
I	n.d.	-0.15	n.d.
G	-0.05 ± 0.07	0.84	1.10 ± 0.10
L	-0.19 ± 0.06	0.39	0.61 ± 0.10
M	-0.29 ± 0.07	0.58	1.08 ± 0.10
V	-0.73 ± 0.09	0.21	1.19 ± 0.14
G	-0.77 ± 0.10	0.93	2.27 ± 0.13
G	-0.90 ± 0.10	1.24	2.86 ± 0.13
V	-1.51 ± 0.13	0.27	2.38 ± 0.17
V	-1.97 ± 0.12	-0.03	2.59 ± 0.16
I	-2.15 ± 0.08	-0.06	2.79 ± 0.11
A	-2.17 ± 0.07	0.57	3.67 ± 0.09
T	-2.19 ± 0.06	0.73	3.91 ± 0.08
V	-2.61 ± 0.18	0.30	3.90 ± 0.24
I	-3.09 ± 0.33	-0.06	4.06 ± 0.44
V	-2.97 ± 0.29	-0.12	3.82 ± 0.38
G	-2.13 ± 0.14	0.93	4.10 ± 0.19
G	-1.53 ± 0.06	1.24	3.71 ± 0.08
L	-1.45 ± 0.03	0.39	2.46 ± 0.04
V	-1.41 ± 0.03	-0.10	1.73 ± 0.04
M	-1.31 ± 0.06	0.65	2.63 ± 0.09
L	-0.99 ± 0.17	0.33	1.75 ± 0.24
K	n.d.	0.55	n.d.
K	n.d.	0.88	n.d.
K	n.d.	0.88	n.d.

Table S7: Numerical values of k_{exp} and ΔG of pL-GG.

k_{exp} is from exponential fit of means ± SE. For exponential fits see Figure S3.
ΔG is listed with the confidence interval, based on the respective k_{exp} SEMs.
n.d. = not determined, as data points were not sufficient.

	pL-GG		
amide	**log k_{exp} [min^{-1}]**	**log k_{ch} [min^{-1}]**	**ΔG**
K	n.d.	0.88	n.d.
L	n.d.	0.34	n.d.
L	n.d.	0.02	n.d.
L	-1.01 ± 0.09	0.02	1.32 ± 0.14
L	-1.88 ± 0.11	0.02	2.54 ± 0.15
L	-2.89 ± 0.07	0.02	3.90 ± 0.10
L	-3.36 ± 0.03	0.02	4.53 ± 0.04
L	-3.40 ± 0.03	0.02	4.59 ± 0.04
L	-3.10 ± 0.09	0.02	4.19 ± 0.12
G	-2.21 ± 0.17	0.86	4.12 ± 0.23
G	-1.58 ± 0.17	1.24	3.78 ± 0.22
L	-2.19 ± 0.05	0.39	3.46 ± 0.07
L	-2.99 ± 0.08	0.02	4.03 ± 0.11
L	-3.24 ± 0.06	0.02	4.37 ± 0.08
L	-3.36 ± 0.08	0.02	4.53 ± 0.11
L	-3.72 ± 0.07	0.02	5.01 ± 0.10
L	-4.01 ± 0.15	0.02	5.41 ± 0.21
L	-4.11 ± 0.21	0.02	5.54 ± 0.28
L	-4.39 ± 0.31	0.02	5.91 ± 0.41
L	-4.48 ± 0.34	0.02	6.03 ± 0.46
L	-4.43 ± 0.26	0.02	5.97 ± 0.35
L	-3.86 ± 0.11	0.02	5.20 ± 0.15
L	-3.50 ± 0.07	0.02	4.72 ± 0.09
L	-3.22 ± 0.07	0.02	4.34 ± 0.09
L	-2.89 ± 0.17	0.02	3.90 ± 0.23
K	n.d.	0.55	n.d.
K	n.d.	0.88	n.d.
K	n.d.	0.88	n.d.

Table S8: Numerical values of k_{exp} and ΔG of pL-VGGV.

k_{exp} is from exponential fit of means ± SE. For exponential fits see Figure S3.
ΔG is listed with the confidence interval, based on the respective k_{exp} SEMs.
n.d. = not determined, as data points were not sufficient.

	pL-VGGV		
amide	**log k_{exp} [min^{-1}]**	**log k_{ch} [min^{-1}]**	**ΔG**
K	n.d.	0.88	n.d.
L	n.d.	0.34	n.d.
L	n.d.	0.02	n.d.
L	-1.05 ± 0.09	0.02	1.38 ± 0.13
L	-1.82 ± 0.06	0.02	2.45 ± 0.08
L	-2.68 ± 0.07	0.02	3.61 ± 0.09
L	-3.15 ± 0.05	0.02	4.24 ± 0.07
L	-3.16 ± 0.03	0.02	4.26 ± 0.05
V	-2.85 ± 0.12	-0.10	3.68 ± 0.16
G	-1.91 ± 0.14	0.93	3.80 ± 0.19
G	-1.56 ± 0.12	1.24	3.75 ± 0.17
V	-1.78 ± 0.15	0.27	2.75 ± 0.20
L	-2.61 ± 0.05	0.09	3.62 ± 0.07
L	-2.89 ± 0.06	0.02	3.90 ± 0.08
L	-3.24 ± 0.06	0.02	4.37 ± 0.08
L	-3.55 ± 0.13	0.02	4.78 ± 0.18
L	-3.84 ± 0.11	0.02	5.17 ± 0.14
L	-4.13 ± 0.21	0.02	5.57 ± 0.28
L	-4.34 ± 0.21	0.02	5.84 ± 0.28
L	-4.43 ± 0.28	0.02	5.97 ± 0.38
L	-4.29 ± 0.45	0.02	5.77 ± 0.60
L	-4.10 ± 0.33	0.02	5.52 ± 0.44
L	-3.62 ± 0.13	0.02	4.88 ± 0.18
L	-3.03 ± 0.07	0.02	4.09 ± 0.10
L	-2.63 ± 0.33	0.02	3.55 ± 0.44
K	n.d.	0.55	n.d.
K	n.d.	0.88	n.d.
K	n.d.	0.88	n.d.

Table S9: Numerical values of k_{exp} and ΔG of pL-VGGV-cr.

k_{exp} is from exponential fit of means ± SE. For exponential fits see Figure S3.
ΔG is listed with the confidence interval, based on the respective k_{exp} SEMs.
n.d. = not determined, as data points were not sufficient.

	pL-VGGV-cr		
amide	**log k_{exp} [min^{-1}]**	**log k_{ch} [min^{-1}]**	**ΔG**
K	n.d.	0.88	n.d.
L	n.d.	0.34	n.d.
L	n.d.	0.02	n.d.
L	-0.73 ± 0.12	0.02	0.88 ± 0.19
L	-1.71 ± 0.07	0.02	2.30 ± 0.10
L	-2.59 ± 0.07	0.02	3.50 ± 0.10
L	-3.13 ± 0.03	0.02	4.22 ± 0.04
L	-3.10 ± 0.02	0.02	4.18 ± 0.03
V	-2.63 ± 0.32	-0.10	3.39 ± 0.43
G	-1.78 ± 0.14	0.93	3.64 ± 0.19
G	-1.54 ± 0.10	1.24	3.72 ± 0.14
V	-1.98 ± 0.06	0.27	3.01 ± 0.08
L	-2.49 ± 0.07	0.09	3.46 ± 0.09
L	-2.64 ± 0.07	0.02	3.56 ± 0.09
L	-2.79 ± 0.04	0.02	3.77 ± 0.05
L	-3.08 ± 0.08	0.02	4.16 ± 0.10
V	-3.75 ± 0.38	-0.10	4.89 ± 0.51
I	-4.16 ± 0.05	-0.06	5.49 ± 0.06
V	-4.46 ± 0.09	-0.12	5.82 ± 0.13
I	-4.39 ± 0.37	-0.06	5.80 ± 0.50
T	-4.05 ± 0.48	0.50	6.10 ± 0.64
L	-3.86 ± 0.55	0.42	5.74 ± 0.74
V	-3.21 ± 0.14	-0.10	4.17 ± 0.19
M	-2.87 ± 0.07	0.65	4.72 ± 0.10
L	-2.47 ± 0.09	0.33	3.76 ± 0.12
K	n.d.	0.55	n.d.
K	n.d.	0.88	n.d.
K	n.d.	0.88	n.d.

Table S10: Numerical values of k_{exp} and ΔG of pL-εGG.

k_{exp} is from exponential fit of means ± SE. For exponential fits see Figure S3.
ΔG is listed with the confidence interval, based on the respective k_{exp} SEMs.
n.d. = not determined, as data points were not sufficient.

	pL-εGG		
amide	**log k_{exp} [min^{-1}]**	**log k_{ch} [min^{-1}]**	**ΔG**
K	n.d.	0.92	n.d.
L	n.d.	0.38	n.d.
L	n.d.	0.05	n.d.
L	-0.75 ± 0.10	0.05	0.97 ± 0.15
L	-1.66 ± 0.08	0.05	2.28 ± 0.11
L	-2.53 ± 0.06	0.05	3.46 ± 0.08
L	-3.07 ± 0.04	0.05	4.19 ± 0.05
L	-3.10 ± 0.04	0.05	4.23 ± 0.05
V	-2.80 ± 0.11	-0.07	3.66 ± 0.15
G	-2.06 ± 0.06	0.67	3.66 ± 0.09
G	-1.72 ± 0.12	0.98	3.62 ± 0.16
V	-1.87 ± 0.15	0.31	2.92 ± 0.20
L	-2.61 ± 0.08	0.12	3.66 ± 0.10
L	-2.88 ± 0.08	0.05	3.93 ± 0.11
L	-3.25 ± 0.12	0.05	4.43 ± 0.16
L	-3.73 ± 0.22	0.05	5.07 ± 0.30
L	-4.00 ± 0.07	0.05	5.44 ± 0.09
L	-3.86 ± 0.15	0.05	5.24 ± 0.20
L	-3.63 ± 0.26	0.05	4.93 ± 0.34
L	-3.12 ± 0.38	0.05	4.24 ± 0.51
G	-1.72 ± 0.36	0.60	3.10 ± 0.48
G	-1.02 ± 0.14	0.98	2.68 ± 0.19
L	-0.75 ± 0.26	0.43	1.54 ± 0.36
L	-0.85 ± 0.09	0.05	1.13 ± 0.14
L	-0.89 ± 0.12	0.05	1.19 ± 0.18
K	n.d.	0.55	n.d.
K	n.d.	0.88	n.d.
K	n.d.	0.88	n.d.

Table S11: Numerical values of k_{exp} and ΔG of pA.

k_{exp} is from exponential fit of means ± SE. For exponential fits see Figure S4.
ΔG is listed with the confidence interval, based on the respective k_{exp} SEMs.
n.d. = not determined, as data points were not sufficient.

	pA		
amide	**log k_{exp} [min^{-1}]**	**log k_{ch} [min^{-1}]**	**ΔG**
K	n.d.	0.92	n.d.
A	n.d.	0.96	n.d.
A	n.d.	0.84	n.d.
A	n.d.	0.84	n.d.
A	0.26 ± 0.09	0.84	0.59 ± 0.16
A	-0.17 ± 0.08	0.84	1.29 ± 0.13
A	-0.70 ± 0.05	0.84	2.05 ± 0.07
A	-1.22 ± 0.03	0.84	2.76 ± 0.04
A	-1.50 ± 0.08	0.84	3.13 ± 0.10
A	-1.86 ± 0.12	0.84	3.62 ± 0.16
A	-1.90 ± 0.17	0.84	3.67 ± 0.23
A	-2.01 ± 0.19	0.84	3.82 ± 0.25
A	-2.10 ± 0.05	0.84	3.94 ± 0.07
A	-2.13 ± 0.39	0.84	3.97 ± 0.52
A	-2.29 ± 0.29	0.84	4.20 ± 0.39
A	-2.25 ± 0.18	0.84	4.14 ± 0.24
A	-2.08 ± 0.08	0.84	3.91 ± 0.11
A	-2.01 ± 0.13	0.84	3.82 ± 0.17
A	-1.98 ± 0.20	0.84	3.77 ± 0.26
A	-1.82 ± 0.13	0.84	3.56 ± 0.18
A	-1.65 ± 0.11	0.84	3.33 ± 0.15
A	-1.40 ± 0.05	0.84	2.99 ± 0.07
A	-1.20 ± 0.07	0.84	2.73 ± 0.10
A	-0.75 ± 0.07	0.84	2.11 ± 0.10
A	-0.51 ± 0.12	0.84	1.78 ± 0.17
K	n.d.	0.76	n.d.
K	n.d.	0.88	n.d.
K	n.d.	0.88	n.d.

Table S12: Numerical values of k_{exp} and ΔG of pL-L15A9.

k_{exp} is from exponential fit of means ± SE. For exponential fits see Figure S4.
ΔG is listed with the confidence interval, based on the respective k_{exp} SEMs.
n.d. = not determined, as data points were not sufficient.

	pL-L15A9		
amide	**log k_{exp} [min^{-1}]**	**log k_{ch} [min^{-1}]**	**ΔG**
K	n.d.	0.88	n.d.
L	n.d.	0.34	n.d.
L	n.d.	0.02	n.d.
L	-0.55 ± 0.17	0.02	0.59 ± 0.29
L	-1.63 ± 0.06	0.02	2.19 ± 0.08
L	-2.47 ± 0.08	0.02	3.33 ± 0.11
L	-3.26 ± 0.07	0.02	4.39 ± 0.09
L	-3.88 ± 0.18	0.02	5.22 ± 0.24
L	-4.21 ± 0.14	0.02	5.67 ± 0.19
L	-4.46 ± 0.06	0.02	6.00 ± 0.08
L	-4.71 ± 0.10	0.02	6.33 ± 0.13
L	-4.49 ± 0.24	0.02	6.04 ± 0.32
L	-4.68 ± 0.19	0.02	6.30 ± 0.26
L	-4.59 ± 0.13	0.02	6.18 ± 0.17
L	-4.61 ± 0.09	0.02	6.21 ± 0.13
L	-4.35 ± 0.10	0.02	5.85 ± 0.14
A	n.d.	0.59	n.d.
A	n.d.	0.80	n.d.
A	n.d.	0.80	n.d.
A	n.d.	0.80	n.d.
A	-1.78 ± 0.13	0.80	3.46 ± 0.18
A	-1.71 ± 0.05	0.80	3.36 ± 0.07
A	-0.95 ± 0.17	0.80	2.33 ± 0.23
A	-0.73 ± 0.05	0.80	2.03 ± 0.07
A	-0.46 ± 0.07	0.80	1.65 ± 0.09
K	n.d.	0.76	n.d.
K	n.d.	0.88	n.d.
K	n.d.	0.88	n.d.

Table S13: Numerical values of k_{exp} and ΔG of pL-A15L9.

k_{exp} is from exponential fit of means ± SE. For exponential fits see Figure S4.
ΔG is listed with the confidence interval, based on the respective k_{exp} SEMs.
n.d. = not determined, as data point were not sufficient.

	pL-A15L9		
amide	**log k_{exp} [min^{-1}]**	**log k_{ch} [min^{-1}]**	**ΔG**
K	n.d.	0.92	n.d.
A	n.d.	0.96	n.d.
A	n.d.	0.84	n.d.
A	n.d.	0.84	n.d.
A	0.16 ± 0.08	0.84	0.77 ± 0.14
A	-0.26 ± 0.06	0.84	1.43 ± 0.08
A	-0.56 ± 0.11	0.84	1.85 ± 0.15
A	-1.18 ± 0.08	0.84	2.69 ± 0.11
A	-1.56 ± 0.07	0.84	3.22 ± 0.10
A	-1.79 ± 0.17	0.84	3.52 ± 0.23
A	-1.95 ± 0.13	0.84	3.74 ± 0.18
A	-2.11 ± 0.20	0.84	3.95 ± 0.27
A	-2.38 ± 0.15	0.84	4.31 ± 0.21
A	-2.00 ± 0.07	0.84	3.80 ± 0.09
A	-2.28 ± 0.17	0.84	4.18 ± 0.23
A	-2.46 ± 0.13	0.84	4.43 ± 0.17
L	n.d.	0.21	n.d.
L	-3.04 ± 0.12	0.05	4.14 ± 0.16
L	-3.42 ± 0.08	0.05	4.65 ± 0.11
L	-3.54 ± 0.27	0.05	4.81 ± 0.37
L	-3.68 ± 0.25	0.05	5.00 ± 0.33
L	-3.63 ± 0.26	0.05	4.93 ± 0.35
L	-3.09 ± 0.22	0.05	4.22 ± 0.29
L	-3.35 ± 0.33	0.05	4.56 ± 0.44
L	-2.80 ± 0.17	0.05	3.83 ± 0.22
K	n.d.	0.55	n.d.
K	n.d.	0.88	n.d.
K	n.d.	0.88	n.d.

8 List of Figures

9 List of Tables